Utilizing the Unique Properties of Seismic Diffractions

Dissertation

zur Erlangung des Doktorgrades
an der Fakultät für
Mathematik, Informatik und Naturwissenschaften

im Fachbereich Geowissenschaften
der Universität Hamburg

vorgelegt von

Alexander Bauer

Hamburg

2019

Tag der Disputation: 02.07.2019

Folgende Gutachter empfehlen die Annahme der Dissertation:

Prof. Dr. Dirk Gajewski
Dr. Benjamin Schwarz

A mi bella esposa, que amo con todo mi ser.

Abstract

Traditional seismic processing has often been steered toward the imaging of seismic reflections. However, in the recent years, the diffracted wavefield, often weak and therefore hidden behind high-amplitude reflections, has gained increasing importance. As diffractions are caused by structures smaller than the predominant seismic wavelength, they are often related to complex geological features such as faults, edges or pinch-outs. Still, diffractions are not only interesting from a structural viewpoint, but also due to their unique physical properties. Unlike a reflected wave, which honors Snell's law and is reflected under its incidence angle, a diffracted wave is scattered into all directions independent of its incidence angle. Therefore, in the context of seismic imaging, a diffracted wave connected to the same scattering object in the subsurface can be measured along large parts of the recording surface and thus contains a significant amount of information about the traversed structures. This work aims to utilize these unique physical properties of seismic diffractions for the enhancement of prestack data and for improved tomographic velocity model building for both multi-channel and single-channel data. The mentioned methods rely on the so-called wavefront attributes, which are a by-product of multi-parameter stacking schemes such as the zero-offset common-reflection-surface stack. In the diffraction case, these attributes describe the emergence angle and the curvature of the wavefront measured at the surface. They are encoded in the first and second derivatives of the traveltime moveout, which – in constrast to the reflection case – for diffractions can be measured in a zero-offset section. This property can be exploited for the imaging of diffractions in the whole prestack data cube by composing any set of finite-offset attributes out of two independent sets of zero-offset attributes originating from the same diffracting structure. Beyond imaging, zero-offset wavefront attributes are also the input for wavefront tomography, an efficient and stable method for the joint estimation of smooth velocity models and the localization of measurements in depth. In the past, wavefront tomography has been applied mainly to reflected measurements. I suggest, however, to utilize diffractions in the inversion process. While results for simple synthetic data show the potential of diffractions, an application to industrial field data suggests that a joint inversion of high-amplitude reflections and low-amplitude diffractions can help to increase the lateral resolution of the obtained velocity models. As a next step, in order to further exploit the properties of diffractions, I propose to enforce the focusing of back-propagated diffracted measurements with the same origin in depth. A requirement for this idea is the a priori identification of all measurements that belong to the same subsurface region. For this purpose, I introduce an event tagging algorithm, which automatically analyzes the local similarity of wavefront attributes and assigns a numerical tag to each diffraction found in the data. Finally, I introduce diffraction wavefront tomography, a modified implementation of the conventional inversion scheme, in which all diffractions with the same tag are forced to focus in depth. The modified algorithm reduces the dependency of wavefront tomography on second-order attributes and evolves into a zero-offset slope tomography, if they are not taken into account. Results for synthetic diffraction data with vertical and lateral heterogeneity suggest that the new approach, which is likewise applicable to passive seismic data, may offer increased stability in laterally heterogeneous settings.

Zusammenfassung

Traditionelle seismische Datenbearbeitung ist häufig auf die Abbildung seismischer Reflexionen ausgerichtet. In den letzten Jahren hat jedoch das diffraktierte Wellenfeld, welches oft schwach und daher von hochamplitudigen Reflexionen überlagert ist, eine erhöhte Aufmerksamkeit erlangt. Da Diffraktionen von Strukturen kleiner als die vorherrschende seismische Wellenlänge verursacht werden, stehen sie oft in Zusammenhang mit komplexen geologischen Strukturen wie Verwerfungen, Kanten oder stratigraphischen Fallen. Diffraktionen sind jedoch nicht nur aus einem strukturellen Blickwinkel interessant, sondern auch aufgrund ihrer einzigartigen physikalischen Eigenschaften. Im Gegensatz zu einer reflektierten Welle, die dem Snelliusschen Brechnungsgesetz unterliegt und unter ihrem Einfallswinkel reflektiert wird, wird eine diffraktierte Welle unabhängig von ihrem Einfallswinkel in alle Richtungen gestreut. Im Kontext seismischer Abbildungsverfahren kann daher eine diffraktierte Welle, die zu demselben Untergrundobjekt gehört, entlang eines Großteils des Messbereichs an der Oberfläche registriert werden und enthält zudem sehr viele Informationen über die durchquerten Strukturen. Das Ziel dieser Arbeit ist es, diese einzigartigen physikalischen Eigenschaften seismischer Diffraktionen für die Charakterisierung ungestapelter Daten und für eine verbesserte tomographische Geschwindigkeitsmodellbestimmung sowohl für Mehrkanal- als auch für Einkanaldaten auszunutzen. Die erwähnten Methoden basieren auf sogenannten Wellenfrontattributen, die ein Nebenprodukt von Multiparameter-Stapelmethoden wie dem Zero-Offset-Common-Reflection-Surface-Stack sind. Im Fall einer Diffraktion beschreiben diese Attribute den Auftauchwinkel und den Radius der an der Oberfläche gemessenen Wellenfront. Sie können aus den ersten und zweiten Ableitungen des seismischen Moveouts extrahiert werden, welcher für Diffraktionen – im Gegensatz zu Reflexionen – in der Zero-Offset-Sektion gemessen werden kann. Diese Eigenschaft kann für die Abbildung von Diffraktionen in den gesamten ungestapelten Daten ausgenutzt werden, indem jeder Finite-Offset-Attributsatz aus einem Paar von Zero-Offset-Attributsätzen kombiniert wird, die von derselben diffraktierenden Untergrundstruktur stammen. Des Weiteren sind Zero-Offset-Wellenfrontattribute die Basis für Wellenfront-Tomographie, eine effiziente und stabile Methode für die Bestimmung glatter Geschwindigkeitsmodelle und die gleichzeitige Lokalisierung der Messungen im Untergrund. In der Vergangenheit wurde Wellenfront-Tomographie hautpsächlich auf Reflexionsmessungen angewandt. Ich schlage hingegen vor, auch Diffraktionen für die Inversion zu nutzen. Während Ergebnisse für simple, synthetische Diffraktionsdaten das Potenzial von Diffraktionen zeigen, suggeriert eine Anwendung auf industrielle Felddaten, dass eine gleichzeitige Inversion von hochamplitudigen Reflexionen und niedrigamplitudigen Diffraktionen dazu beitragen kann, die laterale Auflösung der resultierenden Geschwindigkeitsmodelle zu erhöhen. Um die Eigenschaften von Diffraktionen weiter auszunutzen, besteht der nächste Schritt darin, die Fokussierung zurückpropagierter Diffraktionsmessungen mit demselben Ursprung im Untergrund zu erzwingen. Eine Voraussetzung für diese Idee ist die vorhergehende Identifizierung aller Messungen, die zu derselben Untergrundregion gehören. Zu diesem Zweck führe ich einen Event-Tagging-Algorithmus ein, der automatisch die lokale Ähnlichkeit der Wellenfrontattribute analysiert und jeder Diffraktion in den Daten einen numerischen Tag zuordnet.

Schließlich führe ich Diffraktions-Wellenfront-Tomographie ein, eine modifizierte Implementation des konventionellen Inversionsschemas, in welchem die Fokussierung aller Diffraktionen mit demselben Tag in der Tiefe erzwungen wird. Der modifizierte Algorithmus reduziert die Abhängigkeit der Wellenfront-Tomographie von Attributen zweiter Ordnung und wird zu einer Zero-Offset-Slope-Tomographie, wenn diese nicht berücksichtigt werden. Ergebnisse für synthetische Diffraktionsdaten mit sowohl vertikaler als auch lateraler Heterogenität suggerieren, dass der neue Ansatz, welcher gleichermaßen auf passiv-seismische Daten anwendbar ist, in Fällen mit lateraler Heterogenität die Stabilität erhöhen kann.

Contents

List of Figures

1 Introduction

The acquisition and processing of active seismic data looks back on an extensive history (e.g. Claerbout, 1985). Driven by both academic institutions and the hydrocarbon industry, impressive developments have been achieved within the last decades. While traditional seismic processing has often been steered towards the imaging of high-amplitude reflections, seismic diffractions, which often have weak amplitudes, have been neglected or even treated as noise. In the recent years, however, diffractions have gained importance, mainly because they are caused by small-scale objects and thus related to geologically complex structures, such as faults, edges or pinch-outs (e.g. Krey, 1952; Khaidukov et al., 2004). In contrast to existing applications, which have used diffractions mainly for high-resolution imaging (e.g. Landa and Keydar, 1998; Kozlov et al., 2004; Moser and Howard, 2008; Foss et al., 2018), I propose to use them for velocity model building. While the mentioned publications treat seismic diffractions from a structural viewpoint, this work aims to treat them from a wavefront perspective, thus utilizing their unique physical properties.

In the context of geometrical optics, a field widely used for the description of wave propagation phenomena, diffractions are considered as effects that cannot be described by the ordinary theory, such as energy entering shadow zones and scattering at corners or edges (Keller, 1962). I aim to illustrate an essential property of diffractions – namely illumination – by means of Figure 1.1. This photo, taken by myself with a telephoto lens, shows a christmas ball hanging from a tree in

Figure 1.1: *A christmas ball hanging from a tree in Lüneburg, Germany (photo taken and edited by me).*

the city of Lüneburg, Germany. On the surface of this christmas ball, the viewer can recognize a large part of the surroundings: numerous houses, the street, the sky and my wife and myself. All this information is concentrated in a small-scale object. This illustrates the illumation potential

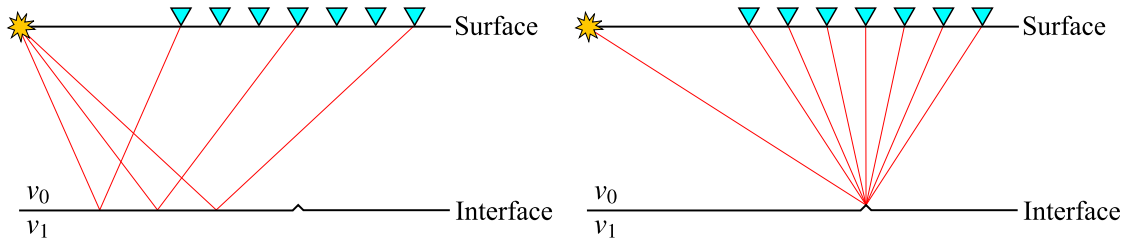

(a) Reflection case (b) Diffraction case

FIGURE 1.2: *Illustration of the seismic experiment. An abrupt velocity change from v_0 to v_1 with an extension considerably smaller than the seismic wavelength acts as a reflecting interface in the subsurface. In the reflection case (a), waves emitted by the source (star) and reflected at the interface are measured at the receivers (triangles). The ray paths (red) honor Snell's law. Therefore, in order to image the reflector from different directions, sufficiently large source-receiver offsets are required. In the diffraction case (b), a small-scale subsurface structure scatters an incoming wave into all directions, that is, the ray paths (red) do not honor Snell's law. As a result, the response can be measured at all receivers.*

of a seismic diffraction, because a seismic wave, which strikes a subsurface structure smaller than its predominant wavelength, is scattered into all directions. This back-scattered wave – just like the christmas ball – contains a lot of information about the subsurface and it can be measured at large parts of the recording surface. This information merely includes propagation effects, but no directionality or the geometrical shape of the scattering object, which allows an analogous description of passive seismic signals. In constrast, a reflecting subsurface structure has an extension significantly larger than the seismic wavelength except for one spatial direction. Therefore, a reflected wave has a specific directionality and, consequently, can be measured only at a distinct region of the recording surface. In the context of Figure 1.1 this would mean a reflecting disk instead of a sphere, which would not be able to image the complete surroundings, but only a small part depending on the viewing angle. Considering that this combination of superior illumination and lateral resolution renders the diffracted wavefield valuable, the aim of this work is to utilize these unique physical properties of diffractions, that is, non-Snell scattering at point-like structures or edges, for seismic imaging and subsurface velocity model building.

In order to back the preceding conceptual introduction in the context of applied seismics, Figure 1.2 illustrates the seismic experiment. When a wave emitted from a source (star) is reflected at an interface (Figure 1.2a), its ray paths honor Snell's law and hence, sufficiently large source-receiver offsets are required during the acquisition in order to image a specific region on the reflector from different directions. In the diffraction case (Figure 1.2b), however, a small-scale subsurface structure scatters an incoming wave into all directions and Snell's law does not hold. As a result, the wavefront diffracted at the same subsurface object can be measured at all receivers (triangles). I argue that this superior subsurface illumination of diffractions compared to reflected waves can be exploited for an improved description of the subsurface particularly in terms of lateral resolution.

A prerequisite for all applications presented in this work are the so-called wavefront attributes, which can be extracted from the traveltime moveout of seismic waves. Initially, wavefront attributes (Hubral, 1983) were a by-product of multi-parameter stacking schemes such as the common-reflection-surface (CRS) stack (Jäger et al., 2001) or the multifocusing stack (Gelchinsky

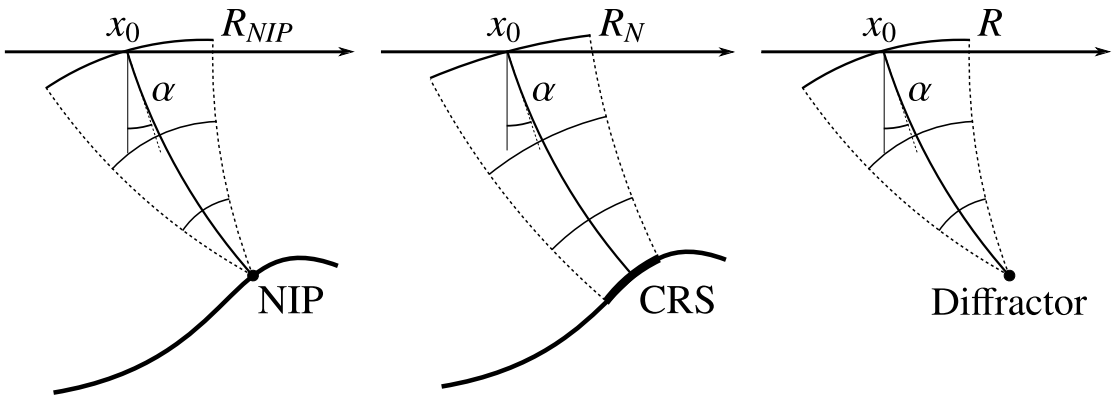

(a) Reflection case: NIP wave (b) Reflection case: normal wave (c) Diffraction case

FIGURE 1.3: *The 2D wavefront attributes α, R_{NIP} and R_N. In the general reflection case, the NIP wave (left) is excited by a point source placed on the reflector's point of normal incidence (NIP) and the normal wave (middle) is excited by an exploding reflector segment (CRS) around the NIP. In the case of a diffraction (right), the exploding reflector segment shrinks to a point that is the actual diffractor acting as a secondary source. Consequently, R_{NIP} and R_N coincide and the NIP wave is no longer fictitious, but it describes the actual diffracted wavefront.*

et al., 1999). These stacking schemes were introduced as an extension of the classical common-midpoint (CMP) stack (Mayne, 1962) by stacking not only in offset direction, but also in midpoint direction. This resulted in a moveout description that depends on three parameters instead of one. These three parameters – encoded in the first and second derivatives of the moveout – are related to the physical properties of the wavefront measured at the recording surface (Hubral, 1983). As illustrated in Figure 1.3, they consist of one emergence angle and the curvatures of two conceptual wavefronts, the normal-incidence-point (NIP) wave and the normal wave. While the NIP wave (Figure 1.3a) is thought to be excited by a point source placed on the reflector's point of normal incidence, the normal wave (Figure 1.3b) is thought to be excited by an exploding reflector segment around the NIP. Hence, in the case of a reflection, the radius of the NIP wave is related to the depth of the reflector and the radius of the normal wave is related to its curvature. In the case of a diffraction, however, these two waves coincide and the remaining wave is no longer hypothetical, but it describes the actual wavefront of the diffraction (Figure 1.3c), thus reducing the number of parameters to two. Figure 1.4 exemplarily shows the results of the application of the zero-offset CRS stack to a simple dataset containing one diffraction. While the zero-offset stack (Figure 1.4a), which has an enhanced signal-to-noise ratio compared to the more noisy raw data due to the stacking of the measurements along the moveout surface, is a first interpretable image of the subsurface, the coherence section (Figure 1.4b), which shows the semblance coefficients (Neidell and Taner, 1971) of all time samples, indicates, where in the data coherent energy was found by the optimization algorithm. In both sections, the diffraction is clearly distinguishable from the surrounding noise. A by-product of the CRS stack are the wavefront attributes: the emergence angle α (Figure 1.4c), encoded in the first derivative of the traveltime moveout Δt, and the radius of the NIP wave R_{NIP} (Figure 1.4d), encoded in the second derivative of Δt. The second wavefront radius R_N is not shown here, because it coincides with R_{NIP} in the diffraction case. While the plots reveal the smooth behavior of the wavefront

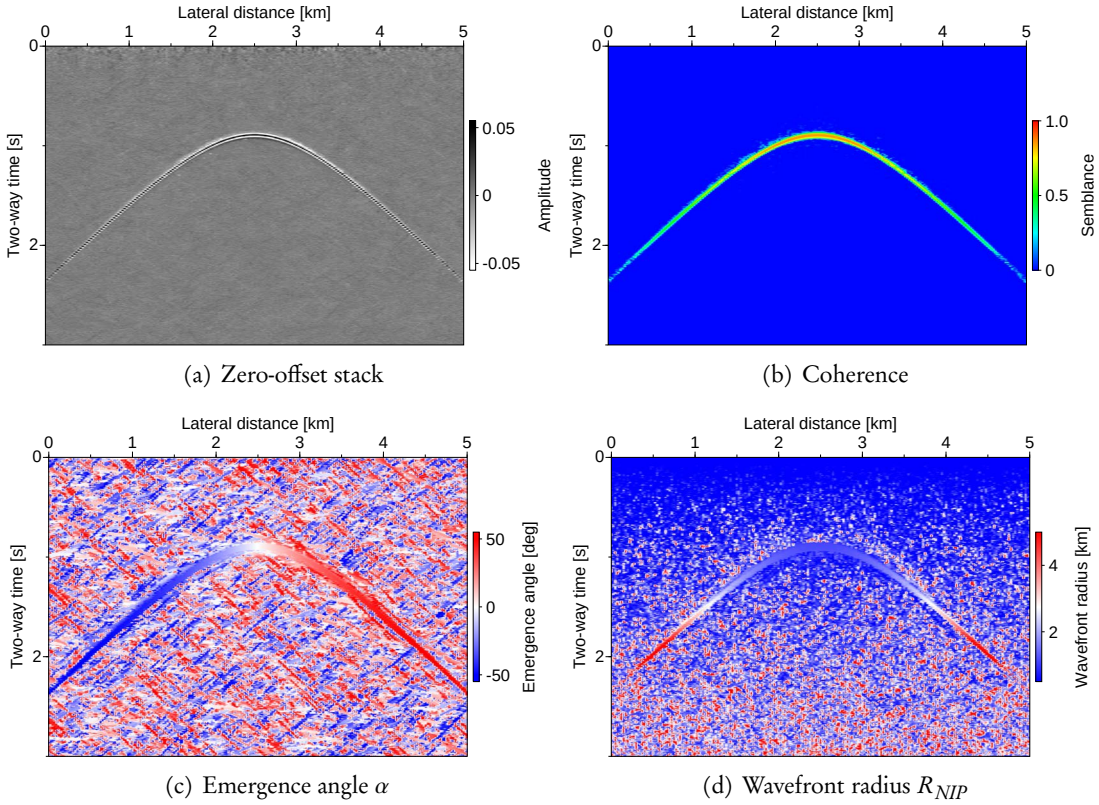

(a) Zero-offset stack (b) Coherence

(c) Emergence angle α (d) Wavefront radius R_{NIP}

Figure 1.4: *Results of the common-reflection-surface (CRS) stack for data with one diffraction. Panel (a) is the zero-offset stack, (b) is the coherence section, (c) is the emergence angle α and (d) is the radius of the NIP wave R_{NIP}.*

attributes – in particular the emergence angle – along the diffraction, the surrounding parts of the attribute sections can be ignored, because the semblance coefficients are very close to zero in the corresponding regions.

Generally, the common-reflection surface can be approximated by parabolic (Schleicher et al., 1993), hyperbolic (Jäger et al., 2001) or non-hyperbolic (Gelchinsky et al., 1999; Schwarz et al., 2014a; Fomel and Kazinnik, 2013) moveout descriptions, which generally can be divided into two categories depending on their derivation (Schwarz and Gajewski, 2017b). However, recent studies have shown that differences between the different moveout approximations vanish in complex settings (Walda et al., 2017). For the characterization and imaging of measurements in the prestack domain, more complex finite-offset formulations with a larger number of parameters exist (Zhang et al., 2001). However, the estimation of wavefront attributes with these operators for an entire prestack data cube is a very expensive process. Aiming for a cost-efficient alternative, Baykulov and Gajewski (2009) have proposed a method that uses zero-offset wavefront attributes for the interpolation and regularization of prestack data. Alternatively, finite-offset wavefront attributes can be extrapolated from zero-offset (Schwarz et al., 2015). Chapter 2 of this thesis introduces a method for the determination of exact finite-offset wavefront attributes for diffractions (Bauer et al., 2016a), which utilizes the previously introduced unique physical properties of diffractions – namely the fact that Snell's law does not hold for diffractions and therefore, their

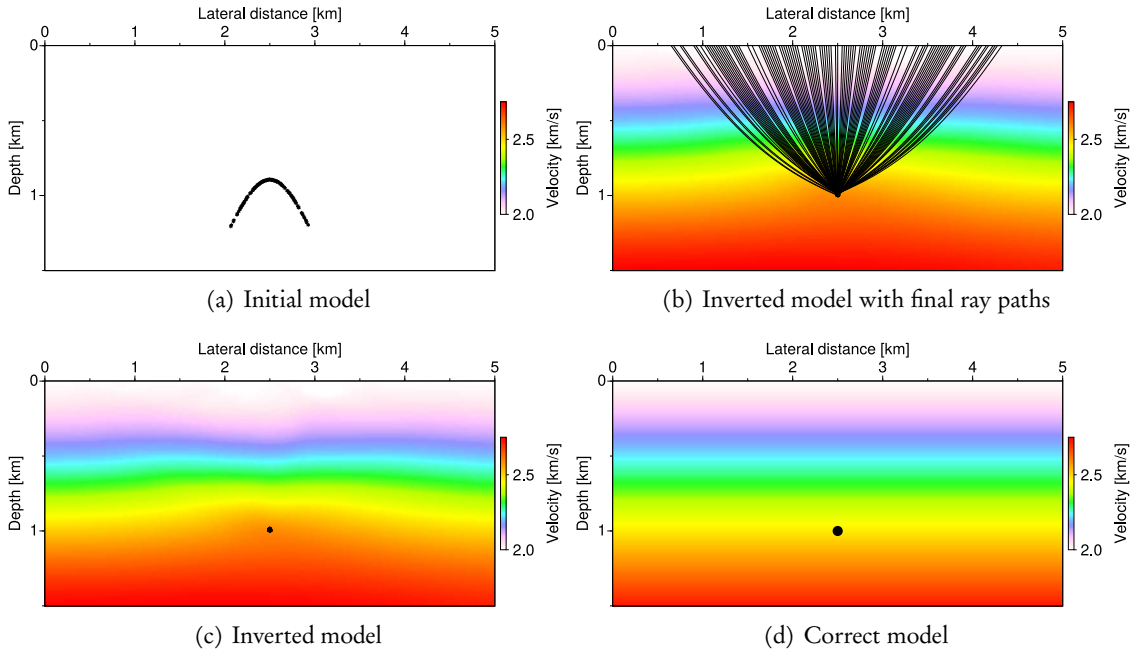

(a) Initial model

(b) Inverted model with final ray paths

(c) Inverted model

(d) Correct model

FIGURE 1.5: *Inversion results for data with one diffraction. Panel (a) is the constant initial model with the back-propagated data points (black asterisks), (b) is the inverted velocity model with the final ray paths, (c) is the inverted model with the back-propagated data points and (d) is the correct velocity model with the true diffractor position.*

up- and downgoing ray paths are decoupled.

While the initial purpose of multi-parameter stacking was the reduction of noise in seismic data (e.g. Eisenberg-Klein et al., 2008), the parametrization of the moveout surface in terms of physically meaningful wavefront attributes has paved the way for numerous subsequent processing steps. In the context of noise reduction and data regularization and enhancement in the prestack domain, impressive results have been presented (Baykulov and Gajewski, 2009; Baykulov et al., 2011). While Mann (2002) used wavefront attributes for the estimation of time migration velocities, Dell and Gajewski (2011) presented an attribute-based approach for diffraction separation. Recently, Schwarz (2019) proposed a method for accessing the diffracted wavefield by modeling and adaptive subtraction of high-amplitude reflections.

While stacking and time migration yield a first image of the subsurface in the time domain, the final goal of seismic processing is to obtain a depth image of the subsurface. In order to be able to convert the time axis to a depth axis, a wave velocity model of the subsurface is required. For the estimation of velocity models, often referred to as *seismic inversion* (Tarantola, 1984), numerous techniques exist that range from ray-based tomographic methods, which try to invert for traveltime-related attributes (e.g. Tromp et al., 2005), to full-waveform inversion (FWI) that tries to invert for the measured waveforms (e.g. Virieux and Operto, 2009). In this work, I use wavefront tomography, an inversion algorithm introduced by Duveneck (2004b), which utilizes zero-offset wavefront attributes for depth velocity model building. Following up on the previous schematic illustration, Figure 1.5 shows the results of an application of wavefront tomography to the previously introduced data set containing merely one single diffraction (compare Figure 1.4).

Starting from a constant initial model (Figure 1.5a), in which the back-projected data points (black asterisks) – that can be picked in an automatic fashion based on the semblance coefficient (Figure 1.4b) – still form a hyperbola due to the wrong velocities, the result of the inversion (Figure 1.5c) shows that the localizations of all data points – although treated independently during the inversion – focus in one distinct subsurface location and that the correct velocity model (Figure 1.5d) could be recovered. The final ray paths (Figure 1.5b) reveal, which parts of the velocity model are backed by the data and thus illustrate the illumination potential of diffractions.

Past applications of wavefront tomography were mainly based on high-amplitude reflections (Meier, 2007; Dümmong et al., 2008) and suggested that prestack slope tomography (Billette and Lambaré, 1998), which is based on finite-offset slopes, is able to provide better-resolved velocity models. However, in the paper presented in Chapter 3 of this thesis (Bauer et al., 2017b), we propose a joint inversion utilizing both high-amplitude reflections and low-amplitude diffractions in order to increase the lateral resolution of the obtained velocity models and thereby close the gap between prestack slope tomography and poststack wavefront tomography. Thus, we render possible better-resolved inversions in the more stable poststack domain, which is often the only option in academic environments. In addition, Schwarz et al. (2016b) have shown that wavefront tomography is likewise applicable to passive seismic data, where it can provide joint source localization and velocity model building (Diekmann et al., 2019a).

In spite of the promising results, the full potential of diffractions – namely their focusing nature (compare Figure 1.5) – had not yet been exploited. For that purpose, however, all measurements in the zero-offset section that belong to the same diffraction – and thus to the same subsurface region – have to be identified and assigned with a so-called event tag. In Chapter 4 of this thesis, I present a paper (Bauer et al., 2019c), in which we introduce an event-tagging algorithm, which utilizes the local similarity of wavefront attributes for the unsupervised identification and tagging of diffractions in the zero-offset domain.

The availability of event tags paves the way for a diffraction wavefront tomography, in which all data points belonging to the same diffraction are forced to focus in depth. In Chapter 5 of this thesis, I present first promising results of this modified implementation of wavefront tomography with enforced diffraction focusing (Bauer et al., 2019a). The modified implementation reduces the dependency of wavefront tomography on second-order wavefront attributes and thus helps to increase the stability of the inversion in complex settings with lateral heterogeneity. Further, it is applicable to zero-offset, passive-seismic and even to earthquake data (Diekmann et al., 2019a), where the determination of second-order attributes is often challenging.

1.1 Structure of the thesis

Following the introduction given in this chapter, Chapter 2 contains the paper *Enhancement of prestack diffraction data and attributes using a traveltime decomposition approach*, which was published in 2016 in the journal *Studia Geophysica et Geodaetica* (Bauer et al., 2016a). This work introduces a method for diffraction enhancement in prestack data, which utilizes the fact that Snell's law does not hold for diffracted waves and, consequently, up- and downgoing diffraction raypaths are decoupled.

Chapter 3 consists of the paper *Utilizing diffractions in wavefront tomography* that was published in 2017 in *Geophysics* (Bauer et al., 2017b). In this work, diffractions are used for velocity model building with wavefront tomography. While results for simple synthetic diffraction data

illustrate the potential, results for industrial multi-channel field data suggest that diffractions can help to increase the lateral resolution of tomographic velocity models and improve depth-migrated images.

In Chapter 4, the paper *Unsupervised event identification and tagging for diffraction focusing*, which was recently published in *Geophysical Journal International* (Bauer et al., 2019c), is presented. This work proposes a scheme for the identification and tagging of diffractions in zero-offset data, which is based on the local similarity of zero-offset wavefront attributes.

While these event tags may significantly improve the performance of the diffraction decomposition, most importantly they are a prerequisite for the development of a *Diffraction wavefront tomography*, which is presented in Chapter 5 by means of a manuscript that will be submitted to a scientific journal in the near future, but has already been accepted for conferences (Bauer et al., 2019b,a). It presents a modified implementation of wavefront tomography, in which diffractions are forced to focus in depth. This new approach allows the application of wavefront tomography to zero-offset and passive seismic data and may increase its stability in settings with strong lateral heterogeneity.

Finally, in Chapter 6 I summarize this work and draw overall conclusions, before giving an outlook to possible future work in Chapter 7.

1.2 Contributions of co-authors

Chapters 2–4 of this work are papers published in scientific journals and Chapter 5 is based on a manuscript that will be published in the near future. In the following, I shortly state the contributions of the co-authors of each paper and my contributions to the two publications I co-authored (Schwarz et al., 2016b; Diekmann et al., 2019a) that are not included in this thesis.

The original idea for the diffraction decomposition introduced in Bauer et al. (2016a) stems from Benjamin Schwarz. Further, Benjamin Schwarz was the supervisor of my master's thesis and Dirk Gajewski is the supervisor of both my master's thesis and my PhD work. Both also contributed via continuous discussion.

Simultaneously to this paper, Benjamin Schwarz published his work on passive seismic source localization and velocity model building (Schwarz et al., 2016b), to which I contributed as a co-author by providing the velocity model and my experience in the application of wavefront tomography.

The majority of the results presented in Bauer et al. (2017b) were produced by myself. Benjamin Schwarz contributed to this publication by the continuous discussion of ideas and results and assisted in writing parts of the manuscript. My supervisor Dirk Gajewski contributed via continuous discussion of the publication strategy. Although not listed as a co-author, I would like to explicitly acknowledge the work of Ekkehart Teßmer, who produced the RTM results presented in this work.

While the original idea and the implementation of the event tagging algorithm presented in Bauer et al. (2019c) are my own work, the implementation of the event tagging algorithm in 3D was carried out by Tobias Werner, whose master's thesis I supervised. Again, Benjamin Schwarz contributed by continuously discussing ideas and results. Further, I included his implementation for the calculation of apex coordinates into my code. My supervisor Dirk Gajewski contributed by discussing both content and the publication strategy.

Recently, Diekmann et al. (2019a) submitted a paper on simultaneous localization and velocity

model building for passive seismic data with wavefront tomography, to which I contributed as a co-author with my experience in the application of wavefront tomography and by providing data in the course of the work.

The work presented in Chapter 5 ties my three first-author publications together and concludes the initial idea of my PhD work of developing a zero-offset slope tomography for diffractions. While this vision was an idea of Benjamin Schwarz and myself, I elaborated the detailed concept and implemented the method. Leon Diekmann contributed to this work by providing the laterally heterogeneous velocity model and his code for the modeling of synthetic data.

2 Enhancement of prestack diffraction data and attributes using a traveltime decomposition approach

Abstract

Diffractions not only carry important information about small-scale subsurface structures, they also possess unique properties, which make them a powerful tool for seismic processing and imaging. Since a point diffractor scatters an incoming wave into all directions, a diffraction event implies better illumination than a reflection, because the rays travel through larger parts of the subsurface. Furthermore, unlike the reflection case, in which the emergence location of the reflected wave depends on the source position, in the case of non-Snell scattering, up-going and down-going raypaths are decoupled. Based on this decoupling, we introduce a diffraction traveltime decomposition principle, which establishes a direct connection between zero-offset and finite-offset diffraction wavefield attributes. By making use of this approach, we are able to enhance diffractions and obtain high-quality diffraction wavefield attributes at arbitrary offsets in the prestack domain solely based on zero-offset processing without any further optimization of attributes. We show the accuracy of the method by fitting diffraction traveltimes and on simple waveform data. Application to complex synthetic data shows the ability of the proposed approach to enhance diffractions and provide high-quality wavefield attributes even in sparsely illuminated regions such as subsalt areas. The promising results reveal a high potential for improved prestack data enhancement and further applications such as efficient diffraction-based finite-offset tomography.

2.1 Introduction

Conventional seismic processing techniques are designed to image and enhance reflection events. However, reflected waves are not suitable for high-resolution structural imaging of features below the Rayleigh limit of half a seismic wavelength (e.g. Dell and Gajewski, 2011). Information about these small-scale structures such as edges, faults, pinch-outs and small-size scattering objects is encoded in the diffraction response of the subsurface (Khaidukov et al., 2004; Fomel et al., 2007). Therefore, the imaging of diffracted waves is a crucial challenge in seismic processing. Recently, different workflows with the goal to separate diffractions from reflections and to enhance diffractions in the post-stack domain have been presented (Fomel et al., 2007; Berkovitch et al., 2009; Dell and Gajewski, 2011). However, an important goal of diffraction imaging is the separation of diffractions and their enhancement in the full prestack data volume, which requires finite-offset (FO) processing. Finite-offset processing may provide improved resolution, especially in sparsely illuminated regions such as subsalt areas (Spinner et al., 2012), but due to the larger number

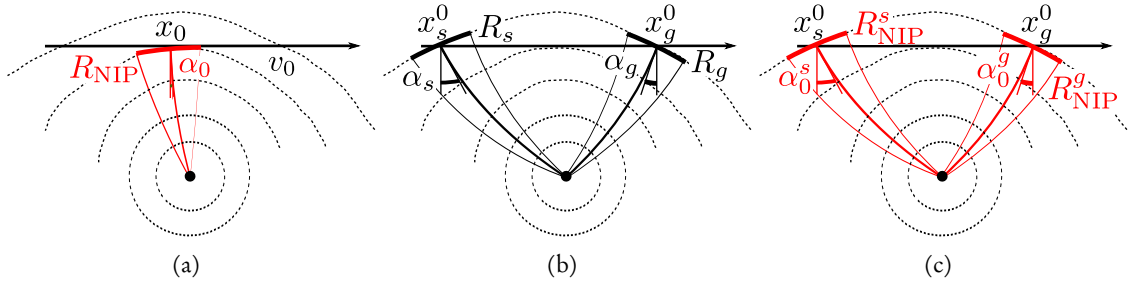

FIGURE 2.1: *In the diffraction case, the zero-offset NIP wave (a) approximates the actual physical wavefront. In the finite-offset setting (b), the common-shot (CS) and common-receiver (CR) experiments may be resembled by two independent zero-offset NIP-wave experiments (c) at source x_s^0 and receiver x_g^0.*

of parameters, the problem is of higher dimensionality, which makes processing less stable and computationally more expensive than in the zero-offset (ZO) setting.

In order to combine the stability of the zero-offset common-reflection-surface (CRS) stack (Jäger et al., 2001) with the improved illumination of finite-offset processing, we introduce a straightforward decomposition principle for diffractions. Based on the redundancy of zero-offset and finite-offset information for diffractions, this new approach allows the direct prediction of finite-offset diffraction attributes from zero-offset CRS processing results (Schwarz et al., 2014a; Bauer, 2014). In this fashion, the full prestack data volume is accurately characterized without carrying out computationally expensive generic finite-offset CRS processing (Zhang et al., 2001) or partial CRS stacking (Baykulov and Gajewski, 2009), where finite-offset traveltimes are extrapolated from zero-offset results.

2.2 THEORY

The common-reflection-surface (CRS) stack is a multi-parameter stacking technique, in which stacking is not only carried out along a traveltime moveout curve in offset direction, but along a traveltime moveout surface in both offset and midpoint direction (Jäger et al., 2001). CRS processing is purely data-driven and provides stacked sections with increased signal-to-noise ratio compared to the classical common-midpoint (CMP) stack, particularly in areas with complex geology and sparse illumination.

The CRS stack has been formulated for a central zero-offset (ZO) ray (Jäger et al., 2001) and for an arbitrary finite-offset (FO) central ray (Zhang et al., 2001). While the widely used zero-offset CRS stack is fast, stable and reasonably accurate for moderate lateral heterogeneity, finite-offset CRS shows its strengths in complex geological settings, where it provides improved resolution and illumination at the cost of being computationally more expensive and less stable (see, e.g., Spinner et al., 2012).

2.2.1 ZERO-OFFSET COMMON-REFLECTION SURFACE

In the reflection case, the 2D zero-offset CRS traveltime moveout depends on three parameters, the kinematic wavefield attributes α_0, R_{NIP} and R_N (Hubral, 1983). The latter ones, R_{NIP} and R_N, are the radii of two fictitious wavefronts, the NIP wavefront and the normal wavefront. While the

NIP wave stems from a fictitious point source placed on the reflector's point of normal incidence (NIP, see Figure 2.1a), the normal wave is emitted by a fictitious exploding reflector segment around the NIP. The angle α_0 describes the direction, from which the two fictitious waves emerge at the central midpoint of the aperture. For the computation of the traveltime moveout along the CRS, different formulations exist. In this work, the hyperbolic and the parabolic traveltime descriptions are used. The hyperbolic CRS traveltime (Jäger et al., 2001) reads

$$t_{ZO}^2(\Delta x_m, h) = \left(t_0^{ZO} + \frac{2\sin\alpha_0}{v_0}\Delta x_m\right)^2 + \frac{2t_0\cos^2\alpha_0}{v_0}\left(\frac{\Delta x_m^2}{R_N} + \frac{h^2}{R_{NIP}}\right), \tag{2.1}$$

where $\Delta x_m = x_m - x_0$ is the displacement from the central midpoint x_0, h denotes the half-offset and v_0 the constant near-surface velocity. The parabolic CRS traveltime (Müller, 1999) is given by

$$t_{ZO}(\Delta x_m, h) = t_0^{ZO} + \frac{2\sin\alpha_0}{v_0}\Delta x_m + \frac{\cos^2\alpha_0}{v_0 R_{NIP}}h^2 + \frac{\cos^2\alpha_0}{v_0 R_N}\Delta x_m^2 . \tag{2.2}$$

In the special case of a diffraction, this traveltime moveout only depends on two parameters, because the NIP wave and the normal wave coincide,

$$t_{ZO}(\Delta x_m, h) = t_0^{ZO} + \frac{2\sin\alpha_0}{v_0}\Delta x_m + \frac{\cos^2\alpha_0}{v_0 R_{NIP}}\left(\Delta x_m^2 + h^2\right) . \tag{2.3}$$

As illustrated in Figure 2.1a, the NIP wave approximates the actual physical wavefront of a diffraction in the zero-offset section ($h = 0$),

$$t_{ZO}(\Delta x_m) = t_0^{ZO} + \frac{2\sin\alpha_0}{v_0}\Delta x_m + \frac{\cos^2\alpha_0}{v_0 R_{NIP}}\Delta x_m^2 . \tag{2.4}$$

Based on the zero-offset CRS stack, Baykulov and Gajewski (2009) recently introduced the so-called partial CRS stack. In this method, finite-offset traces are simulated by application of zero-offset operators for local finite-offset stacks, which corresponds to the extrapolation of traveltimes from zero-offset. Figure 2.2a shows an example of a partial CRS stacking surface. The expansion point of the zero-offset operator is marked in red. Due to the smaller number of parameters this method is computationally more efficient than the generic finite-offset stack and in cases of moderate complexity and for small partial stacking apertures zero-offset operators perform reasonably well. However, the zero-offset approximation loses accuracy with increasing offsets and complexity. Finite-offset operators are more appropriate for local refinement at far offsets (see also Bauer, 2014; Schwarz et al., 2014a).

2.2.2 Finite-offset common-reflection surface

The finite-offset CRS stack (Zhang et al., 2001) is a generalization of the zero-offset CRS stack to arbitrary source and receiver combinations, which allows the simulation of the full prestack data volume. Due to the higher dimensionality of the problem, the finite-offset CRS stack cannot be parametrized by only three parameters. Instead, because of the asymmetry of up- and downgoing raypaths, the finite-offset CRS parameters describe the attributes of the respective two-way wavefronts and a coupling coefficient. The five-parameter hyperbolic finite-offset CRS traveltime

in source ($x_s = x_m - h$) and receiver ($x_g = x_m + h$) coordinates (Bergler et al., 2002) is given by

$$\begin{aligned} t_{FO}^2(\Delta x_s, \Delta x_g) = &\left(t_0^{FO} + \frac{\sin\alpha_s}{v_s}\Delta x_s + \frac{\sin\alpha_g}{v_g}\Delta x_g \right)^2 \\ &+ 2t_0^{FO}\left(\frac{1}{2}B^{-1}A\Delta x_s^2 + \frac{1}{2}DB^{-1}\Delta x_g^2 + B^{-1}\Delta x_s\Delta x_g \right) , \end{aligned} \tag{2.5}$$

where Δx_s and Δx_g denote the displacements from the central source and receiver pair (x_s^0, x_g^0). Further, the angles of emergence at source and receiver are denoted by α_s and α_g[1] and accordingly, v_s and v_g are the near surface velocities at x_s^0 and x_g^0. The quantities A, B and D are the scalar elements of the surface-to-surface ray propagator matrix introduced by Bortfeld (1989). Zhang et al. (2001) describe these quantities in terms of the two emergence angles and three wavefront curvatures, which correspond to fictitious two-way waves observed in the common-shot (CS) and common-midpoint (CMP) configurations.

As it follows from a direct expansion of the traveltime, the parabolic finite-offset CRS traveltime formulation is physically more intuitive than its hyperbolic counterpart. Following Zhang et al. (2001), it reads

$$\begin{aligned} t_{FO}(\Delta x_s, \Delta x_g) = t_0^{FO} &+ \frac{\sin\alpha_s}{v_s}\Delta x_s + \frac{1}{2}\frac{\cos^2\alpha_s}{v_s R_s}\Delta x_s^2 \\ &+ \frac{\sin\alpha_g}{v_g}\Delta x_g + \frac{1}{2}\frac{\cos^2\alpha_g}{v_g R_g}\Delta x_g^2 \\ &+ B^{-1}\Delta x_s\Delta x_g , \end{aligned} \tag{2.6}$$

The coefficients of this second-order expression contain the emergence angles α_s, α_g and the radii of curvature R_s, R_g of the wavefronts measured in the common-shot (CS) and common-receiver (CR) configurations, respectively. For reflections, the coefficient B^{-1} couples the moveouts in the CS and CR gathers. In the diffraction case, the coupling between the two-way wavefronts vanishes and they reduce to one-way waves (see Figure 2.1b). Hence, B^{-1} becomes zero, which decouples the moveouts in the CS and CR configurations. Accordingly, the parabolic finite-offset response for diffractions reduces to

$$\begin{aligned} t_{FO}(\Delta x_s, \Delta x_g) = t_0^{FO} &+ \frac{\sin\alpha_s}{v_s}\Delta x_s + \frac{1}{2}\frac{\cos^2\alpha_s}{v_s R_s}\Delta x_s^2 \\ &+ \frac{\sin\alpha_g}{v_g}\Delta x_g + \frac{1}{2}\frac{\cos^2\alpha_g}{v_g R_g}\Delta x_g^2 . \end{aligned} \tag{2.7}$$

2.2.3 Diffraction traveltime decomposition

Due to the decoupling of diffraction raypaths, zero-offset and finite-offset information is redundant for diffractions (Schwarz et al., 2014a; Bauer et al., 2015b): the CS and CR responses in a finite-offset measurement (see Figure 2.1b) are technically identical to two independent zero-offset

[1] Please note that we use a different sign convention for the emergence angles at source and receiver, which results in an alteration in signs compared to the original formula by Zhang et al. (2001)

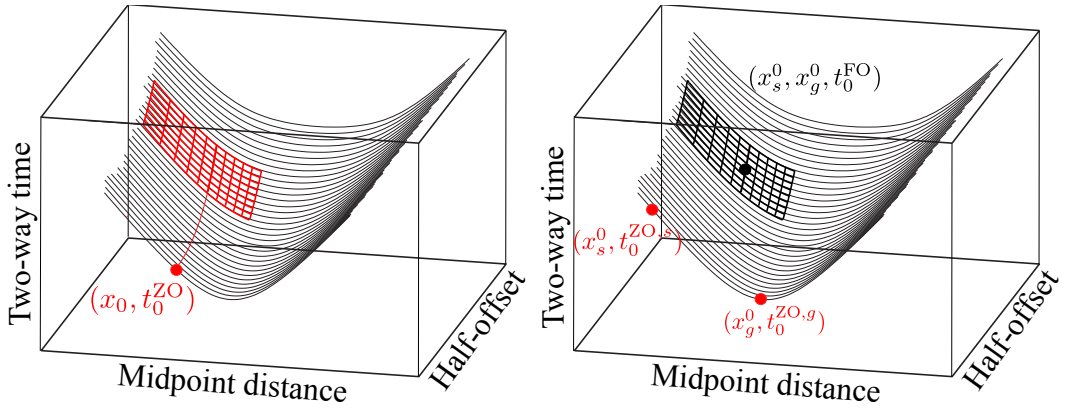

FIGURE 2.2: *The partial CRS stacking surface (a) is based on global application of zero-offset operators. The FO prediction stacking surface (b) is based on a finite-offset operator, which is constructed by two independent zero-offset diffraction operators at a source x_s^0 and a receiver x_g^0.*

measurements carried out at x_s^0 and x_g^0, as illustrated in Figure 2.1c. Based on the assumption of reciprocity, which is valid for diffractions even in highly complex media, comparing equations (2.4) and (2.7) leads to the following system of equations (assuming a consistent choice of near-surface velocities):

$$\alpha_s = \alpha_0^s \,, \tag{2.8a}$$

$$\alpha_g = \alpha_0^g \,, \tag{2.8b}$$

$$R_s = R_{NIP}^s \,, \tag{2.8c}$$

$$R_g = R_{NIP}^g \,. \tag{2.8d}$$

The superscripts s and g indicate the zero-offset attributes measured at the central source and receiver position, respectively (compare Figure 2.1c). This system of equations establishes the relations between zero-offset and finite-offset diffraction attributes. Also the finite-offset reference traveltime can be expressed by the two zero-offset reference traveltimes,

$$t_0^{FO} = \frac{t_0^{ZO,s} + t_0^{ZO,g}}{2} \,. \tag{2.9}$$

Relations (2.8) and (2.9) indicate the redundancy of zero-offset and finite-offset information and thus allow the decomposition of any finite-offset operator into two independent zero-offset operators at a source x_s^0 and a receiver x_g^0 (Schwarz et al., 2014a),

$$t_{FO}(x_s^0, x_g^0, t_0^{FO}, \alpha_s, \alpha_g, R_s, R_g) = \frac{t_{ZO}(x_s^0, t_0^{ZO,s}, \alpha_0^s, R_{NIP}^s)}{2} + \frac{t_{ZO}(x_g^0, t_0^{ZO,g}, \alpha_0^g, R_{NIP}^g)}{2} \,. \tag{2.10}$$

Since the traveltime decomposition principle is a fundamental property of diffractions, Equation (2.10) holds independently of the choice of zero-offset operators. If, e.g., hyperbolic operators such as (2.1) are used during the zero-offset processing, the finite-offset diffraction operators composed according to (2.10) correspond to double square root operators (Yilmaz, 2001), in which the two square roots are approximated independently.

Given the results from zero-offset processing are accurate, the introduced decomposition principle is exact for diffractions in arbitrary media and therefore we also refer to it as *finite-offset prediction for diffractions*. Figure 2.2b shows an example of a stacking surface constructed using the traveltime decomposition method. Note that this decomposition principle is only valid for diffractions, because it is based on the assumption of decoupled up- and downgoing raypaths. In the reflection case, the previously introduced equations do not hold.

2.3 Applications

2.3.1 Diffraction traveltime fit

In order to confirm the redundancy of zero-offset and finite-offset information, we carried out a diffraction traveltime fit on a simple synthetic model containing vertical and lateral heterogeneity by predicting finite-offset traveltimes and attributes solely based on a zero-offset fit and comparing the results to the generic finite-offset reference. The synthetic model consists of a plane interface at a depth of 300 m and a circular discontinuity with a radius of 5 km, whose top point lies at a depth of 400 m. The velocities are 2 km/s above the plane interface, 3 km/s below the interface and 3.5 km/s inside the circular discontinuity. At a depth of 1 km and a lateral position of 5 km we placed a point diffractor. The model and the reference traveltimes were generated with the NORSAR raytracing software. The traveltime fits were computed for each central source and receiver pair (x_s^0, x_g^0) with MATLAB using a Nelder-Mead optimization scheme (Nelder and Mead, 1965) to find those wavefield attributes that minimize the traveltime error. For the computation of traveltime fitting surfaces in the zero-offset and finite-offset domain, the full parabolic traveltime formulations (2.2) and (2.6) were used.

Figures 2.3a and 2.3b show the obtained emergence angles at the source α_s for FO prediction and the generic finite-offset fit, respectively. The corresponding receiver attributes are not shown, since the general behavior is the same. Although it is only based on the results of a zero-offset traveltime fit, the traveltime decomposition approach almost perfectly reproduces the attributes which were obtained from a generic finite-offset fit performed for each finite-offset reference ray (corresponding to one sample of the plot). The symmetry in the results clearly shows the expected redundancy of zero-offset and finite-offset information for the diffraction case, which permits the prediction from zero-offset to finite-offset.

The traveltime errors of FO prediction and the generic finite-offset fit are displayed in figures 2.3c and 2.3d. Each sample of these plots shows the RMS traveltime error of the traveltime surface used for the fit at the corresponding central location. As expected from the theory, the misfit of FO prediction is identical to the one of the generic FO fit. This indicates that the introduced method is exact for diffractions, that is, it is possible to obtain the exact finite-offset wavefield attributes by combining zero-offset attributes according to the introduced decomposition relations. The observed small errors can be explained by inaccuracies of the second-order traveltime approximation. Figure 2.4 shows the traveltime errors of FO prediction and the misfit resulting from global application of zero-offset operators, which corresponds to the partial CRS method. The results clearly reveal the advantages of the new method. Whereas the misfits coincide in the zero-offset section, partial CRS rapidly loses accuracy in offset direction due to the global application of zero-offset operators. However, the magnitude of the FO prediction error does not increase with offset, although both methods use exactly the same input.

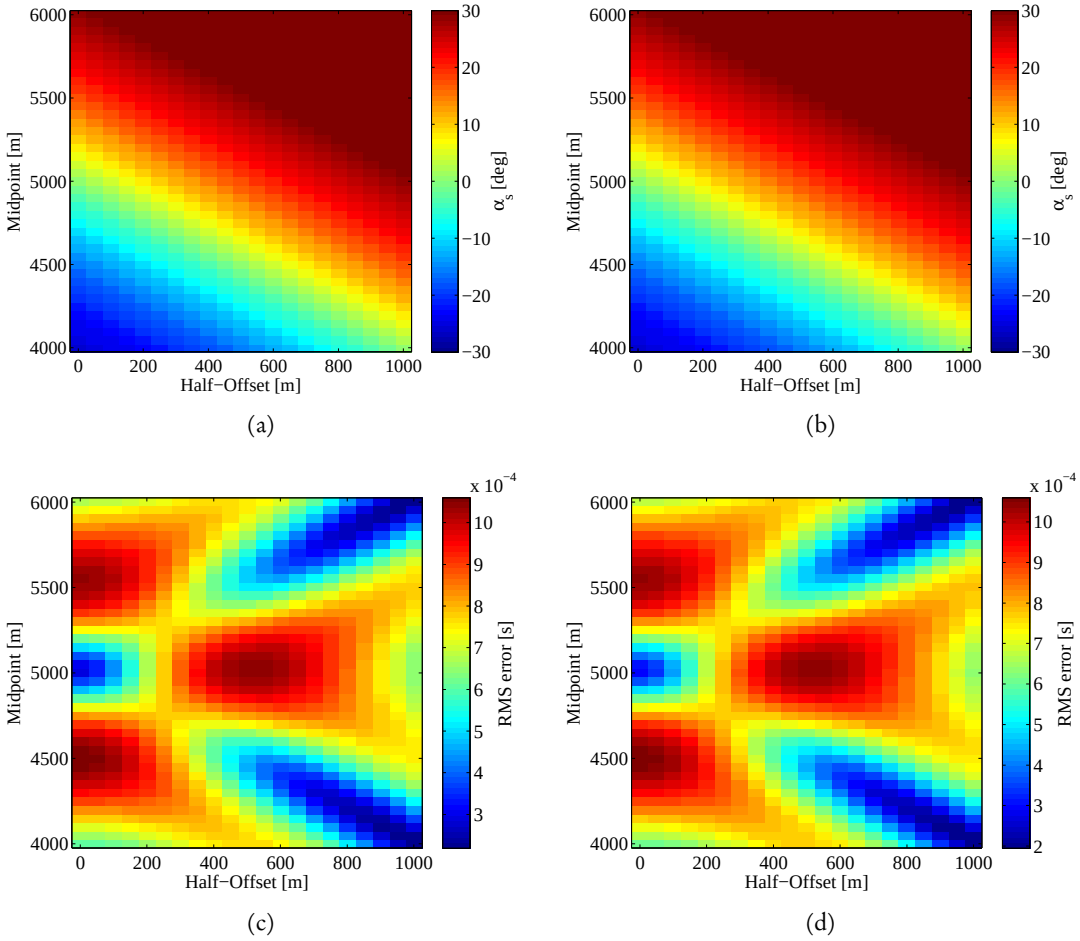

Figure 2.3: *Above: Emergence angles at the source α_s obtained from a) FO prediction and b) generic finite-offset fit. Below: Traveltime errors of c) FO prediction and d) generic finite-offset fit at the same scale. Each sample of the plots corresponds to the RMS traveltime error of one fit.*

Due to the significantly smaller number of traveltime fits, the traveltime decomposition approach only required 0.4 % of the time the full finite-offset fitting needed to produce the same results in this study. Indeed, a challenging task of the traveltime decomposition is the matching of the two events stemming from the same diffractor at source and receiver, which is not required during traveltime fitting.

2.3.2 Implementation

For the application to waveform data, we implemented the new diffraction traveltime decomposition approach into the zero-offset CRS workflow (Mann, 2002). As input, FO prediction requires the prestack data and results of the optimized zero-offset CRS stack, namely the optimized semblance and the attribute sections of the zero-offset wavefield attributes α_0 and R_{NIP}. In order to predict a finite-offset trace for the half-offset h_0 at the midpoint $x_m = x_0$, information from the locations $x_s^0 = x_0 - h_0$ and $x_g^0 = x_0 + h_0$ in the zero-offset section is required. At these

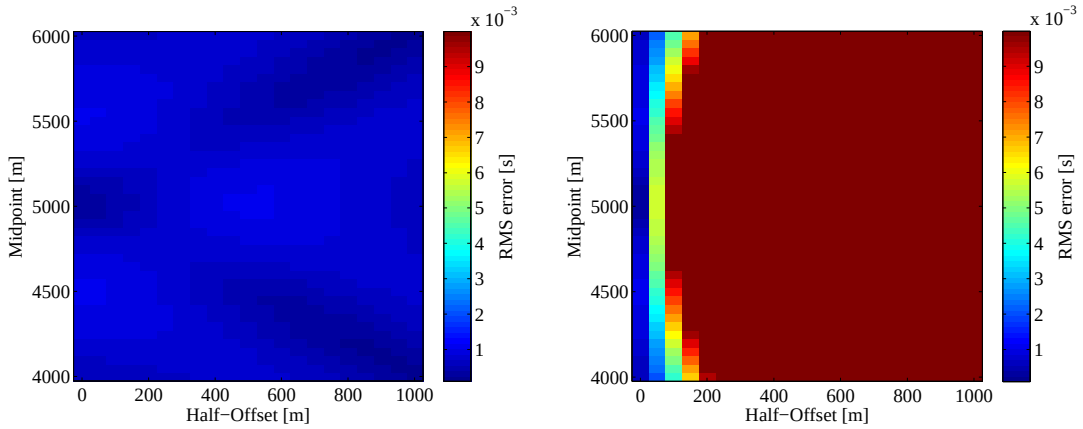

Figure 2.4: *Traveltime errors of a) FO prediction and b) global application of zero-offset operators plotted at the same logarithmic scale. Each sample of the plots corresponds to the RMS traveltime error of one fit.*

locations, the two events which stem from the same diffractor have to be found and matched. In this implementation, different event combinations are tested in order to find the one which provides the best fit. For each sample t_0^{FO} of the finite-offset trace, the source and receiver traces are searched for the corresponding diffraction events using relation (2.9). For the traveltime difference Δt_0 between two matching events the relation

$$\Delta t_0 \leq \frac{2h_0}{v_0} \tag{2.11}$$

holds and the event search may be confined. For each event pair found, the four finite-offset wavefield attributes are extracted from the zero-offset attribute sections. They define the finite-offset diffraction operator for (x_0, h_0, t_0^{FO}). The parameters are tested for accuracy by computing the coherence for the constructed operator. In contrast to the generic finite-offset CRS stack, only the already estimated zero-offset attribute pairs at source and receiver need to be combined.

As output, FO prediction provides the finite-offset stacks, the respective semblance and the four finite-offset attribute sections for the predefined range of offsets. The method is able to handle an arbitrary number of conflicting events, if they are provided with the zero-offset results.

2.3.3 Simple waveform example

In order to verify the proposed method on waveform data, we applied it to a simple dataset based on the same velocity model as the diffraction traveltime fit, but this time containing an additional diffractor at a depth of 1.5 km and lateral position of 3.5 km. The dataset contains a total of 401 CMPs and both the lateral extension of the seismic line and the maximum offset are 5 km. Figure 2.5 compares various finite-offset semblance sections ranging from 500 m to 4000 m offset provided by FO prediction and the zero-offset-based partial CRS method (Baykulov and Gajewski, 2009). The results clearly reveal that the zero-offset operators used by partial CRS (Figure 2.5b) lose accuracy with increasing offset, because they extrapolate traveltimes. However, the FO prediction results (Figure 2.5a) are of very high quality along the whole offset range, because

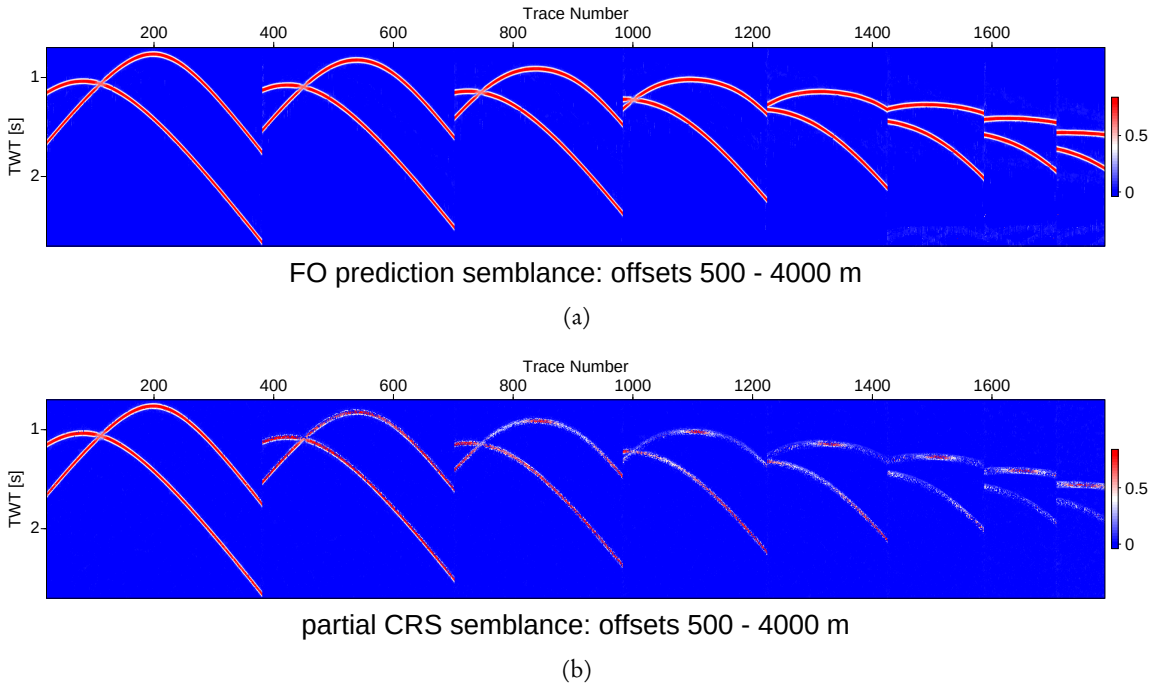

Figure 2.5: *Finite-offset semblance sections of the simple waveform data for eight offsets from 500 (left) to 4000 m (right) generated by application of (a) the new diffraction traveltime decomposition approach and (b) the partial CRS method.*

the decomposed finite-offset operators are accurate for arbitrary offsets. The decomposition relations directly connect zero-offset and finite-offset diffraction traveltimes and attributes and thus define the diffraction moveout globally, while the respective zero-offset-based operators are only accurate in local vicinities of each zero-offset reference ray.

2.3.4 Complex data example

As a next step, we applied the diffraction traveltime decomposition approach to the synthetic Sigsbee 2A dataset. The key feature of this acoustic marine 2D model is a large homogeneous salt body, which is surrounded by sedimentary layers (see Figure 2.6). The rugged top of the salt body causes a significant amount of diffracted energy in the dataset. In addition, the model contains two horizontal lines of diffractors within the sedimentary layers to the left of and below the salt body and several fault structures. The dataset is modeled without a free surface, which is why it does not contain any surface-related multiple reflections. For the results provided in this work we used an excerpt of 400 CMPs taken from the complex part of the model (as indicated by the dotted lines in Figure 2.6), which contains both strong top of salt diffractions and diffracted energy from the subsalt area.

As in the previous examples, we applied partial CRS (Baykulov and Gajewski, 2009) and the new diffraction traveltime decomposition approach (FO prediction) to the data. The previous zero-offset CRS processing was carried out using a global optimization scheme for the attribute search (Walda and Gajewski, 2015) which accounted for a maximum of nine conflicting events at each sample. Both methods under investigation were applied with the same stacking apertures

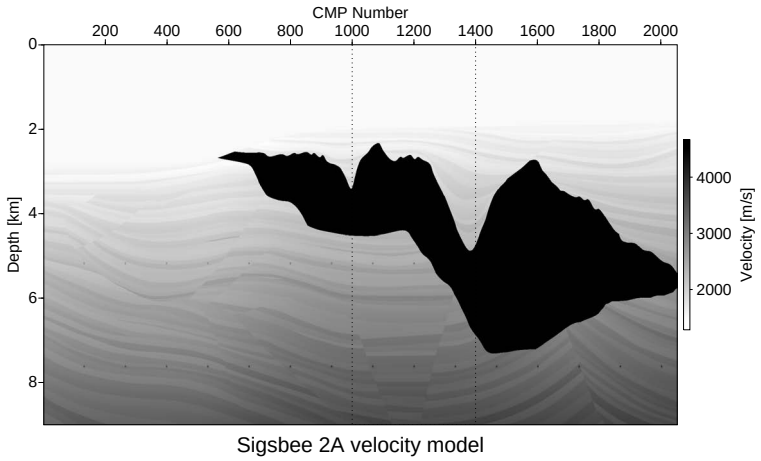

Figure 2.6: *The Sigsbee 2A velocity model. The dotted lines indicate the excerpt which was used for the results shown in this work.*

and processing parameters. Four different finite reference offsets ranging from 1 km to 7 km in steps of 2 km were considered. For a qualitative comparison of the emergence angle α_s to its generic reference we also applied full finite-offset CRS processing (Zhang et al., 2001) to the data.

Figure 2.7 shows FO stacks of all four offsets for two different time ranges. The upper closeups (Figures 2.7a and 2.7b) are taken from 4 to 7 s, that is, the top of salt area. Whereas the traveltime decomposition approach allows us to image diffracted energy well up to the largest offset, partial CRS is only able to fit the strong top of salt diffractions at small offsets. Weaker events are hardly visible and with increasing offset all diffracted events become more blurry. Reflections, however, are still fitted with reasonable quality by partial CRS, whereas the traveltime decomposition inherently suppresses them due to the application of pure diffraction operators (compare the seafloor reflections visible at 5 km and 7 km offset). The closeups displayed below (Figures 2.7c and 2.7d), which were plotted with a smaller clip than the upper ones, are taken from 8 to 11 s and accordingly contain events stemming from the subsalt area. In general, we observe the same behavior as before: whereas the traveltime decomposition approach reveals a high imaging potential for diffractions throughout the whole offset range, the partial CRS stacks are of reasonable quality for small offsets, but become increasingly distorted at larger offsets, where the method fails to image weak events.

In order to evaluate the reliability of our result it is feasible to take into account the semblance coefficient, which serves as a good indicator of successful operator fit. Figure 2.8 displays the finite-offset semblance sections of the full time range of the dataset for the same four offset configurations as obtained by the new diffraction traveltime decomposition approach (left) and partial CRS (right). A comparison of the two images reveals the differences in the ability to find coherent energy in the data. Whereas our new approach images coherent diffracted energy throughout all offsets, partial CRS fails to accurately describe diffracted energy with increasing offset. Moreover, the total energy in the subsalt area is considerably higher for the prediction approach when compared to partial CRS, which should contribute to improved subsalt imaging. However, the reflections from the seafloor and the upper sedimentary layers are more coherent in the partial CRS results, whereas the traveltime decomposition inherently suppresses them. This effect becomes more apparent with increasing offset.

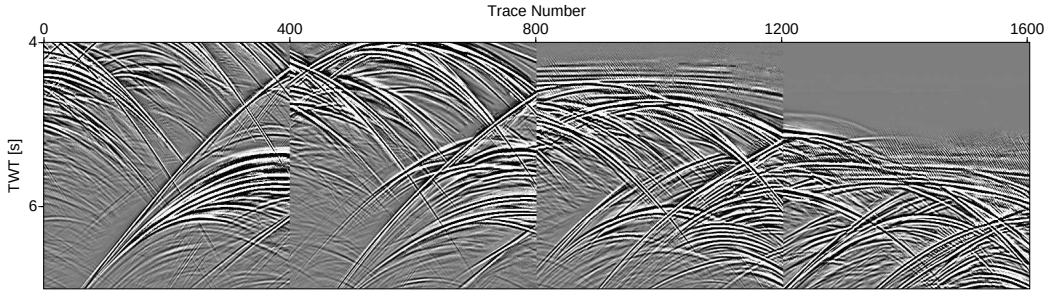

FO prediction: offsets 1000, 3000, 5000, 7000m

(a)

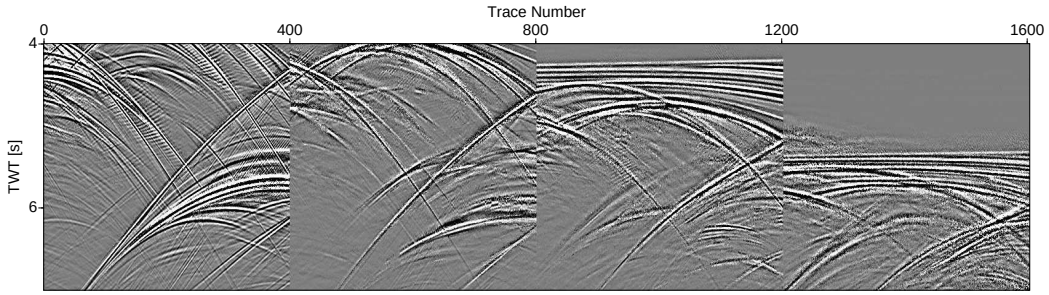

partial CRS: offsets 1000, 3000, 5000, 7000m

(b)

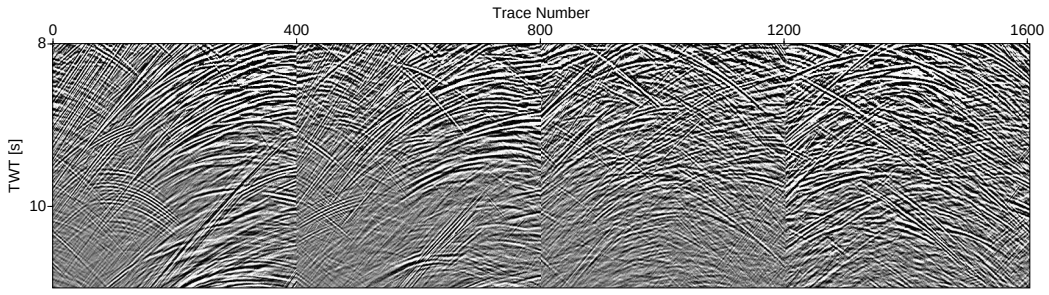

FO prediction: offsets 1000, 3000, 5000, 7000m

(c)

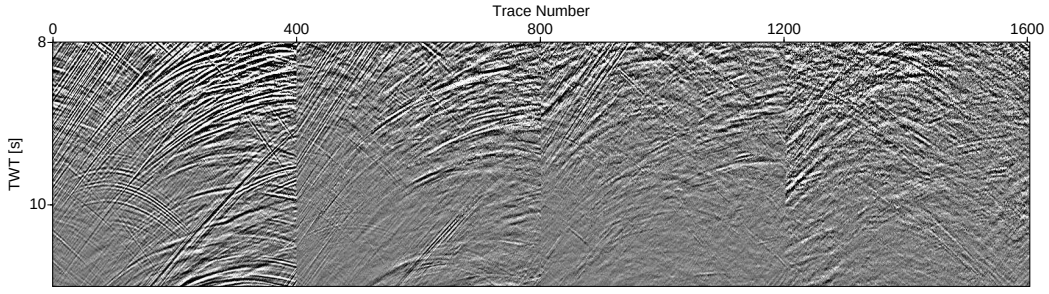

partial CRS: offsets 1000, 3000, 5000, 7000m

(d)

Figure 2.7: *Excerpts of finite-offset stacked sections of Sigsbee 2A for four offsets from 1000 (left) to 7000 m (right) from the top of salt area (above) and the subsalt area (below) generated by application of the new diffraction traveltime decomposition approach (a,c) and the partial CRS method (b,d).*

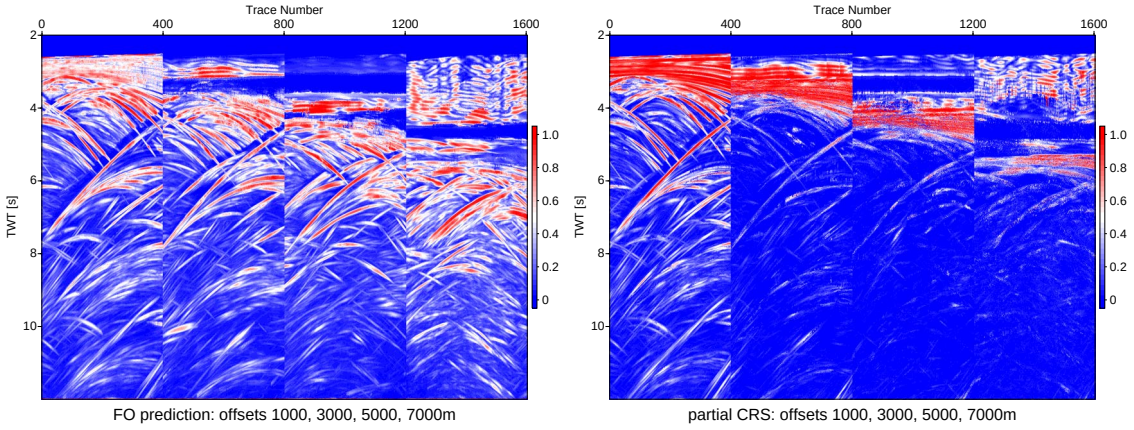

Figure 2.8: *Finite-offset semblance sections of Sigsbee 2A for four offsets from 1000 (left) to 7000 m (right) generated by application of (a) the new diffraction traveltime decomposition approach and (b) the partial CRS method.*

An advantage of the traveltime decomposition is that the new approach, unlike partial CRS, provides the four finite-offset diffraction attributes (emergence angle and NIP-wavefront curvature at source and receiver, respectively) without any further optimization. Since the decomposition principle (2.10) is exact for diffractions, the attributes coincide with the respective estimates obtained from generic finite-offset processing. In this fashion, we can exploit the stability of zero-offset processing to obtain high-quality diffraction attributes for arbitrary offsets. To assess the quality and reliability of the obtained attributes we compare them to results from generic finite-offset CRS processing. Figure 2.9 exemplarily shows the emergence angle at the source α_s as obtained from the zero-offset-based diffraction traveltime decomposition (left) and from generic finite-offset CRS processing (right, Zhang et al., 2001) for the same data excerpt and offset configurations. Note that this is a qualitative comparison, because the algorithms differ and processing parameters cannot be chosen the same, which makes a quantitative comparison inequitable. Nevertheless, the results reveal the high quality of the emergence angle obtained from application of the new traveltime decomposition approach. The zero-offset-based attribute appears more stable and smooth, whereas the one provided by full finite-offset processing reveals stronger distortions, especially for weak events. A comparison of the attribute values of events, which are imaged by both methods, reveals that they coincide. This suggests that the decomposition principle is able to provide reliable prestack diffraction wavefield attributes, which may be used e.g. in the context of prestack stereotomography (Billette and Lambaré, 1998). Note that the angle values along the imaged reflections from sedimentary layers are only reliable if they are obtained from generic finite-offset processing, because the decomposition principle only works for diffractions.

2.4 Conclusions and outlook

We have introduced a universal traveltime decomposition principle for diffractions, which is based on the decoupling of diffraction raypaths. As a result of this decoupling, the kinematic diffraction response is highly symmetric and thus, zero-offset and finite-offset information is

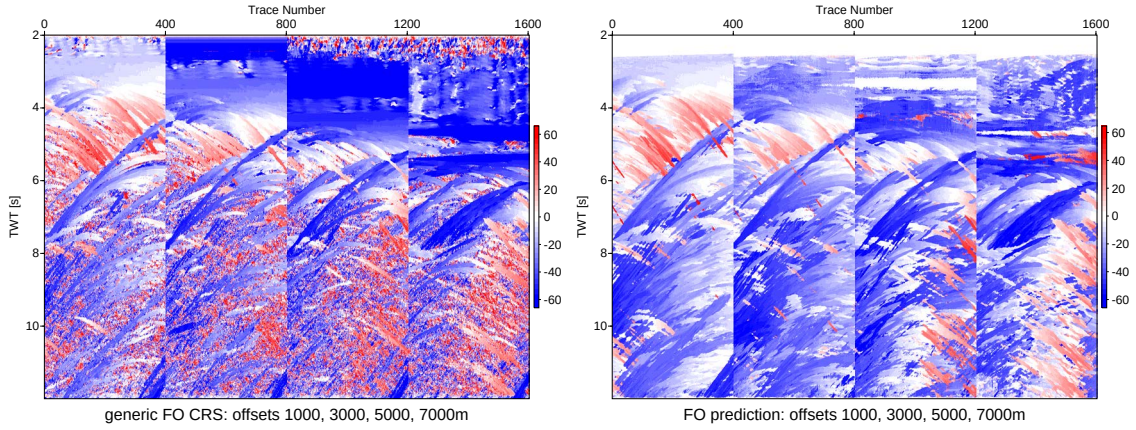

(a) (b)

Figure 2.9: *Finite-offset emergence angle at the source α_s [°] of Sigsbee 2A for four offsets from 1000 (left) to 7000 m (right) generated by application of (a) the new diffraction traveltime decomposition approach and (b) generic finite-offset CRS processing.*

redundant for diffractions. We found that every finite-offset diffraction operator can be decomposed into two independent zero-offset diffraction operators. In this fashion, we are able to image diffractions at arbitrary finite-offsets without loss of accuracy and solely based on zero-offset processing results. We proved the accuracy of the introduced relations by fitting diffraction traveltimes from heterogeneous media and comparing the results in terms of misfit and attributes to the finite-offset reference. In the context of the common-reflection-surface (CRS) stack (Jäger et al., 2001; Zhang et al., 2001), we used the traveltime decomposition principle to enhance prestack diffraction data and to obtain prestack diffraction wavefield attributes, which can be used for inversion. The results on simple waveform data showed the method's ability to fit diffractions at arbitrary offsets using only zero-offset attributes as input. Subsequent application to complex data confirmed the potential of the method for the enhancement of prestack diffraction data and attributes.

Since our method is entirely zero-offset based, it benefits from every improvement in the zero-offset processing. The use of zero-offset attributes obtained from a global optimization scheme with improved conflicting dip handling (Walda and Gajewski, 2015) has increased the quality of our results. Also, the application of non-hyperbolic operators such as i-CRS (Schwarz et al., 2014b) may lead to further improvement. Future work also includes the extension of the decomposition principle to 3D. For a point diffractor, this extension is straightforward. However, at structures such as edge or line diffractors, the decomposition principle is only applicable within that subset of directions, where the structure acts as a point diffractor. In addition, the unique properties of diffractions such as improved illumination and decoupling of raypaths are promising for the successful development of a diffraction-based tomographic scheme, which unites the efficiency of NIP-wave tomography (Duveneck, 2004b) and the improved resolution of prestack stereotomography (Billette and Lambaré, 1998).

Acknowledgments

This work was kindly supported by the sponsors of the *Wave Inversion Technology (WIT) Consortium*, Hamburg, Germany, and is part of the project *Imaging steep structures with diffractions* funded by the German Federal Ministry of Economic Affairs and Energy (BMWi 0325363C). For the generation of reference traveltimes, the NORSAR-3D raytracing software was used. The traveltime fit was carried out with MATLAB. The synthetic Sigsbee 2A dataset was provided by the *Subsalt Multiples Attenuation and Reduction Technology Joint Venture* (SMAART JV). We would like to thank the editor in chief Ivan Pšenčík, the associate editor Leo Eisner and the two reviewers Alexey Stovas and Dmitry Alexandrov for their valuable comments during the revision process.

3 Utilizing diffractions in wavefront tomography

Abstract

Wavefront tomography is known to be an efficient and stable approach for velocity inversion, which does not require accurate starting models and does not interact directly with the prestack data. Instead, the original data is transformed to physically meaningful wavefront attribute fields. These can be automatically estimated using local coherence analysis by means of the common-reflection-surface (CRS) stack, which has been shown to be a powerful tool for data analysis and enhancement. In addition, the zero-offset wavefront attributes acquired during the CRS stack can be used for sophisticated subsequent processes such as wavefield characterization and separation. Whereas in previous works, wavefront tomography has been applied mainly to reflection data, resulting in smooth velocity models suitable for migration of targets with moderately complex overburden, this work has the emphasis on utilizing the diffracted contributions in the data for velocity inversion. By means of simple synthetic examples we demonstrate the potential of diffractions for velocity inversion. On industrial field data we suggest a joint inversion based on reflected and diffracted contributions of the measured wavefield, which confirms the general finding that diffraction-based wavefront tomography can help to increase the resolution of the velocity models. Concluding this work, we compare the quality of a reverse-time migrated result using the estimated velocity model with the result based on the inversion of reflections, which reveals an improved imaging potential for a complex salt geometry.

3.1 Introduction

The estimation of seismic velocities plays a central role in physically characterizing the Earth's interior on scales ranging from the exploration of hydrocarbon reservoirs in local regimes of the crust up to global investigations of the Earth's deeper mantle and core (e.g., Romanowicz, 2003). Besides their potential to answer fundamental geodynamical questions, seismic velocity models are also needed for the migration of recorded seismic data to the depth domain, which leads to structurally rich images of back-scattering impedance contrasts in the subsurface (Claerbout, 1970). In recent years, the direct inversion of full broadband waveforms has become the primary tool for inferring the velocity structure with the highest possible resolution (Tarantola, 1984). Although being based on principles, which were already defined in the eighties, full-waveform inversion (FWI) is still computationally highly demanding and in 3D can only be afforded by processers with access to high-performance computing facilities (e.g., Virieux and Operto, 2009). In addition, current implementations still mostly have to rely on large-offset acquisitions of diving waves with low frequencies or reasonably accurate starting velocity models to ensure stable convergence to the global misfit minimum (Virieux and Operto, 2009). The established process of depth migration, in turn, is designed to provide structural images of high resolution by

focusing the back-scattered, reflected and diffracted contributions of the excited wavefield even at principally small source-receiver offsets. In contrast to full-waveform inversion, imaging performs well for comparably smooth models with less detail in the velocity structure (e.g., Yilmaz, 2001).

While full-waveform inversion and depth migration in principle do not require a dense distribution of sources and receivers, Billette and Lambaré (1998) and Duveneck (2004b) have introduced tomographic inversion techniques that exploit redundancy in the data, which is common in modern seismic acquisitions. These techniques can be formulated either in the pre- or in the poststack domain and rely on the local coherence of the recorded wavefield. Prestack stereotomography incorporates the wavefield's traveltimes, and, in addition to conventional traveltime tomography, its local slopes in the inversion (Billette and Lambaré, 1998). While this local description, in principle, allows for a high resolution in the inverted models, the poststack approach offers the benefits of a decreased noise level and data reduction, which can help to speed up and stabilize the process (Lavaud et al., 2004). The multi-dimensional common-reflection-surface (CRS) stack (Jäger et al., 2001) is a tool, which not only aims at optimally utilizing the redundancy in the data, but also automatically extracts valuable first- and second-order wavefront attributes, which can be used directly for automatic velocity inversion (Duveneck, 2004b). In contrast to prestack stereotomography, this CRS-based wavefront tomography relies on a second-order symmetry of the kinematics of the wavefield in the common-midpoint (CMP) gather, which can be expressed by an auxiliary one-way wave originating at the normal-incidence point (NIP) of the central ray (Hubral, 1983).

While previous applications had a strong emphasis on reflected events (Duveneck, 2004b; Dümmong et al., 2008), we aim to take into account the diffractions in the data. Since diffractions are the seismic response of small-scale structures, they are crucial for high-resolution imaging of the subsurface (Klem-Musatov et al., 1994; Moser and Howard, 2008; Dell and Gajewski, 2011). Santos et al. (2012) propose to make use of diffractions in the framework of tomographic inversion based on common-focus-point operators (CFPOs). Recent works indicate that for diffractions, poststack attributes can be used to accurately describe the full kinematics of the prestack response (Schwarz et al., 2014a; Bauer et al., 2016a), which suggests a potential for increased resolution and stability of wavefront tomography. In this work, we make use of the non-Snell scattering contributions in the data for obtaining better-resolved velocity models than with conventional applications, which are generally reflection-based. Starting with simple synthetic examples, we find support of the recently formulated diffraction symmetry. Concluding this paper, we apply wavefront tomography to industrial field data acquired in the Eastern Mediterranean offshore Israel. We propose a joint inversion based on data points picked automatically at high-amplitude reflections as well as data points extracted from diffraction-only data. This promising approach reveals the potential of increased resolution of diffraction-based inversion for a complex salt geometry.

3.2 Common-reflection-surface stack

Wavefront tomography is based on wavefront attributes that can be obtained by means of the zero-offset (ZO) common-reflection-surface (CRS) stack (Jäger et al., 2001), in which a zero-offset section is simulated in an automatic fashion. The ZO CRS stack is a multi-parameter stacking technique, which takes into account traces along a stacking surface in both offset and midpoint

direction around a central midpoint x_0. Thus, the signal-to-noise ratio in the resulting zero-offset section can be significantly reduced without providing any prior model information. The 2D CRS stacking operator depends on three parameters, which can be expressed in terms of the geometrical wavefront attributes α_0, R_{NIP} and R_N (Hubral, 1983). The parameter α_0 describes the emergence angle, at which two fictitious waves emerge at the central midpoint x_0 on the recording surface. The attributes R_{NIP} and R_N describe the wavefront curvatures of these two fictitious waves, the NIP wave and the normal wave, which are excited by a point source placed on the reflector's normal-incidence point (NIP) and an exploding reflector segment around the NIP, respectively. In the case of a diffraction, R_{NIP} and R_N coincide and the NIP-wavefront corresponds to the actual wavefront of the diffraction. This criterion can be utilized for the separation of reflections and diffractions in the resulting zero-offset sections (Dell and Gajewski, 2011). The hyperbolic zero-offset CRS stacking operator is given by (Jäger et al., 2001)

$$t_{ZO}^2 = \left(t_0 + 2p_0\Delta x_m\right)^2 + 2t_0\left(M_N\Delta x_m^2 + M_{NIP}h^2\right) \quad , \tag{3.1}$$

where $\Delta x_m = x_m - x_0$ is the displacement from the central midpoint x_0, h denotes the half-offset and t_0 the traveltime of the central zero-offset ray emerging at x_0. The horizontal slowness of the normal ray can also be expressed in terms of the geometrical wavefront attributes,

$$p_0 = \frac{\sin\alpha_0}{v_0} \quad , \tag{3.2}$$

where v_0 is the constant near-surface velocity. The second derivative of the traveltime in a CMP-gather is then given by

$$M_{NIP} = \frac{\cos^2\alpha_0}{v_0 R_{NIP}} \quad , \tag{3.3}$$

and accordingly for M_N. Although the hyperbolic traveltime operator (3.1) is the most common one, different moveout descriptions, such as multifocusing (Gelchinsky et al., 1999), non-hyperbolic CRS (Fomel and Kazinnik, 2013) or implicit CRS (Schwarz et al., 2014b), can be used to obtain wavefront attributes. At each zero-offset sample (x_0, t_0), values for the three wavefront attributes are determined by coherence analysis (usually, the semblance coefficient (Taner and Koehler, 1969) is used as a measure of coherence) using either a pragmatic approach and subsequent local optimization (Mann, 2002) or a global optimization scheme (Walda and Gajewski, 2015). Also conflicting dips can be considered by estimating more than one operator at each sample (Mann, 2002; Soleimani et al., 2009; Walda and Gajewski, 2015). Since the wavefront attributes obtained from the ZO CRS stack have a physical meaning, they can be exploited for further processing steps, such as diffraction separation (Dell and Gajewski, 2011), prestack data enhancement (Baykulov and Gajewski, 2009; Bauer et al., 2016a) or the tomographic inversion revisited in this paper (Duveneck, 2004b).

3.3 Diffraction symmetry

Since Snell's law does not hold in the case of a point diffractor, diffraction raypaths are decoupled and zero-offset and finite-offset information (Zhang et al., 2001) is redundant for the corresponding traveltime response (Schwarz et al., 2014a; Bauer et al., 2016a). As illustrated in Figure 3.1, the common-shot and common-receiver responses in a finite-offset measurement of a diffraction

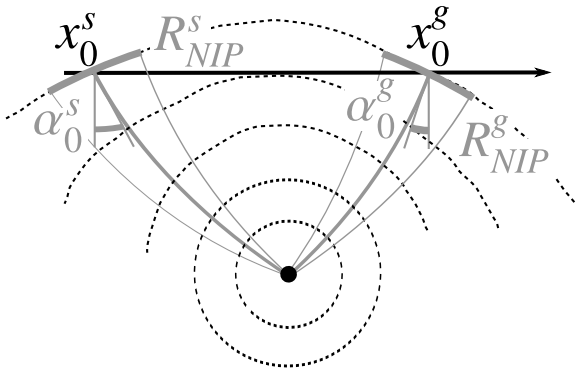

Figure 3.1: *A finite-offset diffraction setting can be described exactly by two independent zero-offset measurements at a source x_0^s and a receiver x_0^g.*

are technically identical to two independent zero-offset measurements carried out at x_0^s and x_0^g. Based on the assumption of reciprocity, which is a model-independent universal principle valid for monotypic waves, it is possible to decompose any finite-offset diffraction operator into two independent zero-offset operators at a source x_0^s and a receiver x_0^g (Schwarz et al., 2014a; Bauer et al., 2016a),

$$t_{FO} = \frac{t_{ZO}(x_0^s, t_0^s, p_0^s, M_{NIP}^s)}{2} + \frac{t_{ZO}(x_0^g, t_0^g, p_0^g, M_{NIP}^g)}{2} \,. \tag{3.4}$$

This traveltime decomposition principle is a fundamental property of diffractions and thus, Equation (3.4) holds independently of the choice of zero-offset operators. If, e.g., hyperbolic operators such as (3.1) are used during the zero-offset processing, the finite-offset diffraction operators composed according to (3.4) correspond to double-square-root operators (Yilmaz, 2001), in which the two square roots are approximated independently. Given the results from zero-offset processing are accurate, the decomposition principle is exact for diffractions in arbitrary media. Note that it is only valid for diffractions, because it is based on the assumption of decoupled up- and downgoing raypaths. Accordingly, Equation (3.4) does not apply in the reflection case.

By utilizing diffractions in the zero-offset-based poststack wavefront tomography we aim to make use of the fact that, unlike the reflection case, the full prestack diffraction response is encoded in its zero-offset measurements, which suggests a potential for improved lateral resolution of the velocity models.

3.4 Wavefront tomography

Wavefront tomography, introduced by Duveneck (2004b), is an efficient tomographic approach, which is entirely based on the zero-offset CRS attributes p_0 and M_{NIP} and provides smooth 2D isotropic velocity models. Previous to the inversion, independent data points are picked in a data-driven way in the CRS semblance section by taking into account stack amplitudes and attribute values. During the tomographic inversion, rays are propagated through the model starting from the picked locations with the respective attribute values. The velocity model is updated according to the criterion that in a correct model, all considered NIP waves focus at zero traveltime.

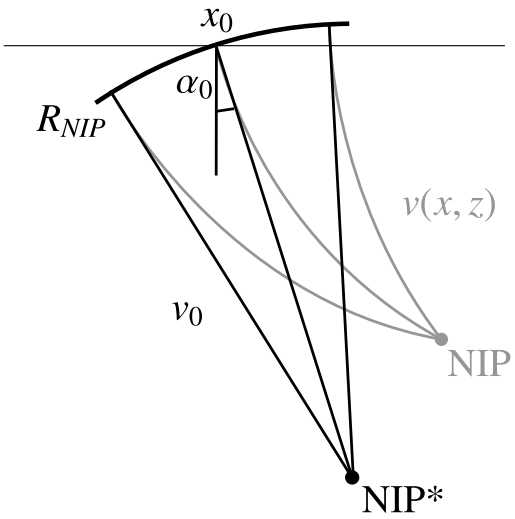

FIGURE 3.2: *The wavefront attributes of the NIP wave are determined in the so-called optical image space (black) by assuming a medium with constant velocity v_0, in which the location NIP* is found by straight-ray projection. By means of wavefront tomography we aim to determine the true velocity model $v(x,z)$ in order to find the NIP wave's true source location (gray).*

3.4.1 INPUT DATA AND MODEL

The input for the inversion are automatically picked data points of the CRS results, which are selected based on their coherence and a number of predefined constraints. Each pick is defined by its location on the recording surface x_0, its zero-offset traveltime t_0 and the wavefront attributes p_0 and M_{NIP} associated with the picked event (see Figure 3.2). Instead of t_0, wavefront tomography considers the one-way zero-offset traveltime

$$T_0 = \frac{t_0}{2} \ . \tag{3.5}$$

Thus, the input data for the inversion algorithm is given by

$$(x_0, T_0, p_0, M_{NIP})_i \quad \text{with} \quad i = 1, \ldots, n_{picks} \ , \tag{3.6}$$

where n_{picks} is the total number of automatically picked data points. Each point i can be associated with an imaginary normal-incidence point NIP* in the subsurface, which for a constant initial model can be obtained by straight-ray projection into the optical image space (see Figure 3.2). Only in a correct velocity model $v(x,z)$, NIP* coincides with the true NIP. In theory, checking if the back-propagated NIP-waves starting from x_0^i with p_0^i for all picks focus at $T_0^i = 0$ is a natural condition for the inversion. However, we have to take into account that the data might be affected by errors in order to ensure stability. Therefore, at every NIP* associated to one data point i, a ray is started in the subsurface by dynamic ray tracing (Duveneck, 2004b). During this process, the true subsurface positions $(x,z)_i$ and the takeoff angles θ_i of the rays must be considered a part of the model, because they are unknown. In order to find the optimum velocity model, wavefront tomography minimizes the misfit between measured and modeled values $(x_0, T_0, p_0, M_{NIP})_i$. Billette and Lambaré (1998) used a similar approach for stereotomography, which is a tomographic inversion method working in the prestack domain.

For the description of the smooth velocity model $v(x,z)$, wavefront tomography uses 2D B-splines,

$$v(x,z) = \sum_{j=1}^{n_x} \sum_{k=1}^{n_z} v_{jk} \beta_j(x) \beta_k(z) \ , \tag{3.7}$$

where n_x and n_z are the total number of knots in x and z-direction, respectively. Accordingly, the model is defined by the B-spline coefficients v_{jk} and the coordinates and ray takeoff angles related to the data points,

$$\begin{aligned} (x,z,\theta)_i \quad &\text{with} \quad i = 1,\ldots,n_{picks} \ , \\ v_{jk} \quad &\text{with} \quad (j,k) = (1,1),\ldots,(n_x,n_z) \ . \end{aligned} \tag{3.8}$$

In order to obtain the desired optimum velocity model, the inverse problem has to be solved iteratively. This process will be described in the following section.

3.4.2 Solution of the inverse problem

In order to solve the inverse problem, the algorithm has to find a model vector $\mathbf{m}$, which minimizes the misfit between a data vector $\mathbf{d}$ and the corresponding modeled values $\mathbf{d}_{\text{mod}} = \mathbf{f}(\mathbf{m})$ (Duveneck, 2004b), where the model vector $\mathbf{m}$ contains all model components (3.8), the data vector $\mathbf{d}$ consists of all picked data points (3.6) and $\mathbf{f}$ is a nonlinear operator, which, in the case of wavefront tomography, corresponds to the dynamic ray tracing carried out in the model. The presented inversion algorithm uses the least-squares norm (Paige and Saunders, 1982; Tarantola, 2005) as a measure of misfit and tries to minimize the objective function given by

$$\Psi(\mathbf{m}) = \frac{1}{2} \|\mathbf{d} - \mathbf{f}(\mathbf{m})\|_D^2 = \frac{1}{2} \Delta\mathbf{d}^T(\mathbf{m}) \mathbf{C}_D^{-1} \Delta\mathbf{d}(\mathbf{m}) \ , \tag{3.9}$$

where $\Delta\mathbf{d}(\mathbf{m}) = \mathbf{d} - \mathbf{f}(\mathbf{m})$. The matrix $\mathbf{C}_D^{-1}$ is symmetric and positive definite and weights the different data components during the calculation of Ψ. Due to the nonlinearity of the operator $\mathbf{f}$, the inverse problem is solved iteratively by locally linearizing $\mathbf{f}(\mathbf{m})$ around the current model vector. For this, the Fréchet derivatives of $\mathbf{f}$ are needed, which can be calculated during forward modeling (Farra and Madariaga, 1987). In order to facilitate a stable inversion, the requirement of a smooth velocity model is implemented as an additional constraint by minimizing its second derivatives. This results in an additional term in the objective function,

$$\Psi(\mathbf{m}) = \frac{1}{2} \Delta\mathbf{d}^T(\mathbf{m}) \mathbf{C}_D^{-1} \Delta\mathbf{d}(\mathbf{m}) + \frac{1}{2} \epsilon'' \mathbf{m}_{(v)}^T \mathbf{D}'' \mathbf{m}_{(v)} \ , \tag{3.10}$$

where $\mathbf{m}_{(v)}$ is the part of the model vector $\mathbf{m}$ containing the velocity coefficients and ϵ'' is a weighting factor, which balances the contributions of the data misfit term and the regularization term to the cost function. The additional term contains the integral

$$\mathbf{m}_{(v)}^T \mathbf{D}'' \mathbf{m}_{(v)} = \int\int \left[\epsilon_{xx} \left(\frac{\partial^2 v(x,z)}{\partial x^2} \right)^2 + \epsilon_{zz} \left(\frac{\partial^2 v(x,z)}{\partial z^2} \right)^2 \right] \mathrm{d}x \, \mathrm{d}z \ , \tag{3.11}$$

where the factors ϵ_{xx} and ϵ_{zz} are used for weighting the contributions of the corresponding second derivatives. The additional term is added in order to ensure that the matrix $\mathbf{D}''$ is positive

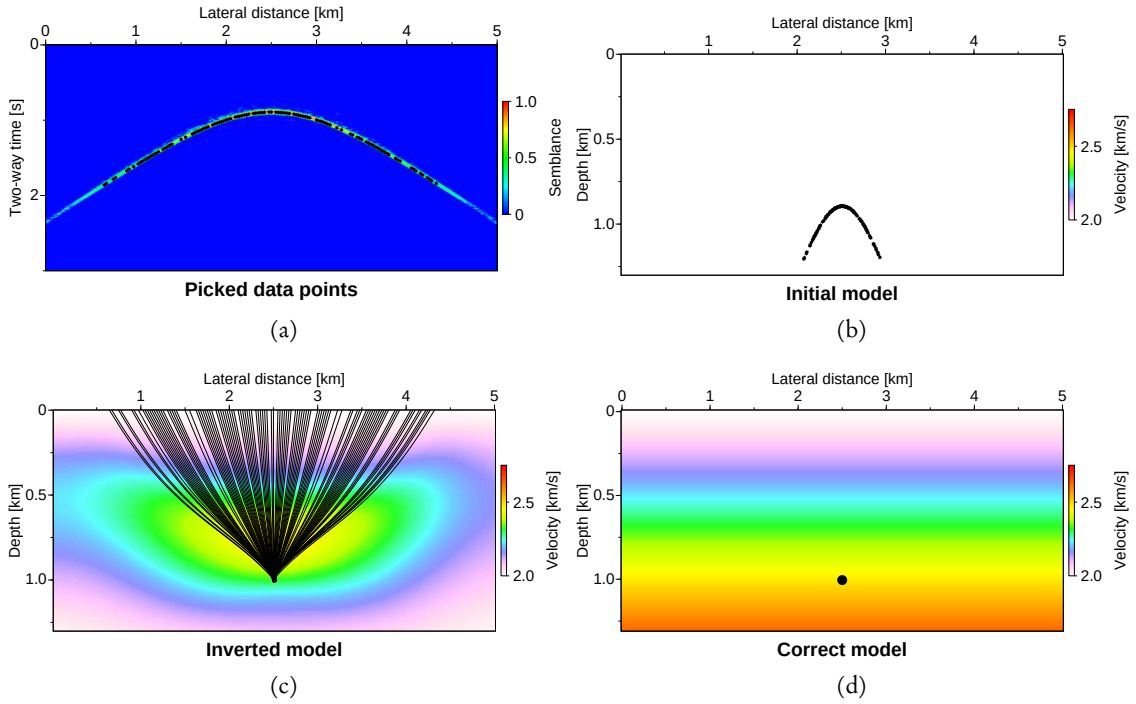

FIGURE 3.3: *Results for simple diffraction data containing one diffractor. (a) All 108 automatically picked data points plotted into the zero-offset semblance section. (b) The constant initial model for the inversion containing the initial ray starting locations. (c) The inverted model with the final ray starting locations and the final ray trajectories corresponding to each data point. (d) The correct velocity model with the position of the diffractor indicated by a black dot.*

definite. For the explanation of the matrix $\mathbf{D}''$ and a more detailed description of the solution of the inverse problem we refer to the work of Duveneck (2004b). Optionally, the weighting factors ϵ_{xx} and ϵ_{zz} may be decreased successively after each iteration by multiplying them with a factor η given by

$$\eta = \sqrt{\frac{\Psi_l}{\Psi_{l-1}}} \ , \tag{3.12}$$

where l is the current iteration and Ψ_l and Ψ_{l-1} the corresponding values of the objective function (3.10) after the current and the previous iteration, respectively.

After setting up an initial velocity model, defined by a constant vertical velocity gradient or a given starting model, kinematic ray tracing for each data point $(x_0, T_0, p_0, M_{NIP})_i$ yields the corresponding coordinates $(x, z, \theta)_i$ in the model. As a next step, the algorithm performs dynamic ray tracing in the upward direction until the rays, which are started at $(x, z)_i$ with the angles θ_i, reach the measurement surface. The updated model for the l-th iteration is then given by $\mathbf{m}_{l+1} = \mathbf{m}_l + \lambda\Delta\mathbf{m}$, where $0 < \lambda \leq 1$ (for more details, see Duveneck, 2004b). In this model, new data values are obtained from dynamic ray tracing and the objective function (3.10) is calculated. If its value decreases with respect to the previous iteration, the next iteration is started. Otherwise, the factor λ is decreased and the objective function is recalculated. If a minimum of the objective function is reached, the calculation is stopped.

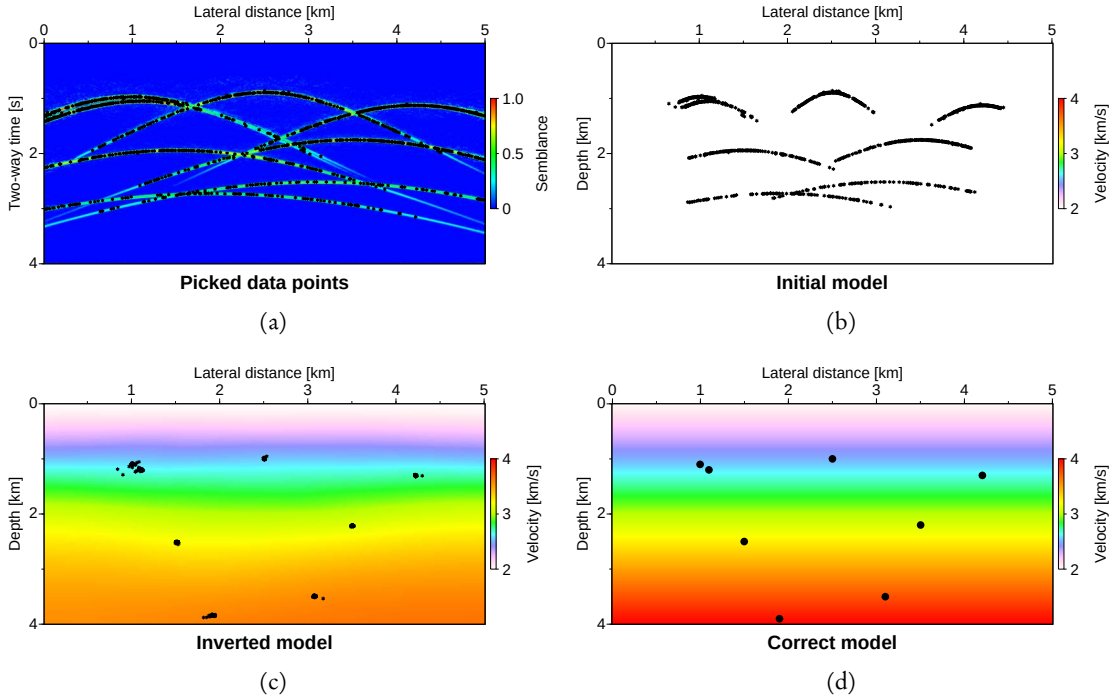

Figure 3.4: *Results for simple diffraction data containing multiple diffractors. (a) All 992 automatically picked data points plotted into the zero-offset semblance section. (b) The constant initial model for the inversion containing the initial ray starting locations. (c) The inverted model with the final ray starting locations. (d) The correct velocity model with the position of the diffractor indicated by a black dot.*

3.5 Simple diffraction data

In previous studies (Duveneck, 2004b; Meier, 2007; Dümmong et al., 2008), wavefront tomography has been applied mainly based on input data points picked on high-amplitude reflections. However, diffraction events possess properties, which make them an interesting target for wavefront tomography. Whereas in the case of a reflection, the NIP wave emerges from a hypothetical point source placed on the reflector's normal-incidence point, in the case of a diffraction, the NIP wave is excited by the diffractor itself and therefore, p_0 and M_{NIP} describe the actual wavefront of the diffraction. Furthermore, diffractions imply better illumination than reflections, because a point diffractor scatters an incoming wave into all directions and thus, contributions stemming from the same diffractor can be recorded within a large part of the recording surface. This means that the rays corresponding to just one diffraction may already travel through a significant part of the model. In addition, the proximity of the starting coordinates of all rays connected to one diffraction serves as a strong quality criterion for the inverted model.

In order to illustrate the procedure, we applied wavefront tomography to a simple dataset containing one diffraction based on a model with a constant vertical velocity gradient of $0.5\,s^{-1}$. The results are displayed in Figure 3.3, where Figure 3.3a shows the data points, which were picked automatically in the zero-offset CRS semblance section. As expected, all 108 picks lie on the diffraction hyperbola. Figure 3.3b shows the initial velocity model for the tomographic

inversion, which merely consists of the near-surface velocity v_0 and no initial vertical velocity gradient. The black asterisks indicate the starting locations of the rays. In a correct velocity model, these locations should coincide for all rays stemming from the same diffractor. In this example, we used 18×18 B-spline knots with a spacing of 250 m in x-direction and 100 m in z-direction for the tomographic inversion. Figure 3.3c shows the inverted model after 13 iterations, the final starting coordinates of the rays and the corresponding ray trajectories. A comparison of the inverted model with the correct one displayed in Figure 3.3d reveals a good agreement in those parts of the model illuminated by the rays. In addition, although all picked data points are treated independently by the algorithm, the final starting locations of the rays are confined to the same depth point, which coincides with the actual position of the diffractor indicated by the black dot in the correct model. Although only a single diffractor was used, the gradient in the illuminated area is already very well reconstructed. By increasing the number of diffractors this result will further improve, which is demonstrated in the next example.

We applied the same workflow to a dataset based on the same background model, but containing a larger number of diffractors at different locations in the subsurface. Figure 3.4 shows the results of this application. In Figure 3.4a, the asterisks indicate the 992 automatically picked data points in the zero-offset CRS semblance section. For the tomographic inversion, we used 26 B-spline knots in x-direction and 21 knots in z-direction with a spacing of 200 m each. As in the previous example, the initial model consisted of the constant near-surface velocity v_0, as displayed in Figure 3.4b, where the starting locations of the rays again indicate the wrong velocity model. The result of the inversion is displayed in Figure 3.4c including the final starting coordinates of the rays. In this example, we stopped the calculation after 50 iterations, because the value of the objective function did not change significantly anymore. The ray trajectories are not displayed in this case for a better visualization of the result. In the inverted model, the ray starting locations are, except for a few outliers, confined nicely to eight distinct depth points, although every data point is treated independently by the inversion. The correct model shown in Figure 3.4d reveals that the inverted depth points coincide very well with the true diffractor positions. Note that even the two diffractors lying close together on the upper left side of the images are distinguishable. Since almost the whole model space is covered by rays, also the background velocity gradient could be well recovered during the inversion.

3.6 Field data

Finally, we applied the same workflow to a marine field dataset recorded by TGS in the Levantine Basin, which is located in the Eastern Mediterranean offshore Israel. The profile considered in this work is characterized by pronounced salt-roller structures in the left part (Hübscher and Netzeband, 2007). In previous studies, Meier (2007) and Dümmong et al. (2008) applied both wavefront tomography and prestack stereotomography (Billette and Lambaré, 1998) to various lines acquired in the same region. However, their results were based on data points mainly picked on high-amplitude reflections. In order to increase the resolution of the resulting velocity models, we propose to take into account diffractions, which usually have lower amplitudes than reflections.

Figure 3.5a shows the zero-offset stack of the dataset under investigation. It was obtained with non-hyperbolic CRS (Fomel and Kazinnik, 2013) using a global optimization algorithm accounting for a maximum of 17 conflicting events at one sample (Walda and Gajewski, 2015). In

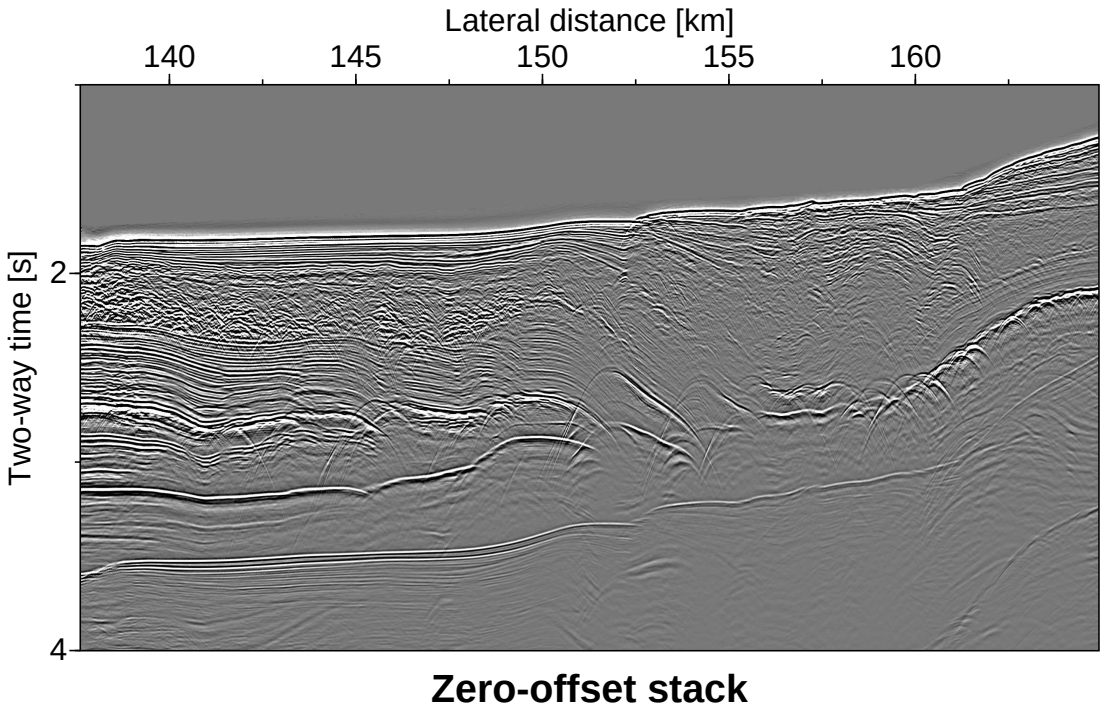

(a)

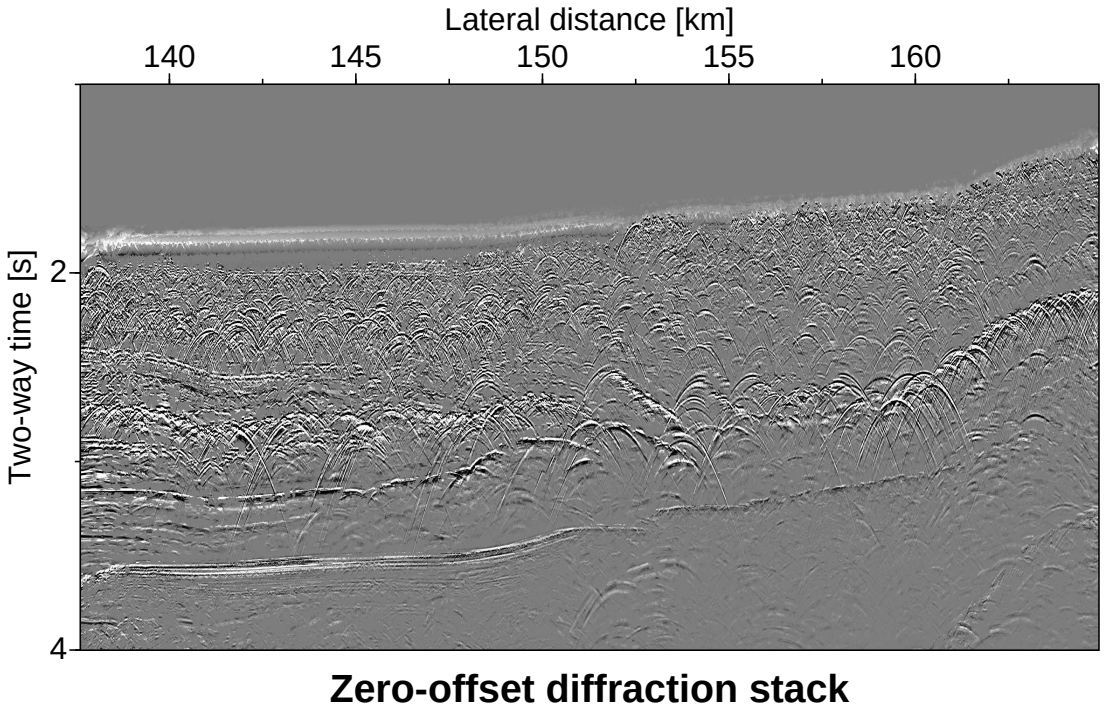

(b)

Figure 3.5: *(a) Zero-offset CRS stack of the investigated marine field data. (b) ZO CRS stack after diffraction separation.*

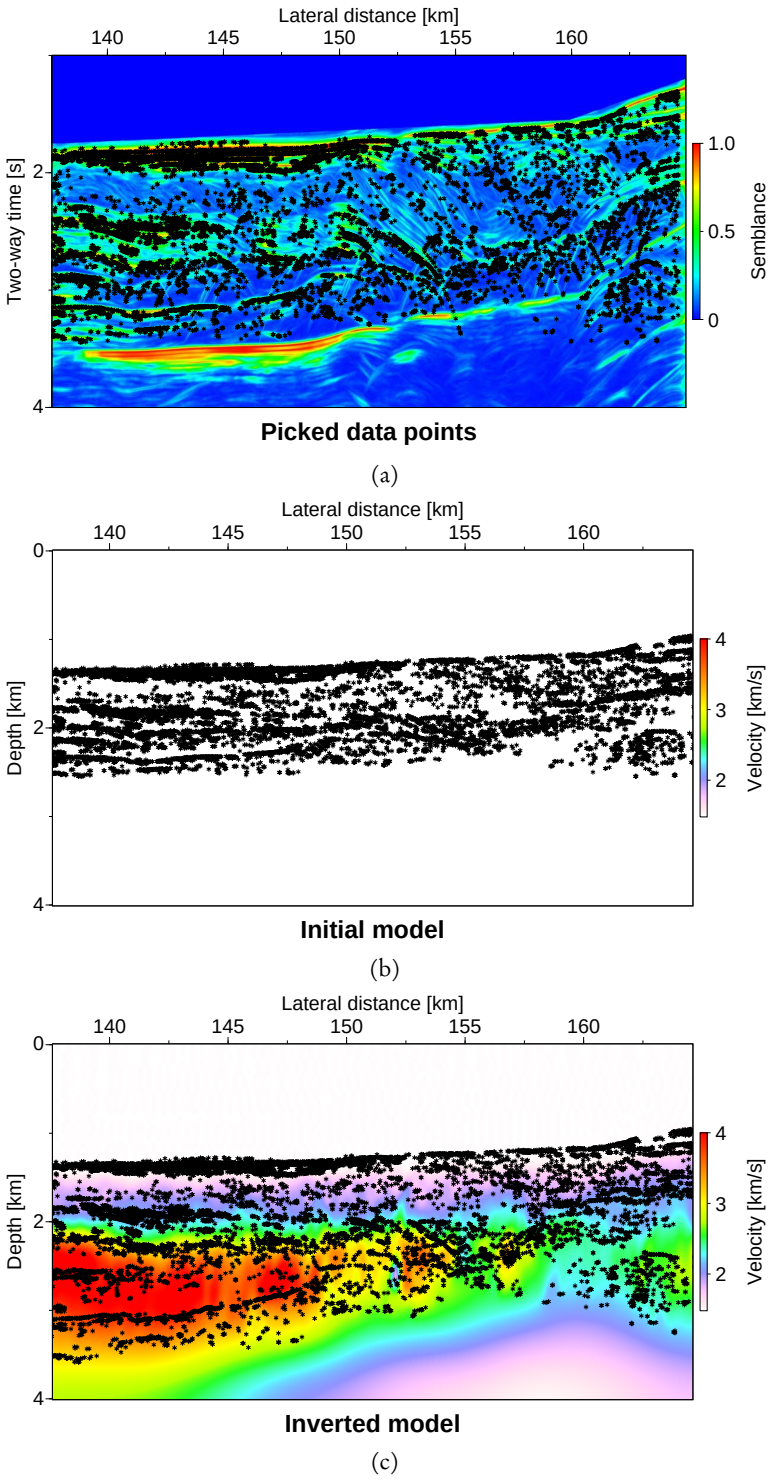

Figure 3.6: *Field data results. (a) All 11955 automatically picked data points plotted into the zero-offset semblance section. (b) The constant initial model for the inversion containing the initial ray starting locations. (c) Resulting model of the joint inversion using both reflection and diffraction picks overlain with the final ray starting locations.*

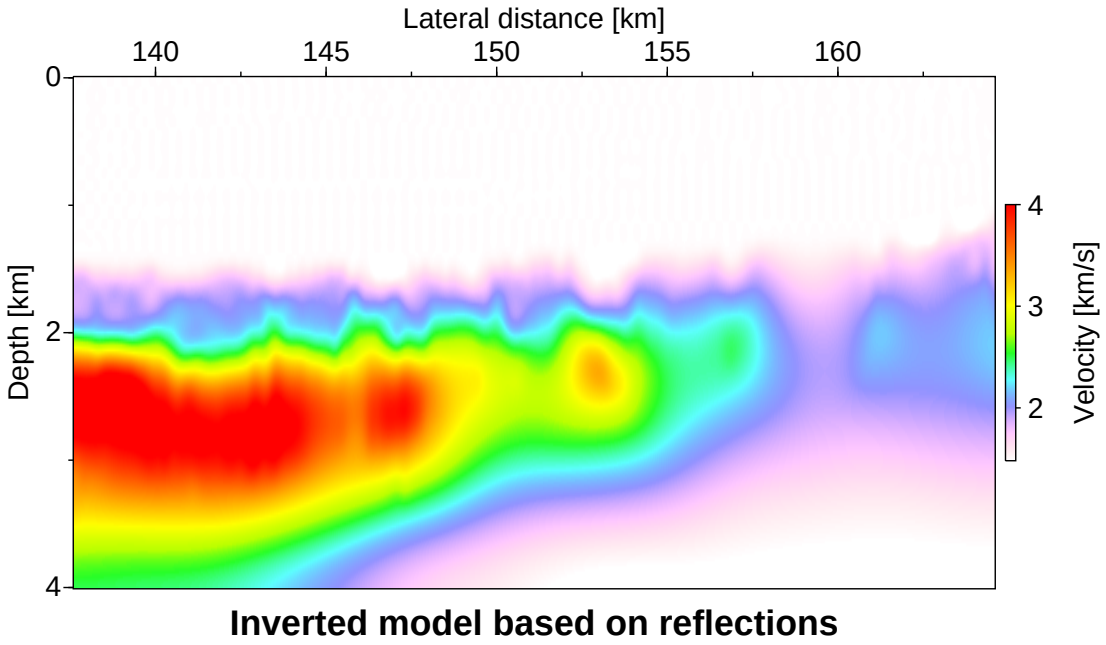

(a)

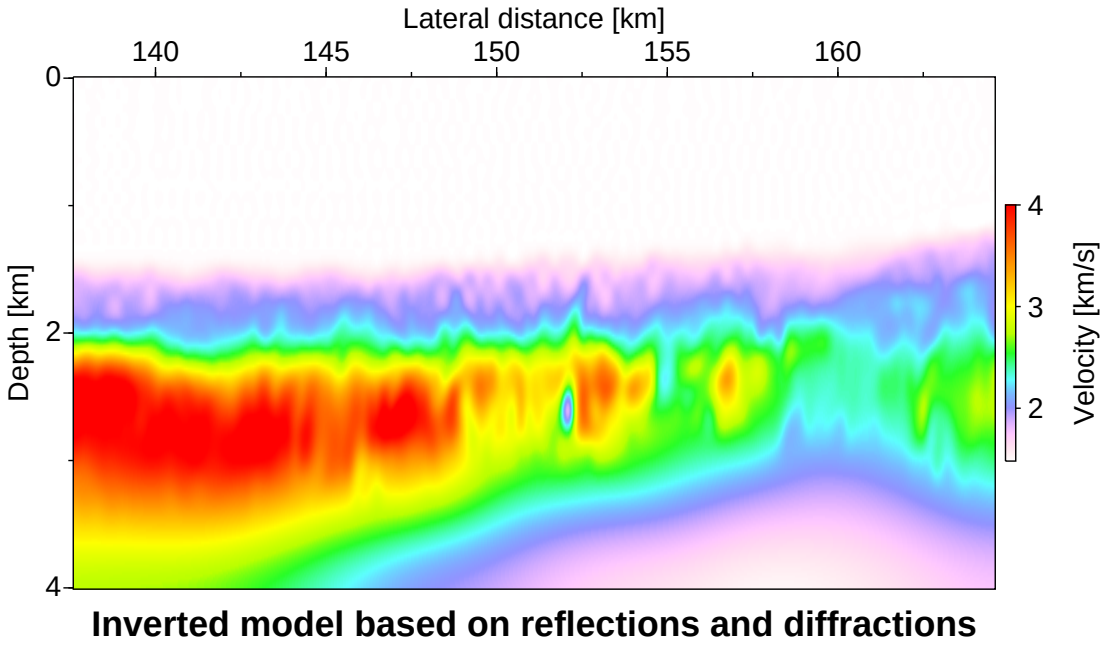

(b)

Figure 3.7: *Velocity models obtained by (a) inversion of only reflections and (b) joint inversion of reflections and diffractions.*

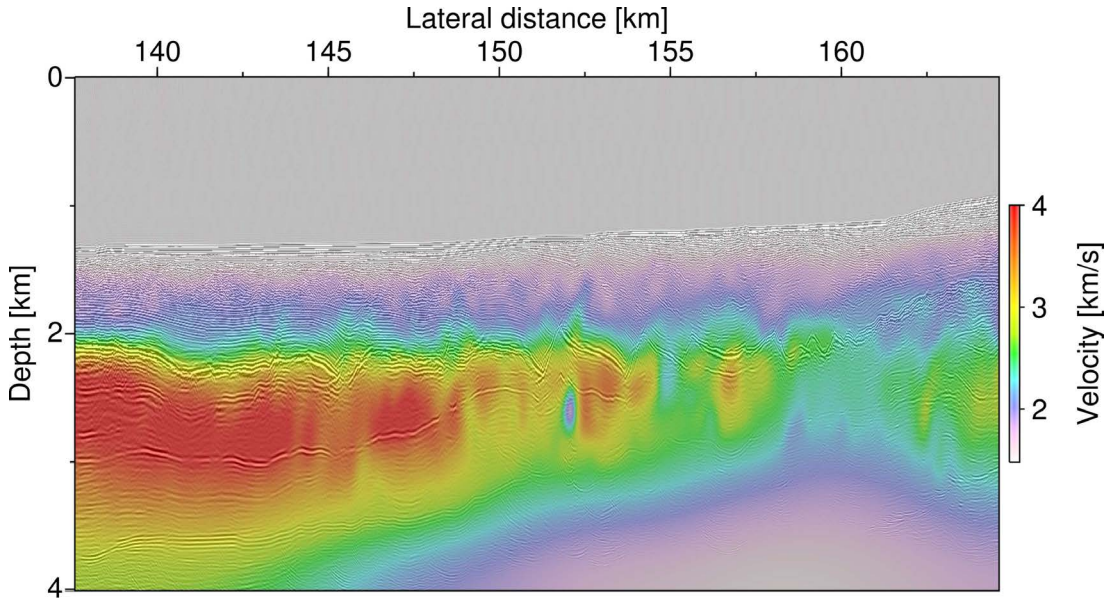

Figure 3.8: *Reverse-time depth-migrated image of the marine field data overlain with the final velocity model obtained from joint inversion of reflections and diffractions.*

order to be able to automatically pick low-amplitude events in the data, we carried out a zero-offset diffraction separation, which is based on the assumption that the second-order attributes M_{NIP} and M_N coincide in the case of a diffraction. Their similarity is evaluated at each zero-offset sample by a weight function (Dell and Gajewski, 2011) of the form

$$w(x_0, t_0) = \exp\left(-\frac{|M_N - M_{NIP}|}{|M_N + M_{NIP}|}\right), \tag{3.13}$$

which reaches its maximum 1 if $M_{NIP} = M_N$. In this case, we defined a threshold of $w = 0.9$ and only stacked the events with a larger value of w, while the remaining events were neglected. The resulting diffraction-only stack is displayed in Figure 3.5b. The result reveals numerous low-amplitude events, which are masked by reflections in the full zero-offset stack.

For the automatic picking of events, we propose the following strategy: first, picking of high-amplitude events in the full zero-offset semblance section. Afterwards, picking of low-amplitude events in the diffraction-only semblance section using a lower semblance threshold. Note that this picking process is fully automatic and only relies on the semblance and the stack section, which both offer the advantage of an increased signal-to-noise ratio. In order to get rid of data points corresponding to multiple reflections, we plotted the two-way time t_0 of all picks against the corresponding M_{NIP} and sorted out all data points not following the general trend. Thus, we obtained a total number of 11955 data points, of which 6430 were extracted from the full semblance section and 5525 from the diffraction-only data. Finally, we carried out a joint tomographic inversion using all picked data points together as input. Figure 3.6a shows all data points in the full zero-offset semblance section.

For the inversion, we used a grid of 136×41 B-spline knots with a spacing of 200 m in x and 100 m in z-direction. We assumed to have no a priori information of the velocity in the subsurface. Accordingly, the initial model solely consisted of the near-surface velocity v_0 =

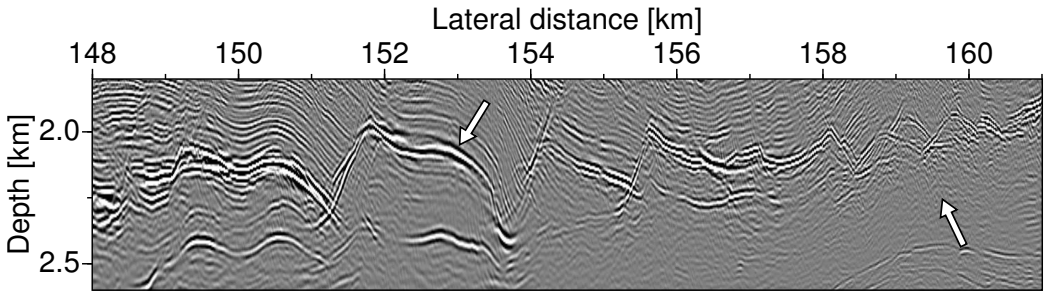

RTM: reflection-only inversion

(a)

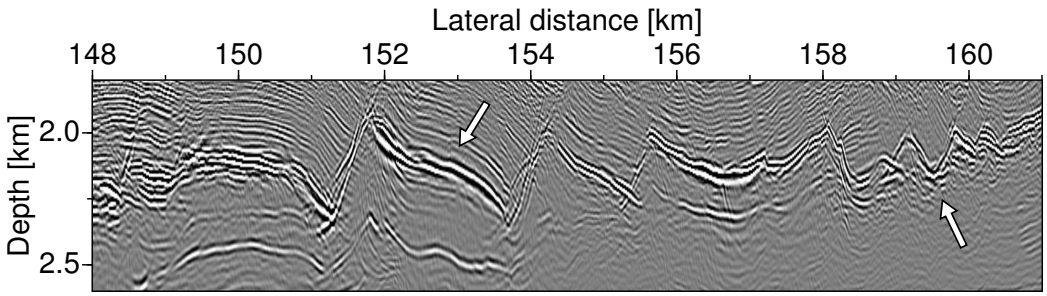

RTM: joint inversion

(b)

Figure 3.9: *Excerpts of the reverse-time-migrated images obtained with (a) the reflection-based velocity model and (b) the velocity model from joint inversion of diffractions and reflections.*

1480 ms^{-1}. It is displayed in Figure 3.6b together with the initial ray starting locations associated to each data point. During the inversion, we constrained the velocity within the water column to v_0. The inverted model is displayed in Figure 3.6c overlain with the final ray starting locations associated to each data point. Figure 3.7b shows a clean version of the model obtained by joint inversion of diffractions and reflections, whereas Figure 3.7a shows a velocity model resulting from an inversion of the high-amplitude reflections only (6430 data points). Both results were obtained after 6 inversion runs each, during which the regularization weights ϵ_{xx} and ϵ_{zz} were systematically decreased in order to increase the model resolution. Whereas the first inversion run was started with the initial model displayed in Figure 3.6b, the subsequent runs were started with the final result of the respective previous run. The total number of iterations was 227 (joint inversion) and 239 (reflection-only inversion). The final model of the joint inversion (Figure 3.7b) reveals a high-velocity zone, which is more prominent to the left of the profile. This is in agreement with the salt geometry known to be present in the region (see also Hübscher and Netzeband, 2007; Dümmong et al., 2008). Compared to the results of previous studies (Meier, 2007; Dümmong et al., 2008), our result confirms the general velocity distribution. A comparison of the velocity models obtained by joint inversion (Figure 3.7b) and reflection-only inversion (Figure 3.7a) reveals that the incorporation of low-amplitude diffractions enhances the resolution of the velocity model and even reveals new features, particularly on the right side of the profile.

In order to examine the validity of the velocity model from joint inversion (Figure 3.7b), we

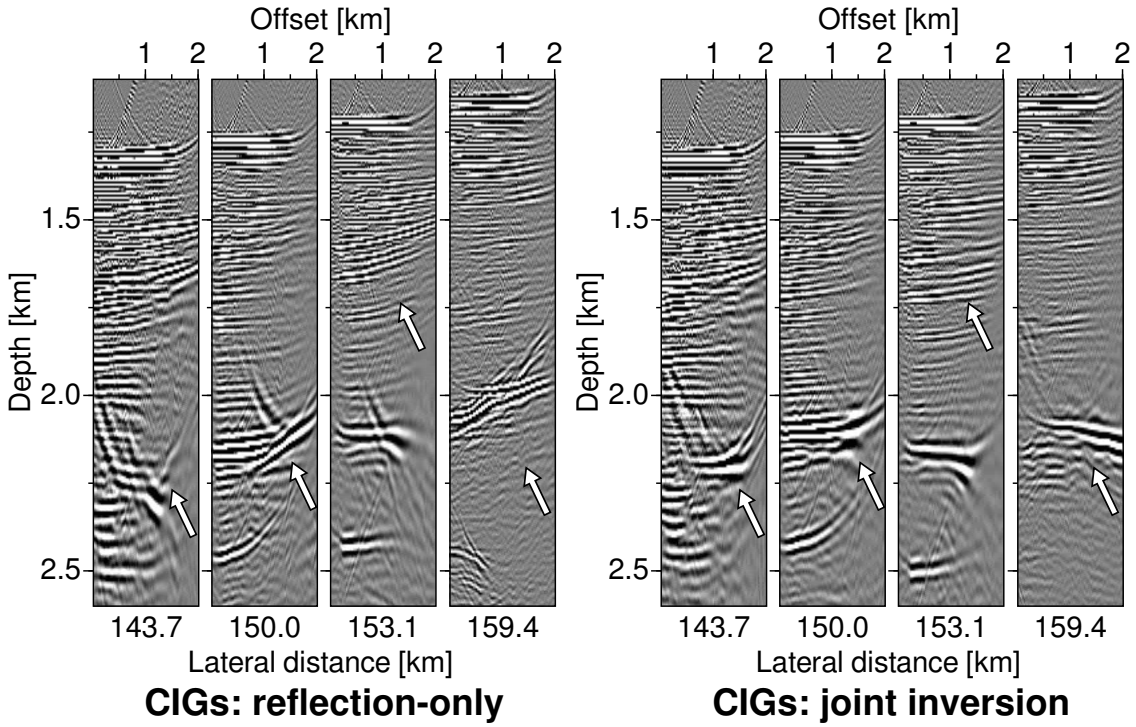

Figure 3.10: *Common-image gathers (CIGs) of reverse-time-migrated data obtained with (a) the reflection-based velocity model and (b) the velocity model from joint inversion of diffractions and reflections for four different midpoint locations with a maximum offset of 2 km each.*

used it as input for a reverse-time migration (RTM) algorithm (e.g., Baysal et al., 1983; Schuster, 2002). The used RTM implementation is based on a deconvolution imaging condition in the time domain (Valenciano and Biondi, 2002). The result is displayed in Figure 3.8 overlain with the velocity model. It shows that the salt-roller structures could be imaged clearly along the whole profile, even at the steep flanks. Also the reflections from the bottom of the salt are clearly visible. The general velocity structure is in good agreement with the salt geometry imaged by the RTM. For comparison we applied the RTM algorithm again using the reflection-based velocity model (Figure 3.7a). Figure 3.9 shows excerpts of the migrated images using the reflection-only velocity model (Figure 3.9a) and the velocity model based on joint inversion (Figure 3.9b) in order to compare the prominent salt-roller structures in the dataset. The salt geometry appears better resolved along the whole profile in the RTM image based on the joint inversion and particularly the rugged structures on the right side of the profile, indicated by strong diffractions in the CRS stacks (see Figure 3.5), are imaged more clearly and with larger amplitudes. For further examination of the quality of the migration results, Figure 3.10 shows common-image gathers (CIGs) taken from four different lateral positions along the profile with a maximum offset of 2 km each. The CIGs taken from the RTM results based on the joint inversion (Figure 3.10b) generally appear flatter than the ones taken from the reflection-based RTM result (Figure 3.10a), indicating a better quality of the depth migration. Particularly large differences are visible for the top-of-salt events at about 2.2 km depth, which confirms the previously made observation that

taking diffractions into account during velocity inversion not only improves the resolution of the velocity model, but also enhances the resulting depth-migrated image.

3.7 Discussion

The results presented in this paper confirm that poststack wavefront tomography is an efficient and stable tool to obtain highly-resolved subsurface velocity models, which does not require any a priori velocity information except the usually well-known near-surface velocity. Furthermore, unlike other inversion techniques such as prestack stereotomography (Billette and Lambaré, 1998) or full-waveform inversion (Virieux and Operto, 2009), CRS-based wavefront tomography does not interact with the full prestack data volume, but relies on wavefront attributes defined in the poststack domain. These wavefront attributes can be estimated for instance by the zero-offset CRS stack or any other operator of the CRS family using local coherence analysis, which allows automatic picking of data points for the tomographic inversion. While this implies a certain robustness of the method with respect to, for instance, random noise, errors made in the coherence and attribute estimation may have significant impact on the quality of the inversion. Therefore, further improvement of the CRS stack, by utilizing global optimization strategies (e.g. Walda and Gajewski, 2015) or by incorporating more accurate moveout approximations that are better suited for diffractions (e.g. Schwarz et al., 2014b), as well as the design of more sophisticated diffraction filters is of central importance to improve the suggested approach to poststack wavefront tomography.

While previous applications were mainly based on high-amplitude reflections in the data, we propose utilizing diffractions for improving the resolution of the velocity models. As the simple synthetic examples show, diffractions can contribute to velocity inversion due to their better illumination of the subsurface. In addition, they provide a new criterion for the quality of the inversion results, because in a correct model, all contributions belonging to one diffractor should focus at the same subsurface position. While we treated each data point independently in this work, in future work we aim to incorporate the focusing criterion for diffractions as a constraint into the inversion algorithm.

On complex industrial field data, we suggest independent extraction of reflected and diffracted events from the data and a joint inversion using all data points together. In this fashion, the general velocity distribution may be steered by the high-amplitude reflections, whereas the diffracted contributions serve to enhance the resolution of the velocity model. While this higher resolution helps to improve depth-migration results, the resulting velocity models do not feature a resolution comparable to results of methods like full-waveform inversion, but they may serve as high-quality starting models for these sophisticated inversion techniques improving cycle-skip issues.

Since diffractions, in contrast to reflections, from a kinematic point of view are a one-way process, their moveout can be described entirely in the zero-offset section (Schwarz et al., 2014a; Bauer et al., 2016a), which supports the nature of our zero-offset-based approach. Wavefront tomography is also applicable for joint localization and velocity inversion in a passive seismic setting. First promising results have been published recently by Schwarz et al. (2016b).

3.8 Conclusions

In this paper, we revisited the largely automatic process of wavefront tomography as an efficient tool to infer the seismic velocity structure of the subsurface, which does not require a priori velocity information. With special emphasis on non-Snell scattering, we illustrated by means of simple synthetic examples that the use of diffracted contributions can enhance the resolution of the inverted models. On industrial field data, the joint inversion of reflected and diffracted contributions led to a reliable detection of the salt and to an increased resolution of the velocity model compared to the conventional result gained by favoring reflections. Results of reverse-time migration based on the improved velocity model revealed a better imaging of the complex salt geometry in the depth domain, which is confirmed by flatter common-image gathers.

Acknowledgments

The contributions of Ekkehart Teßmer in the RTM processing are highly appreciated. We thank Manuel Lotze and Tobias Werner for their valuable contributions in the course of this project and Jan Walda for the generation of wavefront attributes for the field data. This work was kindly supported by the sponsors of the *Wave Inversion Technology (WIT) Consortium*, Hamburg, Germany, and is part of the project *Imaging steep structures with diffractions* funded by the German Federal Ministry of Economic Affairs and Energy (BMWi 0325363C). We thank the Applied Seismics Group at the University of Hamburg for continuous discussion and TGS for providing the marine field data. Seismic Unix was used for data processing, for creating the simple synthetic datasets and for the generation of figures. We would also like to thank the editor-in-chief Mauricio Sacchi, the associate editor Tristan van Leeuwen and the anonymous reviewers for their valuable comments during the revision process.

4 Unsupervised event identification and tagging for diffraction focusing

Abstract

Multi-parameter stacking schemes like the common-reflection-surface (CRS) stack have shown to yield reliable results even for strongly noise-contaminated data. This is particularly useful for low-amplitude events such as diffractions, but also in passive seismic settings. As a by-product to a zero-offset section with a significantly improved signal-to-noise ratio, the CRS stack also extracts a set of physically meaningful wavefront attributes from the seismic data, which are a powerful tool for further data analysis. These wavefront attributes describe the properties of two conceptual wavefronts emerging at the surface. Whereas these wavefronts are hypothetical in the reflection case, for diffractions and passive seismic events the wavefront attributes describe the actually measured wavefront. Although the attributes are extracted locally from the raw data and vary laterally along the events, an analysis of their local similarity allows the global identification of measurements, which stem from the same diffractor or passive source, that is, from the same location in the subsurface. In this work, we present a fully unsupervised scheme to globally identify and tag diffractions in simple and complex data by means of local attribute similarity. Due to the fact that wave propagation is a smooth process and due to the assumption of only local attribute similarity, this approach is not restricted to settings with moderate subsurface heterogeneity. We demonstrate by means of a simple example that event tagging is an essential ingredient for, for example, focusing analysis in wavefront tomography and for uncertainty analysis of velocity and localization for diffraction-only data. Although not explicitly shown in this work, the proposed method is equally applicable to passive seismic data.

4.1 Introduction

In recent years, the process of seismic diffraction has gained increasing research interest in hydrocarbon exploration, because it is known to be caused by small subsurface heterogeneities often related to complicated geology (e.g. Landa and Keydar, 1998). In that context, the successful focusing of recorded diffractions bears the potential for very localized, highly resolved imaging of discontinuous changes in elastic properties of the subsurface that naturally complements more conventional laterally smooth reflection images (Khaidukov et al., 2004). As one of the first objectives, seismic diffractions have been successfully used to identify and image faults, which are often poorly resolved (Krey, 1952). In addition to increased resolution, the successful incorporation of diffracted arrivals in velocity model building schemes has recently suggested that another major benefit of these weak signatures is improved lateral illumination of subsurface structures, which makes them particularly useful in reduced cost-effective acquisitions (Fomel et al., 2007; Santos et al., 2012; Bauer et al., 2017b).

Despite all the aforementioned principal advantages of diffracted wavefields, they still remain largely unexplored in common processing workflows. Aside from the overall weakness of these signals' amplitudes, the main reason for this systematic neglection arguably arises from the fact that they strongly interfere with other more prominent wavefield contributions, in particular reflections (e.g. Kozlov et al., 2004). Because of that, in recent years, a variety of methods has been suggested to robustly separate the weak diffraction background. However, as many of these approaches depend on the a priori knowledge of a depth-velocity model, they can only indirectly contribute to velocity model building (e.g. Moser and Howard, 2008; Klokov and Fomel, 2012; Dafni and Symes, 2017) and diffraction separation remains a direction of active research. Together with different variations of plane-wave destruction filters (Fomel, 2002), noticeable advances have been made in utilizing collective event properties, linked to characteristics of the emerging wavefronts, for diffraction identification, extraction, and imaging. Building on the assumption of local coherence, multi-parameter stacking schemes such as the common-reflection-surface (CRS) stack (Jäger et al., 2001) not only provide an improved data volume with a significantly increased signal-to-noise ratio, but also extract a set of physically meaningful wavefront attributes from the data. These wavefront attributes (Hubral, 1983) can be used for numerous subsequent processing steps, such as time migration (e.g. Mann, 2002; Bóna, 2011), prestack data enhancement (Baykulov and Gajewski, 2009), prestack diffraction enhancement (Bauer et al., 2016a), diffraction separation (Dell and Gajewski, 2011; Schwarz and Gajewski, 2017a; Bakhtiari Rad et al., 2018) and velocity model building for reflection (Duveneck, 2004b) and diffraction (Bauer et al., 2017b), as well as passive seismic data (Schwarz et al., 2016b; Diekmann et al., 2018b).

Also, it has been suggested that from a wavefront perspective, diffractions behave kinematically exactly like passive sources excited at the diffracting structure in depth, which makes most of the aforementioned processing schemes likewise naturally applicable to diffracted and passive events (Schwarz et al., 2016b, 2017a; Diekmann et al., 2018b). Consequently, all of these applications would benefit from the a priori knowledge, which wavefront measurements share the same origin in depth. While this discrimination can be easily made with the human eye by optically tracking the diffracted or passive event, an algorithm requires objective criteria for the identification and discrimination of contributions stemming from different subsurface regions. Following the mentality of image segmentation, which is routinely employed in image processing workflows, in this work, we propose a fully unsupervised scheme, which utilizes the local similarity of wavefront attributes for the global identification and tagging of diffractions directly in the data domain. Since wave propagation is a smooth process, the assumption of local similarity of wavefront attributes is reasonable and not restricted to settings with moderate subsurface heterogeneity.

In the following section, we introduce the theory of wavefront attributes, whose understanding is fundamental for the proposed method. We outline various applications of them, which partly are a requirement for event tagging. After that, we introduce the event tagging scheme in theory and by means of a simple synthetic example. We then confirm the stability of the proposed method by means of simple synthetic 2D and 3D diffraction examples and an application to complex 2D marine field data. Further, we suggest a range of applications – including the formulation of focusing constraints in wavefront tomography or the assessment of event-consistent location and velocity inversion uncertainties – directly following or benefiting from the suggested automated classification strategy.

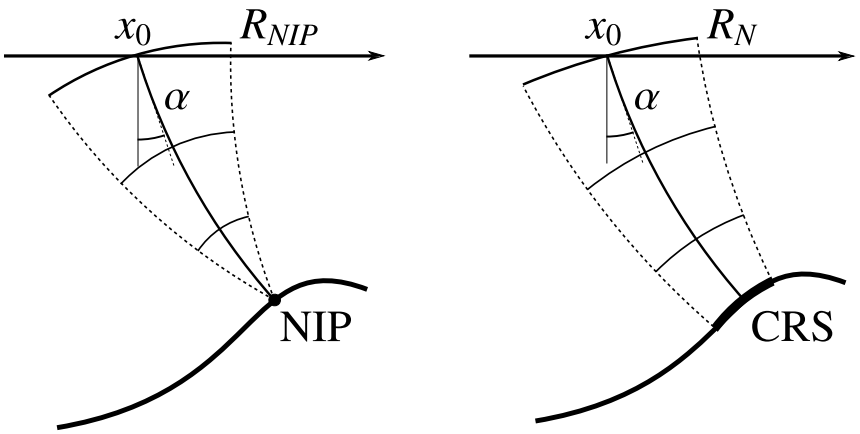

Figure 4.1: *The 2D wavefront attributes α, R_{NIP} and R_N. In the reflection case, the NIP wave (left) is excited by a point source placed on the reflector's point of normal incidence (NIP) and the normal wave (right) is excited by an exploding reflector segment (CRS) around the NIP. In the case of a diffraction or a passive seismic event, they coincide and describe the actually measured wavefront.*

4.2 Wavefront attributes

Wavefront attributes (Hubral, 1983) are physically meaningful parameters, which are encoded in the moveout of seismic events. They describe the direction and the radii of two conceptual waves emerging at the recording surface at the angle α. While the normal-incidence-point (NIP) wave is excited by a hypothetical point source placed on the reflector's point of normal incidence, the normal (N) wave is excited by a hypothetical exploding reflector segment around the NIP. In the case of a point diffraction or a passive event, the two waves coincide. In addition, the NIP wave is no longer hypothetical as it describes the wavefront that actually emerges at the recording surface. In Figure 4.1, the meaning of the three 2D wavefront attributes is illustrated. In 3D, the concept of the two waves is the same, but the number of parameters increases to eight.

4.2.1 Common-reflection surface

The wavefront attributes can be extracted from the raw data by the application of multi-parameter stacking methods such as the common-reflection surface (CRS) stack (Jäger et al., 2001) using local (Mann, 2002) or global (Walda and Gajewski, 2017) optimization methods. In 2D, the hyperbolic CRS stacking operator reads

$$t^2(t_0, x_0) = (t_0 + 2p\Delta x)^2 + 2t_0(M_{NIP}h^2 + M_N\Delta x^2)\,, \tag{4.1}$$

where the midpoint displacement $\Delta x = x - x_0$ is the distance from the central midpoint x_0 and h the half-offset. The first derivative of the traveltime moveout is the horizontal slowness, which can be related to the emergence angle α of the locally measured wavefront,

$$p = \frac{\sin\alpha}{v_0}\,, \tag{4.2}$$

where v_0 is the near-surface velocity. The second derivatives of the traveltime moveout with respect to half-offset and midpoint displacement, respectively, contain the wavefront curvatures

R_{NIP} and R_N of the two previously mentioned hypothetical waves (Hubral, 1983):

$$M_{NIP} = \frac{\cos^2 \alpha}{v_0 R_{NIP}}\,, \qquad M_N = \frac{\cos^2 \alpha}{v_0 R_N}\,. \tag{4.3}$$

In addition to CRS, numerous other multi-parameter traveltime formulations exist, which are either hyperbolic (Jäger et al., 2001) or non-hyperbolic (Gelchinsky et al., 1999; Fomel and Kazinnik, 2013; Schwarz et al., 2014b). However, all of them may be parametrized in terms of the previously introduced wavefront attributes. Further, recent studies for heterogeneous subsurface settings have shown that wavefront attributes of good quality can be obtained with either of them (Schwarz and Gajewski, 2017c,b; Walda et al., 2017).

In practice, the wavefront attributes are extracted from the data in an automatic fashion by searching the set of attributes (α, R_{NIP}, R_N) at a point in the data, which yields the largest local semblance coefficient for a subset of traces located in a pre-defined aperture extending in midpoint and half-offset direction around a central point (t_0, x_0). This optimization problem can be solved either by three one-dimensional line searches and a subsequent local optimization (Mann, 2002) or by a global optimization with a simultaneous search for all three attributes (Walda and Gajewski, 2017).

In the 3D case, the hyperbolic CRS traveltime moveout is given by (e.g. Müller, 2009)

$$t^2(t_0, \mathbf{m}_0) = \left(t_0 + 2\mathbf{p}\Delta\mathbf{m}\right)^2 + 2t_0(\mathbf{h}^T\mathbf{M}\mathbf{h} + \Delta\mathbf{m}^T\mathbf{N}\Delta\mathbf{m})\,, \tag{4.4}$$

where the vectors $\Delta\mathbf{m} = \mathbf{m} - \mathbf{m}_0$ and $\mathbf{h}$ denote the midpoint displacement and half-offset, respectively. The slowness vector $\mathbf{p}$ contains the two angles, which define the emergence direction of the previously introduced conceptual wavefronts, the NIP wave and the normal wave, which are described by the symmetric 2×2 matrices $\mathbf{M}$ and $\mathbf{N}$. Accordingly, in the 3D case eight wavefront attributes have to be extracted from the data. In the diffraction case, this number reduces to five, because $\mathbf{M}$ and $\mathbf{N}$ coincide.

4.2.2 Applications of wavefront attributes

Since the wavefront attributes estimated during the CRS stack have a physical meaning, they can be exploited for numerous subsequent applications, some of which we will briefly introduce in the following. All of these applications are directly connected to the event-tagging scheme suggested in this work. While the application of diffraction filters for active seismic data is a prerequisite for the event tagging, methods like prestack data enhancement, time migration and wavefront tomography can benefit from the previous identification and tagging of measurements with common origin in depth.

Diffraction separation

Diffractions are often hidden or masked by reflections, which usually have larger amplitudes. However, as they are caused by small subsurface heterogeneities, they often contain structurally relevant information, which is necessary to obtain detailed images of the subsurface. Therefore, the separation of diffractions is an important application. For that, we can make use of the fact that in the case of a diffraction, the two wavefront curvatures R_{NIP} and R_N coincide. Dell and Gajewski (2011) introduced the threshold function

$$w_R(t_0, x_0) = \exp\left(-\frac{|R_N - R_{NIP}|}{|R_N + R_{NIP}|}\right)\,, \tag{4.5}$$

which takes the value one if $R_{NIP} = R_N$ and is smaller if they differ. Thus, by defining a threshold close to one and only stacking those events, for which the threshold is exceeded, it is possible to obtain a stacked section that predominantly contains diffracted energy.

A different approach for the separation of diffractions was recently introduced by Schwarz and Gajewski (2017a). It is designed for low-fold or single-channel data, as often acquired in academic environments, where the wavefront curvatures cannot be estimated accurately because of the missing offsets. Therefore, the separation of reflections and diffractions requires a different filter function in this case. Schwarz and Gajewski (2017a) suggest to generate reflection-only data, which can then be subtracted adaptively from the original data in order to generate diffraction-only data. They use a filter function

$$F_p(|p|) = 1 - \Theta(|p| - |p_0|)\,, \tag{4.6}$$

where Θ is the Heaviside step function. Here, p_0 represents a user-defined threshold, which can be chosen relatively small for moderate reflector dips. In contrast to the second-order diffraction filter (4.5), the function F_p becomes one for reflections and can thus be used to generate reflection-only data $\mathcal{R}$. The reflection-only data $\mathcal{R}$ can then be subtracted adaptively from the input data $\mathcal{I}$, resulting in diffraction-only data $\mathcal{D}$ (Schwarz and Gajewski, 2017a),

$$\mathcal{D}(t_0, x_0) = \mathcal{I}(t_0, x_0) - \gamma\mathcal{R}(t_0 + \tau, x_0)\,, \tag{4.7}$$

where γ is a local scaling coefficient and τ a time correction. These quantities are the result of an optimization problem, which has to be solved for every data point (t_0, x_0).

Prestack data enhancement

The zero-offset wavefront attributes may also be used for prestack data enhancement without explicitly performing computationally expensive finite-offset stacks (Baykulov and Gajewski, 2009; Schwarz et al., 2015; Bauer et al., 2016a). In the partial CRS stack (Baykulov and Gajewski, 2009), the reference traveltime t_0 is extrapolated to finite offset and the zero-offset wavefront attributes are used to perform local finite-offset stacks in the prestack data without any further optimization. For moderate heterogeneity and small stacking apertures this method can provide regularized prestack data with a significantly increased signal-to-noise ratio, which is particularly helpful in the case of low-fold land data with irregular acquisition and strong noise. Schwarz et al. (2015) extended this method by extrapolating not only t_0, but also the slopes to finite-offset. They use the first-order finite-offset traveltime operator (Zhang et al., 2001) for a local refinement of the extrapolated slopes and perform local finite-offset stacks with the obtained attributes.

Time migration

Time migration is a widely-used method for obtaining a first structural image of the subsurface. While depth migration, which is the final step of seismic imaging, is very sensitive to errors in the velocity model, time migration is far less sensitive to velocity errors. Mann (2002) introduced a way to estimate the apex location of a diffractor in time based on the zero-offset wavefront attributes. The apex coordinates can be obtained in the zero-offset plane ($h = 0$) by setting the derivative of the traveltime moveout of a diffraction (equation (4.1) with $M_N = M_{NIP}$) with

respect to the midpoint direction to zero,

$$t_{apex}^2(t_0, x_0) = \frac{t_0^3 v_0 \cos^2 \alpha}{2R_{NIP} \sin^2 \alpha + t_0 v_0 \cos^2 \alpha}, \tag{4.8}$$

$$x_{apex}(t_0, x_0) = x_0 - \frac{R_{NIP} t_0 v_0 \sin \alpha}{2R_{NIP} \sin^2 \alpha + t_0 v_0 \cos^2 \alpha}, \tag{4.9}$$

$$v_{RMS}^2(t_0, x_0) = \frac{2v_0^2 R_{NIP}}{2R_{NIP} \sin^2 \alpha + t_0 v_0 \cos^2 \alpha}, \tag{4.10}$$

where (t_{apex}, x_{apex}) are the estimated apex coordinates for the considered event at (t_0, x_0) and v_{RMS} the corresponding dip-corrected effective velocity. The apex coordinates are constant along an event in the case of no lateral heterogeneity. Still, also in a heterogeneous subsurface they should not vary much along a diffraction and thus are a helpful tool for the global identification of events.

4.3 Event tagging

Although the zero-offset wavefront attributes obtained during the application of the CRS stack are local quantities, they provide us with valuable information about the measured events that can be exploited for the automatic global identification and tagging of events with a common origin in depth. Since wave propagation is a smooth process, it is reasonable to assume the local similarity of wavefront attributes, that is, that wavefront attributes do not change abruptly along an event. Due to this assumption of only local similarity, the global identification of events is not limited to data acquired in subsurface settings with a small degree of heterogeneity. Accordingly, the goal of our method is an automatic analysis of the diffractions in a given set of zero-offset wavefront attributes resulting in the assignment of a numeric tag to each unique event. The method consists of two main steps, which we will outline in the following with the help of a simple synthetic diffraction data example.

4.3.1 Detection of events

Figure 4.2 shows zero-offset sections for a simple synthetic 2D diffraction dataset, which contains three diffractions and is based on a velocity model containing both vertical and lateral heterogeneity. In the upper two rows of Figure 4.2, the results from the CRS stack are displayed: the zero-offset stack (Figure 4.2a), the corresponding coherence (Figure 4.2b) and the wavefront attributes α (Figure 4.2c) and R_{NIP} (Figure 4.2d). The bottom line of Figure 4.2 shows the apex coordinates t_{apex} (Figure 4.2e) and x_{apex} (Figure 4.2f) calculated from the wavefront attributes via equations (4.8) and (4.9), respectively. As expected, although α and R_{NIP} vary strongly along the diffractions, they are locally smooth and do not experience abrupt changes. Therefore, the assumption of local similarity is valid and we can utilize it for the global identification of events. The apex coordinates remain almost constant along the events and thus are a suitable additional criterion for the identification of events. We suggest to use the semblance and all four attributes for the matching of events in order to better constrain the problem.

The first step of the event tagging consists in the automatic detection of "valid" events, which is carried out trace-wise. For this purpose, we define a window τ_{max} around a given central

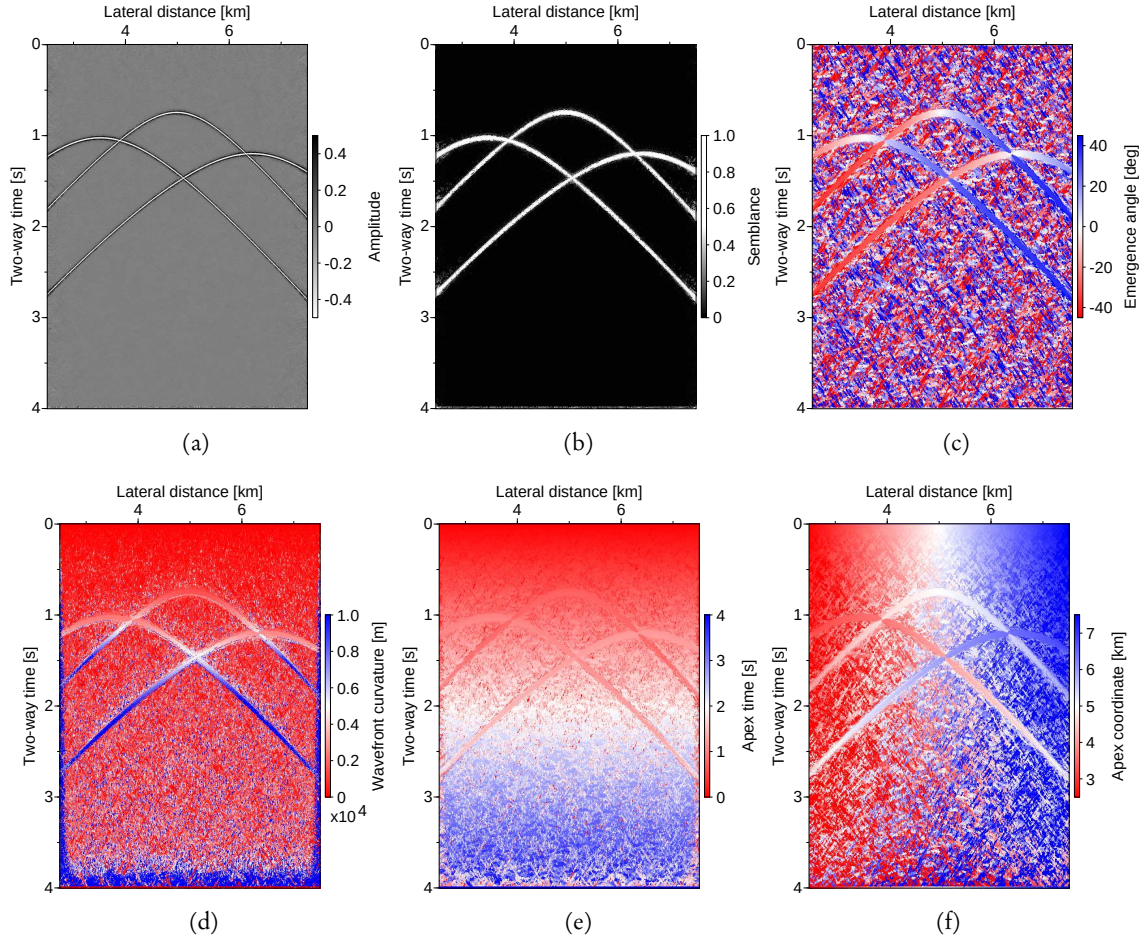

Figure 4.2: *Zero-offset sections for simple synthetic diffraction data with three events. The first line shows (a) the zero-offset CRS stack and (b) the corresponding semblance. The second line shows the wavefront attributes (c) α and (d) R_{NIP} estimated during the CRS stack. The apex coordinates (e) t_{apex} and (f) x_{apex} are calculated from the wavefront attributes.*

sample t_0, such that the time range $t_0 \pm \tau_{max}$ is considered. The value for τ_{max} should be chosen such that the total length of the window is smaller than the width of the events in the coherence section. The given sample t_0 is only considered if its coherence exceeds a pre-defined threshold. If this is the case, we evaluate the local similarity of the wavefront attributes by calculating their semblance coefficients (Neidell and Taner, 1971) given by

$$S_\phi(t_0, x_0) = \frac{1}{n} \frac{\left(\sum_{\tau=t_0-\tau_{max}}^{t_0+\tau_{max}} \phi(\tau, x_0)\right)^2}{\sum_{\tau=t_0-\tau_{max}}^{t_0+\tau_{max}} \phi(\tau, x_0)^2}, \tag{4.11}$$

where ϕ is the corresponding wavefront attribute (α, R_{NIP}, x_{apex} or t_{apex}), x_0 the midpoint under consideration and n the number of samples in the window. In the case of a valid event, which usually ranges over various samples, the local similarities S_ϕ of the attributes should be close to 1 at the event's central sample. If the local similarities of all attributes exceed the corresponding pre-defined thresholds, which should be chosen close to 1, an event tag is assigned to the sample

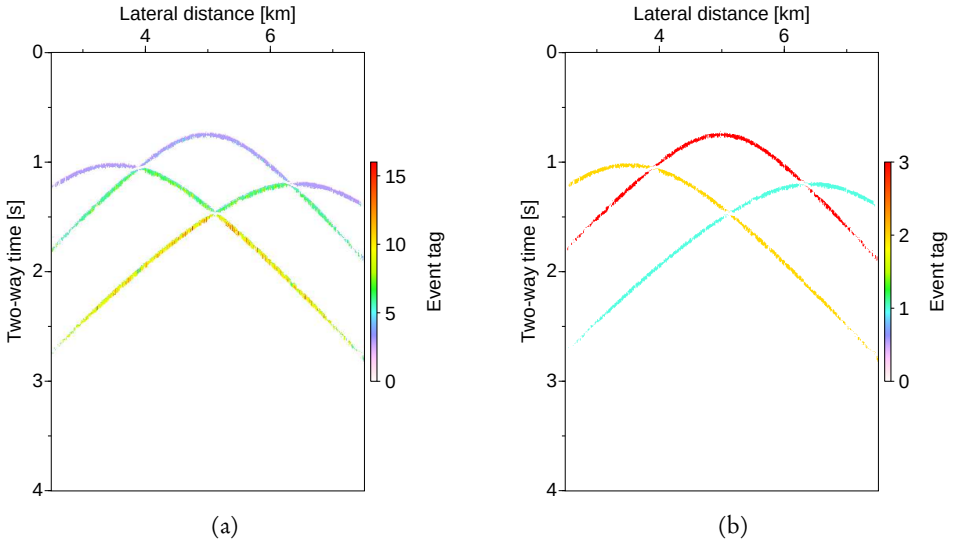

Figure 4.3: *Event tags for the simple synthetic diffraction data: (a) the trace-wise detected events and (b) the final event tags after the lateral matching of the detected events.*

t_0 under consideration. If an event tag exists within the window $t_0 - \tau_{max}$, the corresponding attribute values are compared directly by calculating

$$S_\phi^{match} = \frac{1}{2} \frac{(\phi(t_0, x_0) + \phi(t_0 - \tau, x_0))^2}{\phi(t_0, x_0)^2 + \phi(t_0 - \tau, x_0)^2}, \tag{4.12}$$

where $\phi(t_0, x_0)$ is the wavefront attribute at the current sample t_0 and $\phi(t_0 - \tau, x_0)$ the one at the sample $t_0 - \tau$ within the window $t_0 - \tau_{max}$, which also contains an event tag. If S_ϕ^{match} is close to 1 for all attributes, the samples t_0 and $t_0 - \tau$ are assumed to belong to the same event and the tag from the sample $t_0 - \tau$ is copied to the sample t_0. Otherwise, a new tag is assigned to the event detected on the sample t_0. This procedure is repeated for all samples on the trace and for all traces in the zero-offset volumes. After detecting the events on all traces, we calculate the similarity of the assigned tags S_{tags} via equation (4.11), which will be needed for the lateral matching of events. The result of this first step for the simple synthetic diffraction data is displayed in Figure 4.3a. It shows that the three diffractions could be detected trace-wise throughout the whole section. As a next step, these detected events have to be matched laterally. During this step, detected events with only few occurrences, that is, outliers, will be sorted out.

4.3.2 Lateral matching of events

The next step after the trace-wise identification of events is the lateral matching of those measurements, which belong to the same diffraction. For that, we define two windows: a window Δx_{max} in midpoint direction, which defines the maximum number of neighboring traces to be searched, and a window τ_{max} in sample direction, which defines the range of time samples to be examined. The search is started at a given sample t_0 on a midpoint trace x_0, which contains a previously identified event, that is, S_{tags} is close to 1, and coincides with a local coherence maximum, that is, the coherence at (t_0, x_0) is larger than at the surrounding samples. If this *seed event* at (t_0, x_0)

has been matched in a previous search, we will only search for matching events to the right using the already assigned tag. Otherwise, we will first search for matching events to the left. During both searches, we vertically shift the search window depending on the local moveout Δt in the zero-offset section ($h = 0$), which we calculate via

$$\Delta t(t_0, x_0) = \sqrt{(t_0 + p\Delta x)^2 + M_{NIP}\Delta x^2} - t_0 \,, \tag{4.13}$$

where the midpoint displacement Δx is the distance $|\Delta x| \leq \Delta x_{max}$ from the central trace x_0. If (t_0, x_0) has not been assigned an event tag yet, we first step trace by trace to the left ($\Delta x < 0$) while vertically shifting the search window τ_{max} depending on the event's moveout for the given lateral distance. For each previously matched event contained in the search space, we compare its wavefront attributes to the ones of the seed event at (t_0, x_0) by calculating

$$S_\phi^{match} = \frac{1}{2}\frac{(\phi(t_0, x_0) + \phi(t_0 + \Delta t + \tau, x_0 + \Delta x))^2}{\phi(t_0, x_0)^2 + \phi(t_0 + \Delta t + \tau, x_0 + \Delta x)^2} \,, \tag{4.14}$$

where $\phi(t_0, x_0)$ is a wavefront attribute of the current event and $\phi(t_0+\Delta t+\tau, x_0+\Delta x)$ a wavefront attribute on the trace $x_0+\Delta x$ at the sample $t_0+\Delta t+\tau$ within the moveout-shifted vertical window $(t_0 + \Delta t) \pm \tau_{max}$. If S_ϕ^{match} exceeds the pre-defined thresholds for all attributes, the measurements at (t_0, x_0) and $(t_0 + \Delta t + \tau, x_0 + \Delta x)$ are assumed to belong to the same event. If various matching events are found during the search to the left, the one with the highest matching coefficients S_ϕ^{match} is chosen and the event tag is copied from the corresponding location $(t_0 + \Delta t + \tau, x_0 + \Delta x)$ to (t_0, x_0). If there are no traces to the left or the target regions of the neighboring traces do not contain previously matched events, a new event tag is assigned to the current sample (t_0, x_0).

As a next step, the traces to the right ($\Delta x > 0$) of the seed event at (t_0, x_0) are searched for matching events. For each event identified during step 1 within the moveout-adapted search space to the right, the wavefront attributes of the seed event at (t_0, x_0) are compared to the ones at the corresponding location $(t_0 + \Delta t + \tau, x_0 + \Delta x)$. If S_ϕ^{match} exceeds the thresholds for all attributes, the current event tag is copied from (t_0, x_0) to $(t_0 + \Delta t + \tau, x_0 + \Delta x)$.

After searching all traces of the zero-offset sections for matching events, we obtain a section with a unique tag assigned to each diffraction or passive event. Events occurring on very few traces are considered outliers and sorted out. The result for the simple synthetic diffraction data is displayed in Figure 4.3b. As desired, all three diffractions could be identified globally by assigning them a unique tag. Note that this result was obtained in a fully unsupervised fashion. Applications of the event tagging algorithm to synthetic diffraction data with more events and to field data are presented in Section 4.4 of this paper.

4.3.3 Event tagging in 3D

The current implementation of the event-tagging algorithm in 3D is based on the 2D implementation. However, in the current version, absolute attribute differences instead of the semblance coefficient are used for the analysis of attribute similarity. Since seismic diffractions are intrinsically 3D phenomena, the step from 2D to 3D is a natural one. While the larger number of wavefront attributes in 3D is an advantage because the discrimination of different events is better constrained, on the other hand wavefront attributes are more difficult to obtain in a stable fashion in 3D due to the same reason. We present first promising results of an application of the 3D event-tagging algorithm to synthetic diffraction data in Section 4.4.

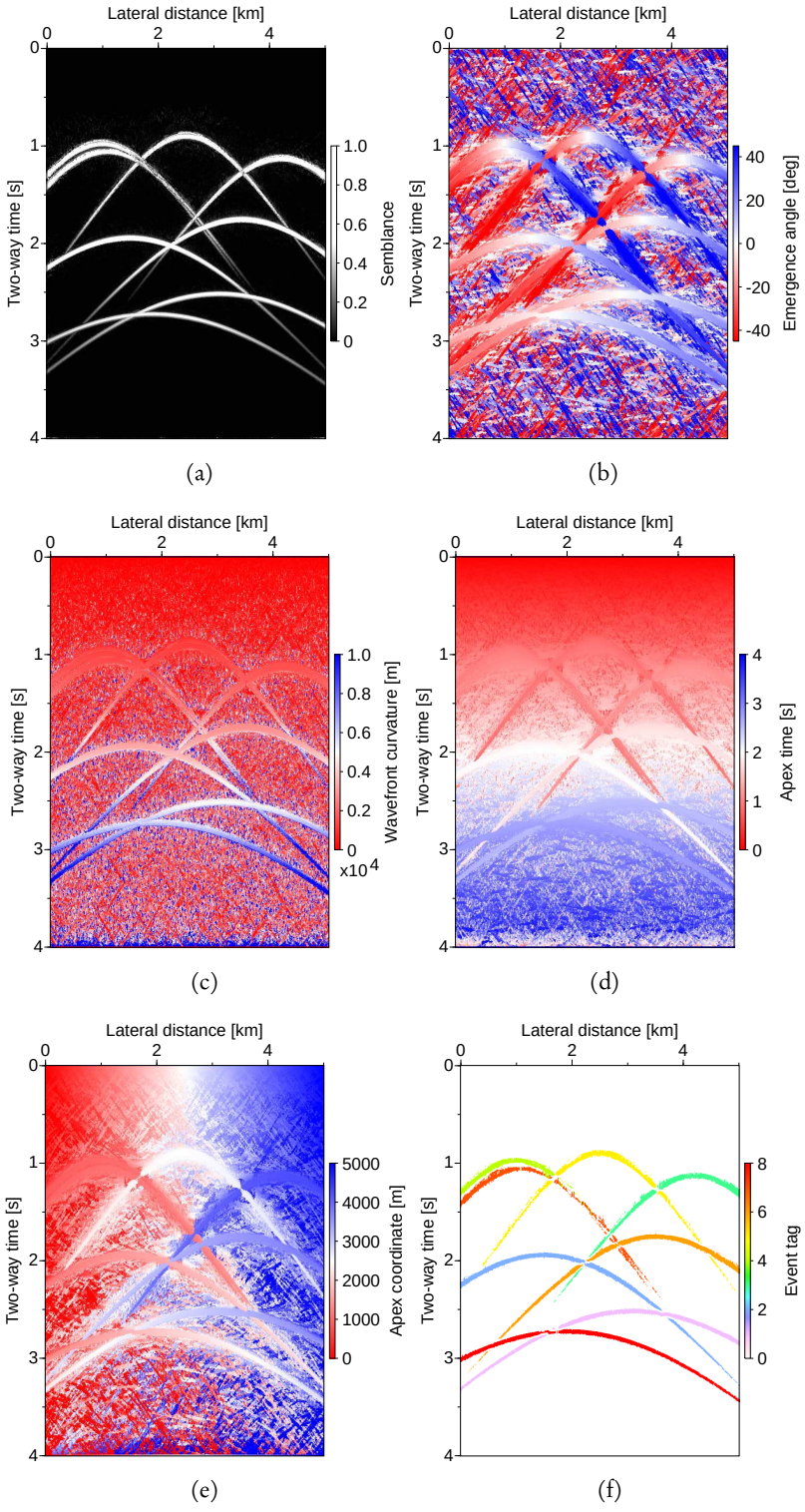

Figure 4.4: *Results for 2D synthetic diffraction data with eight events: (a) the zero-offset coherence, the wavefront attributes (b) α and (c) R_{NIP}, the apex coordinates (d) t_{apex} and (e) x_{apex} and (f) the resulting event tags.*

4.4 Examples

In this section we present applications of the introduced event-tagging algorithm to synthetic 2D and 3D diffraction data as well as complex 2D marine field data.

4.4.1 2D synthetic diffraction data

The results of the application of the 2D event-tagging algorithm to synthetic diffraction data containing eight diffractions are presented in Figure 4.4. The diffraction-only dataset is based on a vertically inhomogeneous velocity model with a velocity gradient of $0.5\,s^{-1}$. Figure 4.4a shows the zero-offset coherence and Figures 4.4b and 4.4c the wavefront attributes α and R_{NIP}, respectively, as resulting from the application of the CRS stack. The apex coordinates calculated via equations (4.8) and (4.9) are displayed in Figures 4.4d and 4.4e. All wavefront attributes reveal the expected smooth behaviour, which permits the assumption of their local similarity. The result of the application of the introduced event tagging algorithm to the shown zero-offset sections is presented in Figure 4.4f. All eight diffractions contained in the data could be discriminated and were assigned with a unique event tag. Difficulties merely occurred on the tails of the two diffractions in the upper left of the section. These two diffractions lie so close together that a discrimination is hardly possible, because the wavefront attributes are practically the same, particularly on the tails. Since this also means that the two diffractions stem from almost the same subsurface region, this is not a critical problem, though.

4.4.2 3D synthetic diffraction data

Figure 4.5 presents the results of the application of the 3D event-tagging algorithm to synthetic 3D diffraction data. The dataset contains five diffractions and is also based on a vertically inhomogeneous velocity model. While Figures 4.5a and 4.5b show the full zero-offset coherence volume and an inner excerpt of it, Figures 4.5c and 4.5d present the resulting event tags. Although some problems occurred at the apices of the diffractions, all five events could be tagged correctly. Since the number of wavefront attributes is larger in 3D, the discrimination of diffractions is even better constrained than in 2D. In contrast to the presented 2D results, for the generation of these results absolute attribute differences instead of the semblance coefficient were used. Further, the apex coordinates have not yet been incorporated into the 3D implementation.

4.4.3 2D field data

In Figure 4.6, the results of an application of the proposed 2D event-tagging algorithm to complex 2D marine field data are presented. The dataset was acquired by TGS in the Eastern Mediterranean offshore Israel. It is characterized by pronounced salt-roller structures (Netzeband et al., 2006), which cause a lot of diffracted energy (Bauer et al., 2017b). The wavefront attributes for these results were obtained with a CRS implementation using global optimization and accounting for conflicting dips (Walda and Gajewski, 2017). Before the application of the event tagging algorithm, a poststack diffraction separation (Dell and Gajewski, 2011) was applied to the CRS results. The full resulting zero-offset diffraction coherence section is shown in Figure 4.6a, while Figure 4.6c presents a close-up taken from the far right part of the profile. The corresponding event tags are plotted in Figure 4.6b as an overlay over the entire coherence and in Figure 4.6d for the close-up. The results reveal that a large number of diffractions among the whole profile could

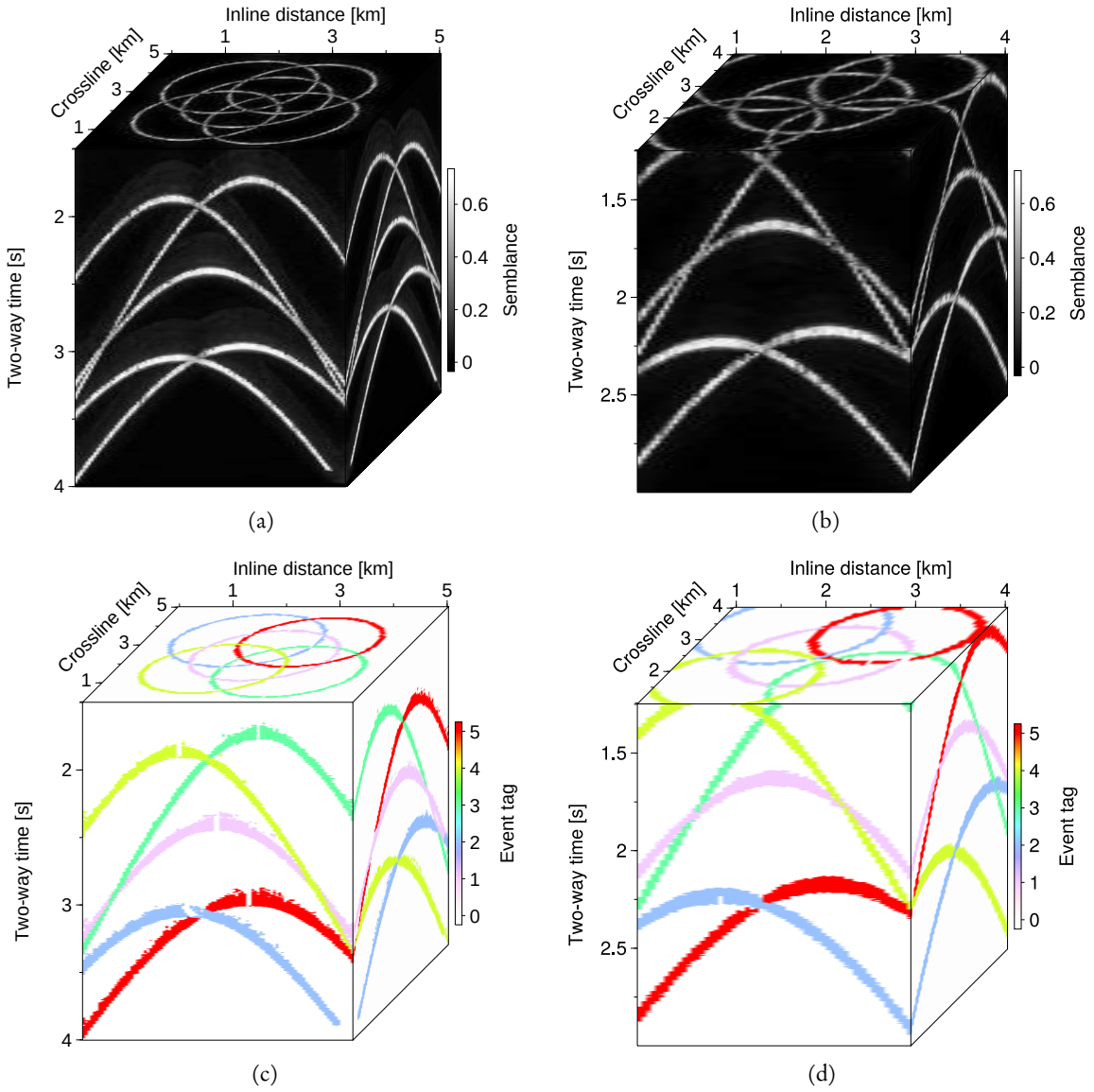

Figure 4.5: *Results for 3D synthetic diffraction data with five events: (a) the zero-offset coherence cube, (b) an inner excerpt of the coherence cube, (c) the resulting event tag cube and (d) an excerpt of the event tag cube.*

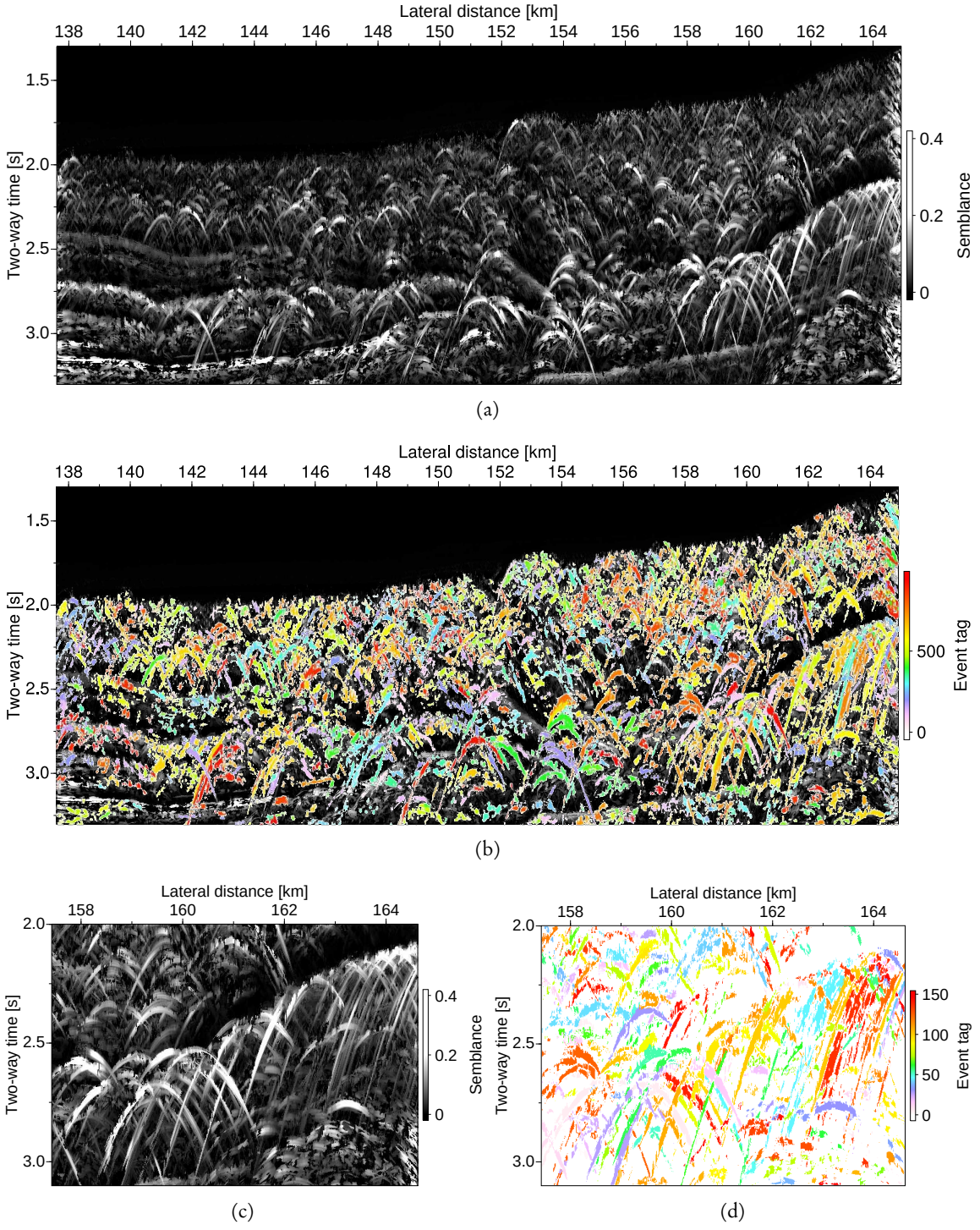

Figure 4.6: *Results for the marine field data: (a) the zero-offset coherence after diffraction separation, (b) the coherence section overlain with resulting event tags, (c) an excerpt from the far right part of the coherence section, (d) the event tags for the same excerpt.*

be identified and tagged correctly. Problems only occurred in regions, where diffraction apices lie very close together resulting in very similar wavefront attributes. Please note that this result was obtained in a completely unsupervised fashion without any manual quality control involved. As an interesting by-product, the event tagging algorithm also provides a total event count.

4.4.4 Potential applications

As previously outlined, various subsequent processing steps may benefit from the identification and tagging of diffractions, three of which we will outline in the following.

Diffraction decomposition

In the case of diffractions, that is, non-Snell scattering, one can make use of the fact that up- and downgoing waves are decoupled and therefore, the moveout of a diffraction can be described entirely in the zero-offset setting (Bauer et al., 2016a). This means that any finite-offset stacking operator can be composed out of two zero-offset operators extracted at the source and receiver locations corresponding to the desired offset,

$$t_{FO}(x_s^0, x_g^0, t_0^{FO}, \alpha_s, \alpha_g, R_s, R_g) = \frac{t_{ZO}(x_s^0, t_0^{ZO,s}, \alpha_0^s, R_{NIP}^s)}{2} + \frac{t_{ZO}(x_g^0, t_0^{ZO,g}, \alpha_0^g, R_{NIP}^g)}{2}, \tag{4.15}$$

where t_{FO} is the finite-offset operator for the half-offset $(x_g^0 - x_s^0)/2$ composed out of two independent zero-offset diffraction operators measured at x_s^0 and x_g^0, respectively. The finite-offset wavefront attributes coincide with their zero-offset counterparts from the corresponding source and receiver locations and the finite-offset reference traveltime t_0^{FO} is given by $(t_0^{ZO,s} + t_0^{ZO,g})/2$. Unlike the extrapolation method mentioned in section 4.2.2, the diffraction traveltime decomposition is exact, as recently shown in theory and proven in synthetic and field data applications by Bauer et al. (2015a, 2016a). Since it depends on the unique properties of diffractions, this method is not applicable to reflection data. Event tagging is an essential ingredient for the application of diffraction decomposition, because the information, which zero-offset measurements belong to the same event, is needed in order to find the two zero-offset operators in equation (4.15). If the information is available, the contributions do not have to be searched for in the data by coherence analysis, which significantly speeds up the application.

Wavefront tomography

Wavefront tomography (Duveneck, 2004b) is an efficient and stable seismic inversion scheme, which uses zero-offset wavefront attributes for velocity model building in the depth domain. Initially, wavefront tomography was mainly applied using attributes measured for reflections (Duveneck, 2004b; Dümmong et al., 2008). Bauer et al. (2017b) recently showed that diffractions can help to improve the resolution of the velocity models obtained with wavefront tomography and that their unique properties may contribute not only to further constrain the inversion, but also to estimate uncertainties (Bauer et al., 2017a). Further, Schwarz et al. (2016b) have shown that wavefront tomography may likewise be used for passive-seismic source localization.

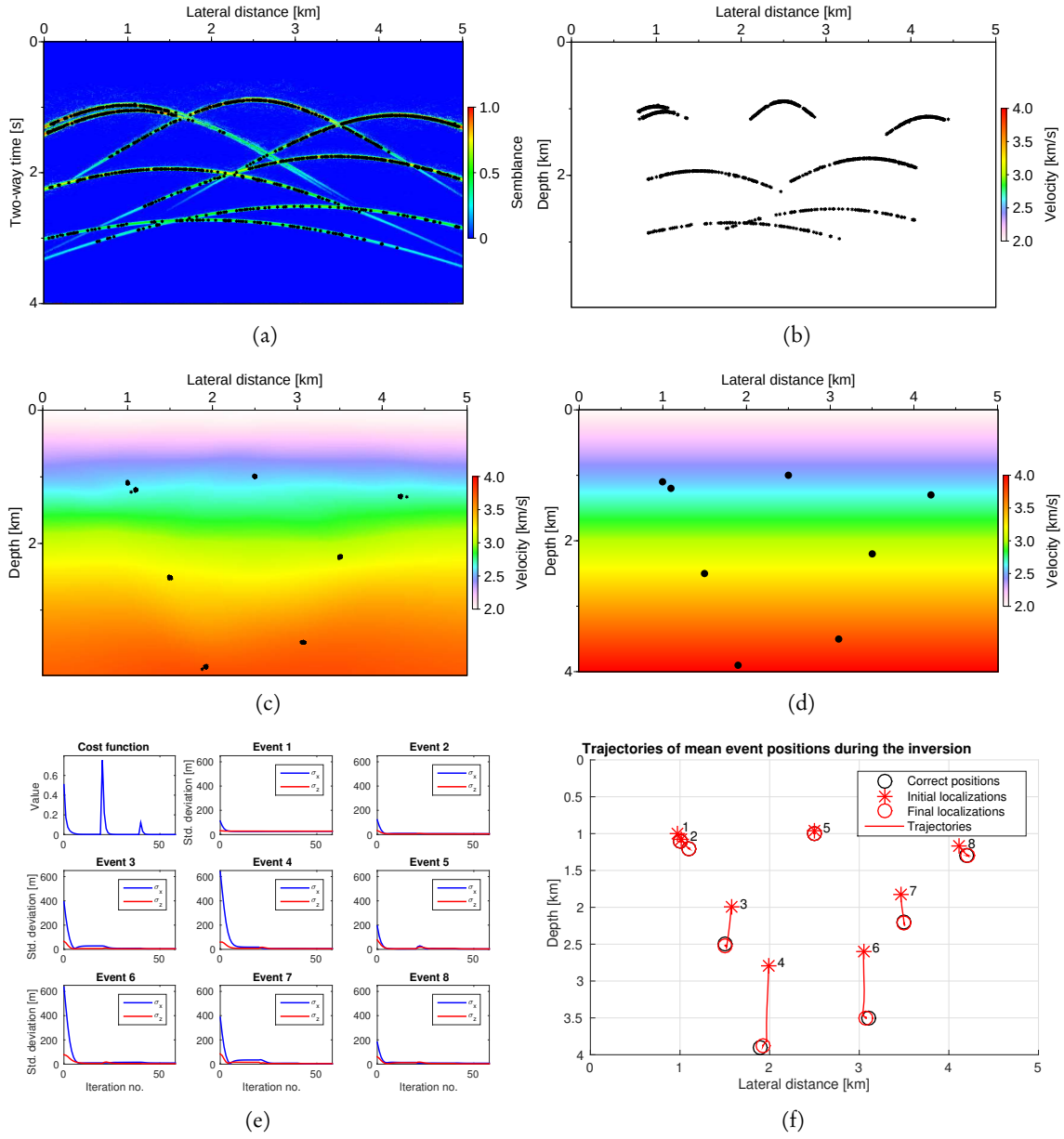

Figure 4.7: *Application of wavefront tomography to 2D synthetic diffraction data: The picked data points (a) are the input for the inversion, (b) the constant initial model, (c) the inverted model with the final localizations of all data points and (d) the correct model with the correct diffractor positions. (e) shows the cost function and the standard deviations σ_x and σ_z of all locations belonging to the same event. The peaks in the cost function correspond to refinements of the B-spline-knot grid. In (f), the trajectories of the mean event locations during the inversion are depicted. The red stars indicate the mean initial locations, the red circles the mean final locations and the red lines the corresponding trajectories during the inversion. The black circles are the correct locations of the diffractors.*

Wavefront tomography is an efficient method because it does not require any interaction with the prestack data. The data points, which form the input for the inversion, can be picked in a completely automatic fashion in the attribute volumes estimated by the zero-offset CRS stack based on their local coherence (Bauer et al., 2017b). Each data point consists of the set of zero-offset attributes

$$\mathbf{d}_i = (x_0, T, p, M_{NIP})_i, \qquad i = 1, \ldots, n_{picks}\,, \tag{4.16}$$

where $T = t_0/2$ is the one-way zero-offset traveltime. The velocity model $v(\xi, \zeta)$ is described by B-splines, whose user-defined knot locations are given by a $n_\xi \times n_\zeta$ grid. During the inversion, kinematic ray tracing into the subsurface is performed for all data points starting from d_i to obtain initial subsurface locations (NIPs) $(\xi, \zeta, \theta)_i$, where θ is the angle at which the ray arrives at (ξ, ζ). Subsequently, dynamic ray tracing in the upward direction starting from $(\xi, \zeta, \theta)_i$ yields modeled data points $\tilde{\mathbf{d}}_i = (\tilde{x}_0, \tilde{T}, \tilde{p}, \tilde{M}_{NIP})_i$. The least-squares misfit between measured and modeled data is used as the objective function for the inversion, which is given by

$$\Psi(\mathbf{m}) = \frac{1}{2}\|\mathbf{d} - \tilde{\mathbf{d}}\|_2^2 + \Lambda\left(\partial_{\xi\xi} v(\xi, \zeta)), \partial_{\zeta\zeta} v(\xi, \zeta)\right)\,, \tag{4.17}$$

where $\mathbf{m}$ is the model vector that contains the B-spline coefficients v_i and the subsurface locations $(\xi, \zeta, \theta)_i$ related to the data points. The additional regularization term Λ ensures a smooth velocity model by minimizing the second derivatives of $v(\xi, \zeta)$. In our implementation, the velocity model is updated iteratively by minimizing the misfit function $\Psi(\mathbf{m})$ using a least-squares algorithm (Paige and Saunders, 1982). A working implementation of wavefront tomography in 3D is also available (Duveneck, 2004a).

In the context of wavefront tomography, the event tags pave the way for an assessment of the obtained velocity models via the quantification of localization uncertainties in depth. Also, contributions which belong to the same diffraction may be forced to focus in depth by introducing a constraint into the inversion. As an example, Figure 4.7 shows the results of an application of wavefront tomography to the 2D synthetic diffraction data introduced in Section 4.4.1. Figure 4.7a shows the data points, which form the input for the inversion and were picked in an automatic fashion based on their coherence. The initial model (Figure 4.7b) merely consists of the constant near-surface velocity used for the estimation of wavefront attributes. Black asterisks indicate the initial ray starting locations for all data points, which are obtained by kinematic ray tracing. The final model (Figure 4.7c) was obtained after a total of 61 iterations. During the inversion, the initial 6×5-grid of B-spline knots with a knot spacing of 1000 m in both x and z-directions was refined twice by halving the knot spacing, such that the final 21×17 grid has a knot spacing of 250 m in both directions. The result shows that the final ray starting locations (black asterisks) focused at eight distinct locations, although they were treated independently in this application, that is, no focusing constraint has been included into the inversion. A comparison to the true model with the correct positions of the eight diffractors (Figure 4.7d) directly reveals that both velocity and localizations could be retrieved successfully by the inversion algorithm.

In this application, the event tags were used to calculate the mean positions and standard deviations of the depth locations connected to all data points with the same event tag during the inversion. Figure 4.7e shows the horizontal and vertical standard deviations σ_x and σ_z for each of the eight events along with the cost function (4.17). The peaks in the cost function correspond to the two refinements of the B-spline grid. As expected, the standard deviations of all events decrease in a similar fashion as the cost function and converge to very small values, indicating a good localization quality. In Figure 4.7f, the trajectories of the mean event positions

during the inversion are plotted. The stars indicate the mean positions in the initial model, the lines correspond to the trajectories of the mean positions during the inversion and the red circles are the mean positions in the final model. The black circles denote the correct positions of the diffractors, which are almost congruent with the final localizations for all eight events.

Passive-source data

Diffractions are focusing wavefields and kinematically, from a wavefront perspective, behave exactly like passive-source wavefields excited at the diffractor location. The previously described process of wavefront tomography back-projects emerging wavefronts, characterized through local coherence measurements, into the subsurface, which lets one arrive at an estimate of both, the focusing location, and the traversed velocity structure. Thus, it is likewise naturally applicable to passive-seismic data (Schwarz et al., 2016b; Diekmann et al., 2018b). While in controlled-source acquisitions, the zero-offset response directly reveals (twice) the reference propagation time t_0, in the passive case this quantity needs to be estimated additionally due to the fact that the excitation time t_s is generally not known. For the general 3D case we have

$$[t_{data} + t(t_0, \mathbf{m}_0) - t_0]^2 = (t_0 + \mathbf{p}\,\Delta\mathbf{m})^2 + t_0\,\Delta\mathbf{m}^T\mathbf{N}\,\Delta\mathbf{m}\,, \tag{4.18}$$

where $t_{data} = t_s + t_0$ is the reference recording time and t_0, here, represents the one-way rather than the two-way propagation time at the reference receiver location $\mathbf{m}_0$. In correspondence with the general 3D paraxial two-way traveltime operator (4.4), $\Delta\mathbf{m}$ denotes the lateral receiver separation of every considered trace, and the quantities $\mathbf{p}$ and $\mathbf{N}$ represent the two-component slope vector and the 2×2 curvature matrix, respectively. As equation (4.18) suggests, the propagation time t_0 and the time coordinate of the considered data point, in contrast to the controlled-source case, generally differ, thereby demanding the estimation of an additional unknown from the data. Please note, however, that the source excitation time t_s, which can directly be derived from the given recording time t_{data} and the estimated t_0, represents a natural global event attribute that can also be used for event discrimination (Schwarz et al., 2016b; Diekmann et al., 2018b). In the common-source or the common-receiver gather, diffractors appear exactly like passive sources and the time of diffraction is generally not known and needs to be estimated (e.g. Schwarz and Gajewski, 2017b). Similar to the example presented in the previous subsection, the application of wavefront tomography to passive seismic data benefits directly from the event-tagging scheme (Diekmann et al., 2018b).

4.5 Discussion

A main prerequisite for the suggested event-tagging scheme is the sufficiently dense sampling of the recorded wavefields. While user-defined constraints can help to guide the coherence analysis in cases of moderate sparsity, too large trace separations are likely to result in spatial aliasing which makes conventional coherence analysis suffer or even fail. However, this limitation is intrinsic and well-acknowledged in the general context of migration. Therefore, it is by no means exclusive to the presented method. In addition, owing to the symmetry of diffractions in different data configurations, dense trace spacing – at least in one of these domains – can be safely assumed in most realistic circumstances. If diffracted wavefields are numerous and strongly interfere with each other – an observation that can often be made, for example, in crystalline rock

environments – large portions of an event might be hidden behind other, more prominent contributions, resulting in the so-called *conflicting-dip problem*, which represents a notorious challenge in multi-dimensional stacking (e.g. Walda and Gajewski, 2017). Schwarz and Gajewski (2017a) presented a simple yet powerful solution to this problem, in that the less prominent interfering wavefields can be accessed by adaptively subtracting the amplitude-strong contributions that are normally favored. Although only reflections were targeted, the same methodology can also be applied to adaptively separate one diffraction from another. As is the case with other methods, the estimation of local attribute similarity can be flawed if different diffractions are largely tangential, that is, of similar shape and location, in data space. While the formulation of more discriminative attribute representations and similarity measures can, to a certain extent, help to improve selectivity in these situations, natural limitations are reached when differences in onset and overall shape approach the order of the predominant signal's period. However, it may be argued that in this case, the two events from a wavefront perspective are largely equivalent and likely have originated in a similar subsurface region.

Building on the potential for full automation in coherence analysis and multi-dimensional stacking, the presented strategy links individual measurements of one particular diffracted event without supervision by evaluating the local similarity of a set of wavefront attribute representations. While the presented attributes turned out to already work reasonably well, they should merely be viewed as exemplary measures for discrimination. In general, the algorithm, depending on the wavefield complexity encountered in the preceding coherence analysis stage, couples to the data through these wavefront characteristics and other, more elaborate versions might be considered in the future. The unsupervised grouping or tracking of individual contributions of a dataset is well-known in other fields. In image processing, a variety of sophisticated techniques exist to perform the segmentation of an image, for example, based on color. As the color-coded images of the presented event attributes suggest, the detection of their local similarity can be fully transformed to an image processing objective, which lets a vast ecosystem of commercial or open-source segmentation routines be readily exploitable for the discrimination of individual diffracted events. In addition, concepts from machine learning, that is, more sophisticated types of pattern recognition, should prove useful in further improving the presented results. Despite these strong and fruitful interfaces, however, it needs to be appreciated that the extracted attributes represent physically meaningful characteristics of the emerging diffracted wavefronts, which helps to naturally constrain and guide existing techniques. As illustrated with different concrete examples, we are convinced that the global identification and tagging of individual diffracted contributions bears the potential to significantly improve existing applications, including but certainly not limited to velocity model building. We have demonstrated with a simple example that the detection of a joint origin in depth directly helps to constrain wavefront-tomographic inversion potentially leading to improved estimates of the scatterer location and the principal assessment of event-consistent uncertainties. Although not explicitly presented here, it appears natural to assume that in the same fashion, full-waveform-based as well as migration techniques are expected to equally benefit from these constraints. Note that the presented method does not intrinsically assume a type of event and thus, in principle, is applicable to any type of event. While an application to reflections is not worthwhile in the context of focusing in the subsurface, since every reflected contribution in a zero-offset section originates at a different subsurface location, in the case of edge or line diffractions it makes sense to tag their diffractive parts, which also belong to the same subsurface point. However, the reflective parts, whose directional behavior honors Snell's law, may be neglected.

4.6 Conclusions

We have introduced a fully unsupervised scheme for the global identification and tagging of diffractions, which stem from the same subsurface region. The proposed method works entirely in the data domain and only relies on the assumption of local similarity of wavefront attributes estimated during the common-reflection-surface (CRS) stack. Since wave propagation is a smoothing process, this assumption does not restrict the suggested approach to moderately heterogeneous subsurface settings. Applications to synthetic 2D and 3D diffraction data have confirmed that diffractions can be identified and tagged correctly. An application to complex marine field data further revealed the potential and stability of the method in complex settings. Future work may include the integration of sophisticated image-segmentation algorithms as well as machine-learning techniques into the suggested scheme. As illustrated by means of a synthetic diffraction example, the gained knowledge may be exploited to further constrain diffraction wavefront tomography by focusing common contributions in depth and to assess uncertainties in the obtained velocity models. Also, other processing steps such as time migration and prestack diffraction enhancement may benefit from the proposed event tagging scheme. In addition, the suggested scheme is likewise applicable to passive seismic data.

Acknowledgments

We thank Leon Diekmann for fruitful discussions and Jan Walda for the generation of wavefront attributes for the marine field data. This work was kindly supported by the Federal Ministry for Economic Affairs and Energy of Germany (BMWi, 03SX427B) and by the sponsors of the Wave Inversion Technology (WIT) consortium, Hamburg, Germany. Benjamin Schwarz is supported by a research fellowship of the German Research Foundation (DFG, SCHW 1870/1-1). We thank the Applied Seismics Group at the University of Hamburg for continuous discussion and TGS for providing the marine field data. We thank Andrej Bóna, one anonymous reviewer and the Associate Editor Jean Virieux for their helpful comments during the revision process.

5 Diffraction wavefront tomography

Abstract

Wavefront tomography is an efficient and stable tool for the generation of smooth velocity models. As input it requires first and second-order attributes, which describe slope and curvature of the measured wavefronts. These wavefront attributes can be extracted from the data by multi-parameter stacking schemes such as the common-reflection-surface (CRS) stack. While the slopes are stable and relatively easy to determine, the wavefront curvatures can become unreliable in the case of sparsely-sampled data or strong lateral heterogeneity. Since wavefront tomography is mainly driven by the misfit of modeled and measured wavefront curvatures, curvatures of bad quality may compromise its convergence. A possible solution to overcome this problem are diffractions, which have a unique property that can be exploited for better constraining the inversion: all measurements belonging to the same diffracted event are connected to the same subsurface structure, although registered at different positions on the recording surface. In recent work, we introduced an event-tagging scheme that automatically assigns a unique tag to each diffraction in the data. We propose to use this information to constrain the inversion by enforcing all diffracted measurements with the same tag to focus in depth, thus overcoming the sole dependency of wavefront tomography on second-order attributes. Results for diffraction-only data with vertical and lateral heterogeneity confirm that it is possible to obtain depth velocity models for zero-offset data without using curvature information and that the suggested approach may help to increase the stability of wavefront tomography in complex settings.

5.1 Introduction

While traditional seismic imaging has often been designed to favor reflections, the true potential of the weak diffracted wavefield has rarely been recognized (Krey, 1952). In the last two decades, however, diffractions have gained importance and numerous applications have been proposed (e.g. Landa and Keydar, 1998; Fomel et al., 2007; Moser and Howard, 2008; Klokov and Fomel, 2012; Bauer et al., 2016a, 2017b; Schwarz, 2019). The main motivation for this change of mind is the fact that seismic diffractions occur at small-scale subsurface structures, which are often related to interesting geological features such as faults and pinch-outs and thus contain high-resolution information about the subsurface (Khaidukov et al., 2004). Since Snell's law does not hold for diffractions, any seismic diffraction can be recorded at various positions of the recording surface, which implies a better illumination of the subsurface compared to reflected waves.

In the recent years, wavefront attributes – initially being a by-product of multi-parameter stacking schemes such as the common-reflection-surface stack (CRS, Jäger et al., 2001) – have proven to be a powerful tool for seismic data analysis. While they are physical properties of hypothetical wavefronts in the reflection case, for diffractions they describe the actual wavefronts. Wavefront attributes can not only be used for imaging (e.g. Eisenberg-Klein et al., 2008; Baykulov and

Gajewski, 2009; Dell and Gajewski, 2011; Bauer et al., 2016a; Walda and Gajewski, 2017; Schwarz and Gajewski, 2017b; Schwarz, 2019), but also for velocity model building with wavefront tomography (Duveneck, 2004b). Recently, we have shown that the unique physical properties of diffractions can help to improve the resolution of depth velocity models obtained with wavefront tomography (Bauer et al., 2017b). A drawback of existing techniques for velocity-model building such as stereotomography (Billette and Lambaré, 1998), its successor adjoint slope tomography (Tavakoli F et al., 2017) or full-waveform inversion (e.g. Virieux and Operto, 2009) is that these methods require seismic data with sufficiently large offsets. However, the acquisition of seismic data with large offsets is expensive and merely feasible for the hydrocarbon industry, while academic institutions often have to cope with low-cost acquisitions and short streamers. Owing to their focusing nature, we argue that diffractions may serve as a solution to overcome this problem. However, a requirement for further benefitting from the properties of diffractions is the identification of measurements connected to the same diffraction – and thus the same subsurface structure – in the data. For this purpose, we recently proposed a scheme, which utilizes the local similarity of zero-offset wavefront attributes to globally assign tags to every diffraction in a zero-offset section (Bauer et al., 2019c). While every data point is treated independently in conventional wavefront tomography, the availability of these event tags allows for both event-consistent statistics, that is, quality control or uncertainty analysis of the obtained velocity models (Bauer et al., 2019c), and further constraining the inversion algorithm by enforcing diffraction focusing in depth.

In this work, we introduce diffraction wavefront tomography, a modified implementation of wavefront tomography, in which all diffractions with the same tag are forced to focus in depth. As a by-product, this new constraint reduces the dependency of wavefront tomography on the curvature-related second-order wavefront attributes. If curvatures are not taken into account at all, the new method evolves into a zero-offset slope tomography for diffractions. This allows its application to data, in which the determination of curvatures is challenging, such as settings with strong lateral heterogeneity or zero-offset data with few traces. Applications to synthetic diffraction data with vertical and lateral heterogeneity confirm the potential of the modified implementation, which is likewise applicable to passive seismic data (Diekmann et al., 2019a).

5.2 Wavefront attributes

The input for the inversion algorithm used in this work are the so-called zero-offset wavefront attributes (Hubral, 1983), which can be determined via multi-parameter stacking schemes such as the common-reflection-surface stack (CRS, Jäger et al., 2001). The wavefront attributes are encoded in the first and second derivatives of the traveltime moveout Δt given by

$$\Delta t^2(t_0, x_0) = (t_0 + 2p\Delta x)^2 + 2t_0(M_{NIP}h^2 + M_N\Delta x^2)\,, \tag{5.1}$$

where t_0 is the zero-offset time sample under consideration, $\Delta x = x - x_0$ is the distance from the central midpoint x_0 and h is the half-offset. The first derivative of Δt is the horizontal slowness p that can be expressed in terms of the emergence angle α of the wavefront measured at the recording surface,

$$p = \frac{\sin\alpha}{v_0}\,, \tag{5.2}$$

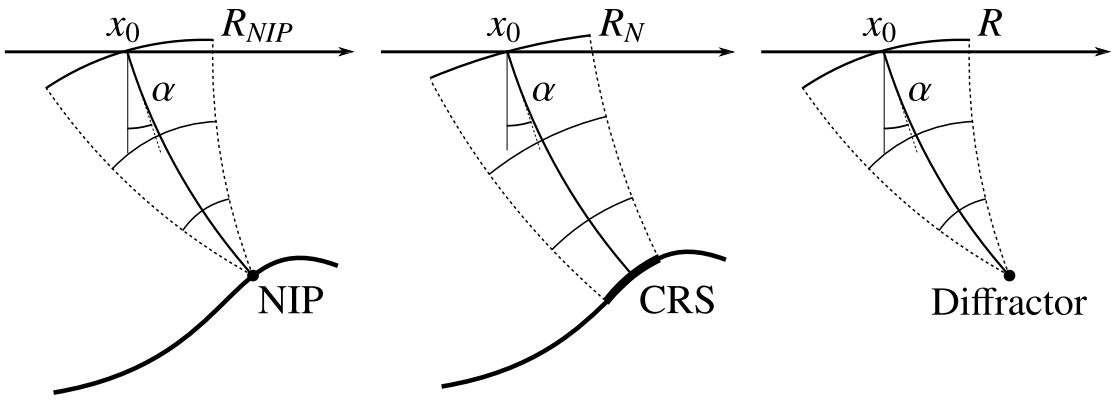

(a) Reflection case: NIP wave (b) Reflection case: normal wave (c) Diffraction case

Figure 5.1: *The 2D wavefront attributes α, R_{NIP} and R_N. In the general reflection case, the NIP wave (left) is excited by a point source placed on the reflector's point of normal incidence (NIP) and the normal wave (middle) is excited by an exploding reflector segment (CRS) around the NIP. In the case of a diffraction (right), the exploding reflector segment shrinks to a point that is the actual diffractor acting as a secondary source. As a result, R_{NIP} and R_N coincide and the NIP wave is no longer fictitious, but it describes the actual diffracted wavefront.*

where v_0 denotes the near-surface velocity. The second-order quantities M_{NIP} and M_N can be parametrized by the radii of two fictitious wavefronts, R_{NIP} and R_N,

$$M_{NIP} = \frac{\cos^2 \alpha}{v_0 R_{NIP}}, \qquad M_N = \frac{\cos^2 \alpha}{v_0 R_N}. \tag{5.3}$$

In the general case of a seismic reflection, R_{NIP} is the radius of a wavefront excited by a hypothetical point source placed on the reflector's point of normal incidence (NIP, compare Figure 5.1a) and R_N is the radius of a wavefront excited by an exploding reflector segment around the NIP (Figure 5.1b). Consequently, R_{NIP} is related to the depth of a reflector and R_N is related to its curvature. However, in the case of a diffraction, the point source is no longer hypothetical, but it is the diffractor acting as a secondary source, and the reflector segment reduces to the NIP (Figure 5.1c). Therefore, R_{NIP} and R_N coincide for diffractions and the NIP wave is the actual wavefront measured at the recording surface. Hence, in contrast to the reflection case, where offsets in the data are required for the estimation of wavefront attributes, diffraction wavefront attributes can also be determined for zero-offset data. Moreover, note that the moveout of a passive seismic event can be described by the same quantities, except for the additionally unknown source excitation time, as the moveout of an active seismic diffraction (Schwarz et al., 2016b). As a result, the inversion scheme presented in this work is equally applicable to passive seismic data (Diekmann et al., 2019a). While the first-order slopes p in general are easy to extract from the data, the determination of second-order curvatures, that is M_{NIP} and M_N, is more challenging. Particularly in complex settings with a laterally heterogeneous subsurface the successful determination of curvatures strongly depends on the chosen aperture.

The results of the CRS stack, namely a zero-offset section with improved signal-to-noise ratio, a coherence section and the wavefront attributes p and M_{NIP}, are a prerequisite for the application of wavefront tomography, which we will introduce in the following.

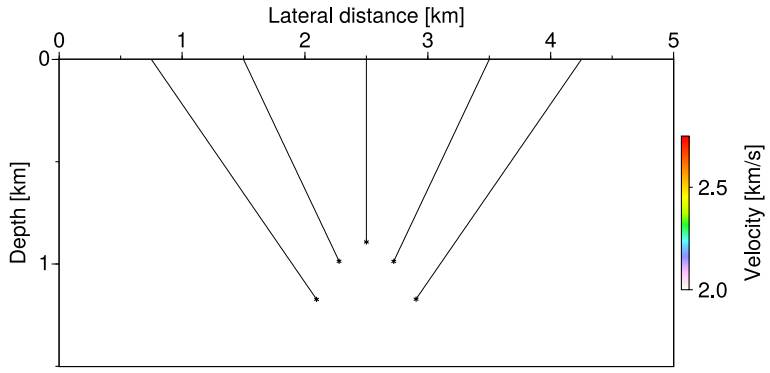

Figure 5.2: *Illustration of five initial ray paths of conventional wavefront tomography for a simple data example with one diffraction. The ray paths of the downward and upward ray tracing coincide. As a result, the initial misfit only depends on M_{NIP}.*

5.3 Wavefront tomography

Wavefront tomography is an efficient and stable method for the determination of smooth depth-velocity models. In the following, we will shortly describe conventional wavefront tomography (Duveneck, 2004b), which can be applied to both reflections and diffractions (Bauer et al., 2017b). Afterwards, we will introduce a modified implementation of wavefront tomography for diffraction-only data, in which diffractions are forced to focus in depth.

5.3.1 Conventional approach

As input for wavefront tomography, data points $\mathbf{d}_i$ have to be picked in the zero-offset sections. This can be done in an automatic fashion based on the semblance value associated to the measurements,

$$\mathbf{d}_i = (x_0, T, p, M_{NIP})_i \,, \qquad i = 1, \ldots, n_{picks} \,, \tag{5.4}$$

where x_0 is the midpoint coordinate and $T = t_0/2$ is the one-way zero-offset traveltime. The velocity model is defined in terms of 2D B-splines,

$$v(x,z) = \sum_{k=1}^{n_x} \sum_{l=1}^{n_z} v_{kl}\, \beta_k(x) \beta_l(z) \,, \tag{5.5}$$

where n_x and n_z are the number of knots in x- and z direction, respectively, and v_{kl} are the velocity values at the corresponding locations. Accordingly, the model space $\mathbf{m}$ is defined by the $n_x \times n_z$ B-spline velocity coefficients, subsurface locations $(x,z)_i$ and ray take-off angles θ_i associated to each data point. In the inversion algorithm, downward kinematic ray tracing into the given initial velocity model yields first guesses of the localizations $(x,z)_i$ of each data point. As a next step, upward dynamic ray tracing starting from $(x,z)_i$ provides the modeled data $\tilde{\mathbf{d}}$. After the initial modeling, due to the reciprocity of downward und upward ray paths, the modeled attributes $\tilde{\mathbf{d}}$ and the measured attributes $\mathbf{d}$ only differ in the values of M_{NIP}, which are calculated during the dynamic ray tracing. Figure 5.2 illustrates five ray paths of the initial modeling for a simple diffraction example. Due to the wrong initial model, the localizations $(x,z)_i$ of the five data points, which would coincide in a correct velocity model, still form a

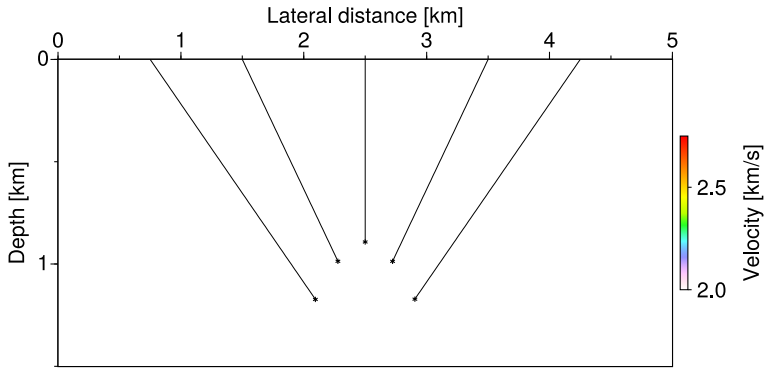

(a) Downward ray paths

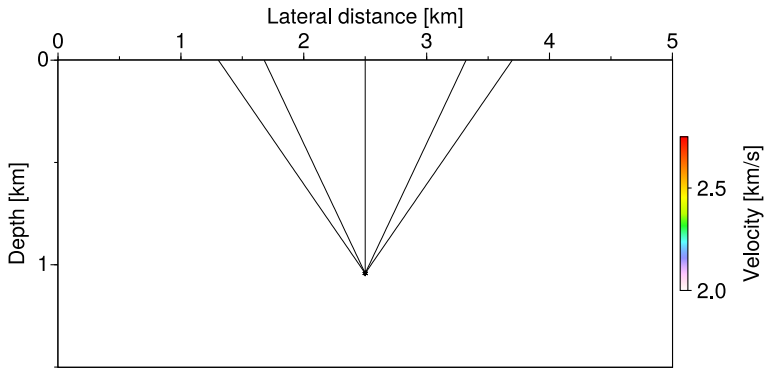

(b) Upward ray paths

FIGURE 5.3: *Illustration of five initial ray paths of diffraction wavefront tomography for a simple data example with one diffraction. The ray paths of the (a) downward and (b) upward ray tracing differ, because all localizations are set to their mean value after the downward ray tracing. As a result, the initial misfit mainly depends on x_0 and T.*

hyperbola. For the inversion scheme, the misfit between measured and modeled data $\Delta\mathbf{d} = \mathbf{d} - \tilde{\mathbf{d}}$ is defined in terms of a cost function

$$\Psi(\mathbf{m}) = \frac{1}{2}\|\mathbf{d} - \tilde{\mathbf{d}}\|_2^2 + \Lambda\left(\partial_{xx}v(x,z)), \partial_{zz}v(x,z)\right) , \tag{5.6}$$

which is minimized in a least-squares sense by an LSQR algorithm (Paige and Saunders, 1982). The second term Λ of the cost function is responsible for regularization and ensures a smooth velocity model by minimizing its second derivatives. For more details on the iterative solution of the inverse problem we refer to the original work of Duveneck (2004b). In order to account for the different units of the attributes (x_0, T, p, M_{NIP}), they are weighted with given factors (w_x, w_T, w_p, w_M) that have to be chosen by the user depending on the attribute quality and the problem at hand. However, since the initial misfit of conventional wavefront tomography only depends on the values of M_{NIP}, the weighting factor w_M must not be set to zero. Consequently, in complex settings, where the estimation of second-order attributes is challenging, this may lead to an unstable behavior of the inversion scheme.

5.3.2 Diffraction wavefront tomography

While in conventional wavefront tomography all data points are treated independently, diffractions allow the introduction of an additional constraint into the algorithm: all data points that belong to the same diffraction are connected to the same subsurface structure and therefore, all localizations connected to the same diffraction have to focus in depth. However, the implementation of this constraint requires the previous identification and tagging of diffractions, such that a unique identifier, that is, an *event tag*, is assigned to every diffraction present in the data. Bauer et al. (2019c) recently introduced a scheme that identifies and tags diffractions in an unsupervised fashion by analyzing the local similarity of wavefront attributes.

Accordingly, the diffraction wavefront tomography we propose requires an additional input parameter: the event tag associated with each data point. The data space $\mathbf{d}$ is then given by

$$\mathbf{d}_i = (x_0, T, p, M_{NIP}, j)_i \,, \qquad i = 1, \ldots, n_{picks} \,, \qquad j = 1, \ldots, n_{events} \,, \tag{5.7}$$

where j denotes the event tag and n_{events} is the number of different diffractions identified in the data. As in the original implementation, the first step of the initial modeling consists of downward kinematic ray tracing into the initial velocity model, which yields first guesses of the subsurface locations $(x, z)_i$ related to each data point. These initial downward ray paths are illustrated in Figure 5.3a. While in the original implementation upward dynamic ray tracing starting from $(x, z)_i$ with the take-off angles θ_i provides the modeled data $\tilde{\mathbf{d}}$, in our modified implementation, the mean subsurface locations of all data points with the same event tag $(\bar{x}, \bar{z})_j$ are calculated and the upward dynamic ray tracing is started from these locations. In this case, the ray take-off angles are calculated from the measured slowness values p_i. The resulting initial upward ray paths for the simple diffraction example are illustrated in Figure 5.3b. Since they differ from the downward ray paths, this results in an initial misfit $\Delta\mathbf{d}$, which does not only depend on M_{NIP}, but mainly on x_0 and T. Consequently, the modified implementation allows setting the weighting factor w_M to zero, thereby evolving into a zero-offset slope tomography for diffractions.

5.4 Data examples

In this section, we present synthetic data examples comparing diffraction wavefront tomography to the conventional approach and analyzing the stability of the proposed method in the presence of lateral heterogeneity.

5.4.1 Simple diffraction data with vertical heterogeneity

The first example consists in an application of both conventional wavefront tomography and our modified implementation to synthetic diffraction data obtained in a vertically inhomogeneous velocity model with a velocity gradient of $0.5\,\mathrm{s}^{-1}$. The dataset contains a total of eight point diffractors. The input for the inversion, 879 automatically picked data points, is displayed in Figure 5.4a plotted onto the zero-offset semblance section provided by the CRS stack. Figure 5.4b shows the event tags that have been obtained in an unsupervised fashion based on the local similarity of the corresponding wavefront attributes (Bauer et al., 2019c). The inversion results are presented in Figure 5.5. In the upper row, the results of conventional wavefront tomography

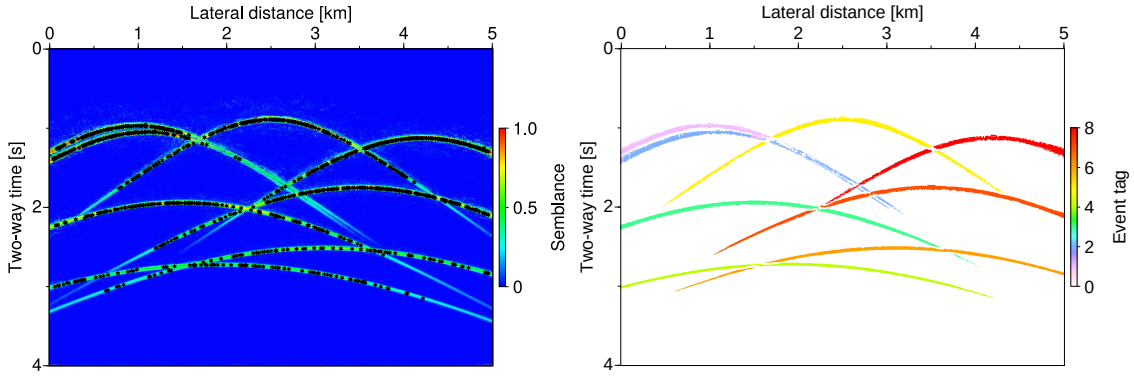

(a) Picked data points (b) Initial model

Figure 5.4: *Panel (a) shows the automatically picked data points plotted onto the zero-offset semblance, (b) the event tags obtained in an automatic fashion.*

are shown: starting from a constant initial model, displayed in Figure 5.5a, consisting in the near-surface velocity v_0 with the initial localizations (black asterisks) connected to all data points, the inversion algorithm converged to the final model displayed in Figure 5.5b with the final localizations. Figure 5.5c shows the constant initial model of diffraction wavefront tomography with the initial scatterer localizations $(\bar{x}, \bar{z})_j$ connected to each event tag (black dots). For all inversion runs, an initial grid of 6×5 B-spline knots with a spacing of 1000 m each was used. In a cascaded approach, the knot spacing was halved three times during the inversions, thus ending up with a 41×33-grid with a spacing of 125 m each. While Figure 5.5b is the result obtained with conventional wavefront tomography, Figures 5.5d and 5.5e are the models obtained with our modified implementation. In the latter, we set the weight for the curvatures w_M to zero, that is, no curvature information was used in the inversion. While this would imply a vanishing misfit and no convergence in the original implementation, in the modified implementation this approach provides a result of at least the same quality as the conventional implementation compared to the correct model (Figure 5.5f). Still, for this dataset without lateral heterogeneity it is possible to obtain good results with both implementations and both with or without relying on curvature information in diffraction wavefront tomography.

5.4.2 Simple diffraction data with lateral and vertical heterogeneity

The results for the second example, presented in Figure 5.6, are based on a zero-offset dataset, which contains both vertical and lateral heterogeneity and a total of nine point diffractors. Figure 5.6a shows the 7452 automatically picked data points plotted onto the coherence section obtained during the CRS attribute analysis. The event tags, which could be assigned successfully to each diffraction in an automated fashion (Bauer et al., 2019c), are displayed in Figure 5.6b, where each diffraction has a distinct color. As in the previous example, we applied both conventional wavefront tomography and diffraction wavefront tomography with and without using curvature information. For all inversion runs, we used an initial grid of 11×6 B-spline knots with a spacing of 1000 m each, which was halved three times during each inversion, thus ending up with a 81×41 grid with a spacing of 125 m each. The initial model of conventional wavefront tomography, for which again merely the near-surface velocity v_0 was assumed, is plotted in Figure 5.6c along

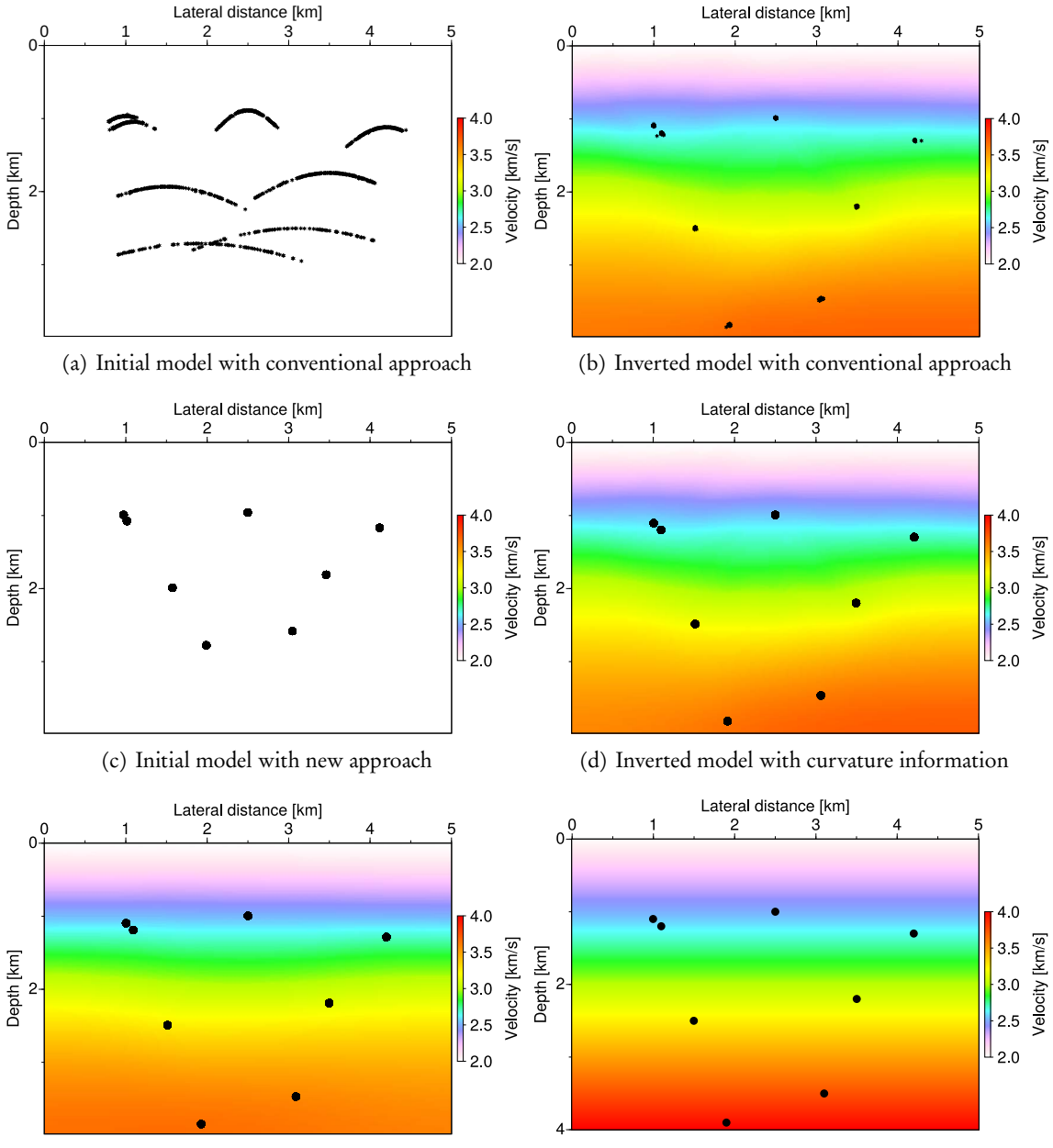

(a) Initial model with conventional approach

(b) Inverted model with conventional approach

(c) Initial model with new approach

(d) Inverted model with curvature information

(e) Inverted model without curvature information

(f) Correct model

Figure 5.5: *Results for synthetic data with vertical heterogeneity: (a) the initial model with the initial localizations (black asterisks) using conventional wavefront tomography, (b) the inverted model with the conventional approach without enforced diffraction focusing with the final localizations (black asterisks), (c) the initial model of the new approach with the initial localizations (black dots), (d) the inverted model of the new approach obtained using curvature information with the final localizations, (e) the inverted model obtained without using curvature information with the final localizations, (f) the correct model with the correct diffractor positions.*

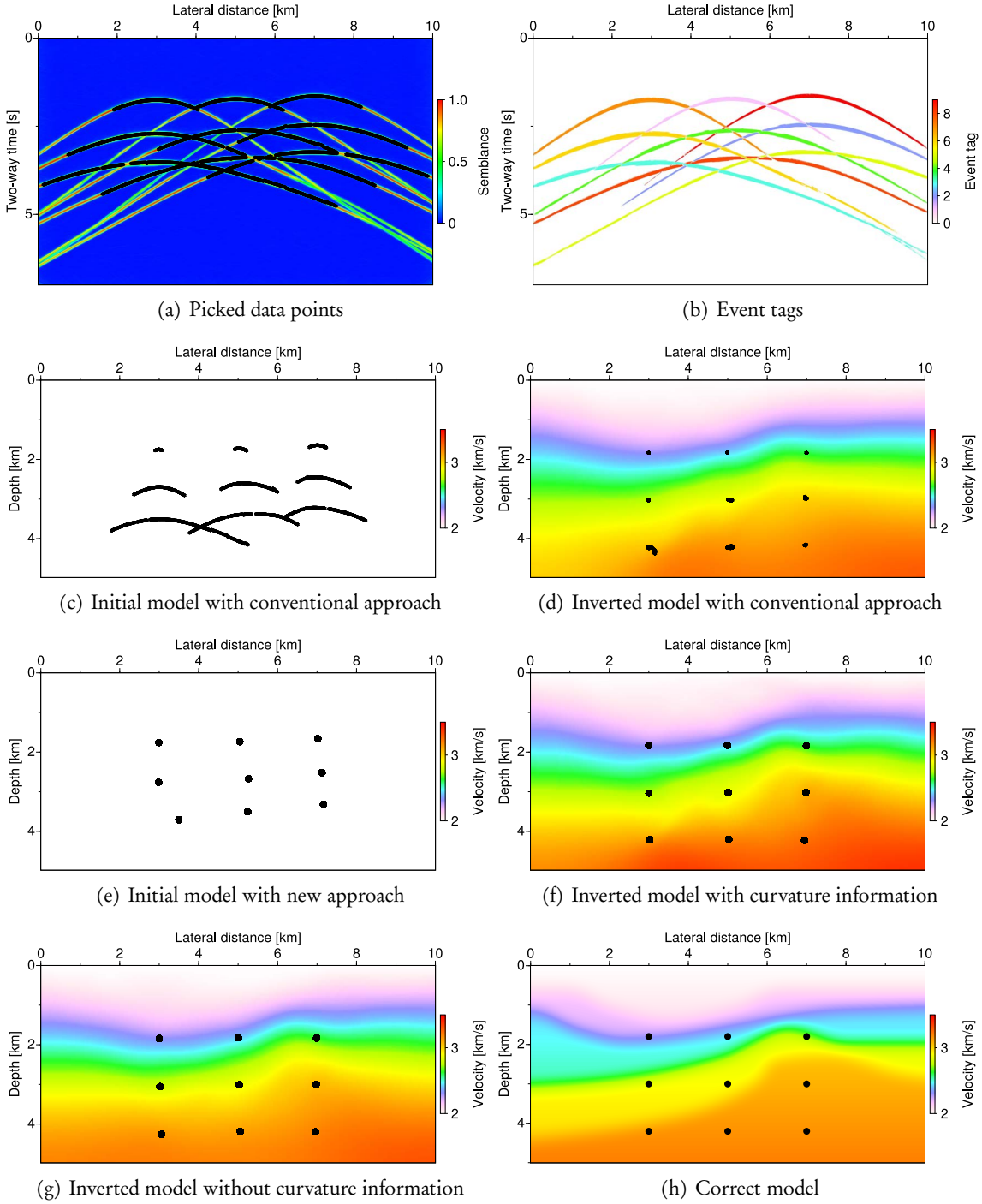

(a) Picked data points

(b) Event tags

(c) Initial model with conventional approach

(d) Inverted model with conventional approach

(e) Initial model with new approach

(f) Inverted model with curvature information

(g) Inverted model without curvature information

(h) Correct model

Figure 5.6: *Results for synthetic data with vertical and lateral heterogeneity: (a) the picked data points (black asterisks) plotted into the zero-offset semblance section, (b) the event tags, (c) the initial model with the initial localizations (black asterisks) of conventional wavefront tomography, (d) the conventional inverted model with the final localizations, (e) the initial model with the initial localizations (black dots) of the modified approach, (f) the inverted model obtained using curvature information with the final localizations, (g) the inverted model obtained without using curvature information with the final localizations, (h) the correct model with the correct diffractor positions.*

with the initial localizations of all data points. Figure 5.6d shows the inverted model using the conventional scheme, in which the overall velocity distribution (compare Figure 5.6h) could be retrieved fairly well and the – independently treated – data points focus in the correct nine distinct subsurface regions. In diffraction wavefront tomography, the data points connected to each event are not treated independently anymore, which leads to the initial localizations plotted in Figure 5.6e as black dots onto the constant initial model. Figures 5.6f and 5.6g are the velocity models and localizations obtained with the modified implementation that enforces diffraction focusing. While in the first, curvature information was used, the latter was obtained by setting the curvature weight w_M to zero, that is, the second-order attributes were not taken into account during the inversion. A comparison to the correct model with the correct diffractor positions (Figure 5.6h) reveals that the result obtained without using curvature information is the one closest to the correct model. This observation leads to the assumption that an inversion algorithm relying on curvatures may become less stable in settings with considerable lateral heterogeneity. However, the unique properties of diffractions allow to overcome this issue by enforcing their focusing in depth. This finding is supported by the fact that the conventional implementation of wavefront tomography, whose initial misfit exclusively depends on curvatures, for this example only converges, if the weight of the regularization term is increased.

5.5 Conclusions

We have presented a modified implementation of wavefront tomography (Duveneck, 2004b; Bauer et al., 2017b), which makes use of the unique physical properties of diffractions by forcing all measurements belonging to one diffraction to focus in the same subsurface location. A requirement for the application of the modified implementation is the a priori knowledge, which measurements in the data belong to the same diffraction. Once these event tags (Bauer et al., 2019c) are available, all data points with the same event tag are forced to focus in depth by calculating a mean subsurface location for each event and assigning it to the corresponding data points during the inversion. While the initial misfit of conventional wavefront tomography exclusively depends on second-order wavefront attributes, which can be difficult to determine in complex settings, the modified implementation relies primarily on zero-order and first-order attributes, whose estimation is generally more stable. As the new approach allows not to take into account second-order attributes it evolves into a zero-offset slope tomography for diffractions in this case. Results for synthetic diffraction data confirm the potential of our approach and suggest that it benefits from the improved stability in settings with lateral heterogeneity. Future work comprises further improvement of the event-tagging algorithm (Bauer et al., 2019c), the application to field data and the extension to 3D. Owing to their focusing nature, it can be demonstrated that the method is likewise applicable to passive-seismic events (Diekmann et al., 2019a).

Acknowledgments

This work was supported by the Federal Ministry for Economic Affairs and Energy of Germany (BMWi, 03SX427B) and by the sponsors of the Wave Inversion Technology (WIT) consortium, Hamburg, Germany. Benjamin Schwarz is supported by a research fellowship of the German Research Foundation (DFG, SCHW 1870/1-1).

6 Conclusions

While the understanding and processing of reflected-wave measurements is well-established in the field of applied seismics, the aim of this work has been to emphasize the unique physical properties of seismic diffractions, which are caused by small-scale subsurface heterogeneities and thus contain high-resolution information about the subsurface. A particular focus of this work lies on the illumination properties of non-Snell scattering, which I exploited during different processing steps. The final goal consisted in the development of a wavefront-tomographic scheme that enforces the focusing of measured diffracted wavefronts in depth and thus enables velocity-model building for low-fold-, zero-offset- and passive-seismic data.

In the first presented publication (Bauer et al., 2016a), we utilized the unique properties of diffractions for prestack diffraction enhancement. Since Snell's law does not hold for diffractions, the up- and downgoing ray paths are decoupled. While conventionally, the exact characterization of prestack data with wavefront attributes requires the application of finite-offset traveltime operators to the entire prestack data cube, with the proposed traveltime decomposition any set of finite-offset wavefront attributes can be composed out of two sets of zero-offset attributes. As a result, diffracted measurements within the whole prestack data cube can be characterized from zero-offset. We confirmed this finding by means of both simple and complex synthetic data examples, comparing the method to the well-established partial CRS, which extrapolates zero-offset operators into the prestack domain.

Instead of utilizing the decoupling of diffraction ray paths for prestack data enhancement, the same property lead to the assumption that diffractions bear the potential of closing the gap in terms of resolution that had been observed by Dümmong et al. (2008) between zero-offset-based methods for velocity model building such as wavefront tomography (Duveneck, 2004b) and finite-offset-based approaches such as prestack slope tomography (Billette and Lambaré, 1998). In the second presented publication (Bauer et al., 2017b), we utilized diffractions in wavefront tomography. By means of simple synthetic examples we demonstrated that only a few diffractions in the data are sufficient for resolving the subsurface velocity model. In an application to an industrial multi-channel field data set, we showed that a joint inversion of high-amplitude reflections and low-amplitude diffractions may help to increase the lateral resolution of the obtained velocity model. We backed this finding by performing a reverse-time depth migration using the velocity model obtained by reflection-only inversion and the one obtained by joint inversion of reflected and diffracted measurements. The results showed that the quality of the structural image of the subsurface improved when taking into account the diffracted wavefield. This observation was supported by flatter common-image gathers, which generally are an indicator for an improved velocity model.

However, in order to further benefit from the potential of diffractions, their focusing nature has to be exploited during the inversion: all measurements of one diffraction along the recording surface are known to originate from the same subsurface structure. Thus, in a correct velocity model, these measurements should focus in depth. Utilizing this fact, however, requires the a priori identification of those measurements that belong to the same diffraction. For this purpose,

I implemented an event-tagging algorithm, which is introduced in the third publication presented in this work (Bauer et al., 2019c). Based on the fact that wave propagation is a smooth process, the algorithm automatically analyzes the local similarity of zero-offset wavefront attributes and assigns a unique numerical tag to each diffraction found in the data. Results for synthetic diffraction data in both 2D and 3D as well as a field data application confirmed the functionality of the algorithm.

While also the diffraction decomposition (Bauer et al., 2016a) may benefit directly from the event tagging, more importantly it paves the way for diffraction wavefront tomography, which is introduced by the manuscript presented in the previous chapter (based on Bauer et al., 2019a). In this modified implementation of wavefront tomography (Duveneck, 2004b; Bauer et al., 2017b) the data points are not treated independently anymore, but all data points belonging to the same diffraction – as previously identified by their event tag – are forced to focus in depth. This focusing is enforced by calculating the mean event localizations for all equally tagged data points and initializing the upward ray tracing from these positions. This causes that the initial downward and upward ray paths do not coincide anymore and therefore – in contrast to conventional wavefront tomography – the initial misfit does not depend only on second-order wavefront attributes, but mainly on the lateral positions and the traveltimes. Applications to synthetic diffraction data with vertical and lateral heterogeneity suggest an improved stability of diffraction wavefront tomography in the case of lateral heterogeneity, where the estimation of second-order attributes is challenging. The modified implementation yielded particularly promising results, when second-order attributes were not taken into account at all, thereby evolving into a zero-offset slope tomography and thus closing the circle to the initial idea of this thesis.

7 Outlook

Although the results presented in this thesis may be seen as important first steps of utilizing the unique physical properties of diffractions in seismic processing, there is still a long way to go toward exploiting their full potential.

Inherently, diffractions are 3D phenomena, since diffracting structures scatter incoming waves into all directions. While 2D field data applications often suffer from out-of-plane effects, in three dimensions also the full illumination potential of diffractions can be exploited – not only in the case of a point diffraction, but also in the special cases of edge or line diffractions, which may be decomposed into their reflective and diffractive parts. Generally, all methods presented in this thesis either have been extended to 3D already or are extendable to 3D in a straightforward fashion.

7.1 Event tagging

An important part of future work comprises further development of the presented event-tagging scheme (Bauer et al., 2019c). While the method works well in synthetic diffraction examples with relatively few events, field data applications are challenging, particularly in regions, where diffractions lie close to each other. On the one hand, different matching strategies may be tested – for instance initializing the search at the diffraction apices instead of arbritrary locations –, on the other hand modern sophisticated image segmentation and pattern recognition techniques are expected to significantly improve the method. Further, the problem of event identification and tagging is perfectly suited for the application of deep learning algorithms. In connection with beamforming, the method may be extended to seismological problems similar to a method recently proposed by Ross et al. (2019), who try to associate measured phases to common earthquake sources. First successful results for event tagging in three dimensions have been presented by Werner (2018) and Bauer et al. (2019c), respectively. While the problem is better constrained in 3D due to the larger number of wavefront attributes – most importantly, there are two angles instead of one in 2D –, the implementation of the event tagging scheme in 3D still needs to be subject to further development in the future.

7.2 Wavefront tomography

The original implementations of wavefront tomography in both 2D and 3D have been established by Duveneck (2004b,a). In addition to the application of conventional 2D wavefront tomography to diffraction-only data, which is part of this thesis (Bauer et al., 2017b), results for academic and industrial single-channel data have been presented by (Schwarz et al., 2017a). The applicability of wavefront tomography to single-channel data is important in the context of academic acquisitions or legacy data, which often lack large offsets required for conventional tomographic schemes. In principle, an application to ground-penetrating radar (GPR) data, which is not always, but of-

ten zero-offset data, is also possible. A prerequisite for all of these cases is the separation of the diffracted wavefield that is often hidden behind high-amplitude reflections. For that purpose, Schwarz (2019) has introduced a method, which models and adaptively subtracts the dominant reflected wavefield from the data, thus revealing the weak diffracted background. Complex synthetic examples and a GPR field data application prove its potential. For multi-channel data, where both reflected and diffracted measurements are available, a combination of conventional wavefront tomography and diffraction wavefront tomography, which only forces diffractions to focus and treats data points connected to reflected measurements independently might lead to increased stability and better-resolved velocity models. Both the further development of methods to access and separate the diffracted wavefield and diffraction wavefront tomography remain a subject of active research.

In order to further increase the stability of wavefront tomography and to facilitate its application, first steps have been taken in the course of my work: I implemented an automatic refinement of the B-spline knot grid, which halves the knot spacing in both directions after each inversion run. Thus, the inversion may be initialized with a coarse grid and a constant initial model in order to resolve the low-frequency part of the velocity structure before successively refining the grid and the velocity model. While previously, the desired smoothness of the velocity model had to be steered by means of the regularization parameters (as done in Bauer et al., 2017b), these may be left constant when using the automatic knot refinement (as done in Bauer et al., 2019a), thus reducing the user interaction. A detailed investigation of the trade-off between regularization parameters and refinement of the knot grid might be worthwhile in the future. Further work might lead to an adaptive grid, which should be iteratively adjusted to the density of data points connected to the localizations in specific regions. Since such a variable grid might be impossible to combine with the matrix-based implementation of wavefront tomography, this might require a re-derivation and -implementation of wavefront tomography using the adjoint-state method, as done by Tavakoli F et al. (2017) for prestack slope tomography (Billette and Lambaré, 1998)

First applications of 3D wavefront tomography to diffraction-only data have been carried out by Werner (2018) and Glöckner et al. (2018) showed preliminary results of the application to 3D P-Cable data. Werner (2018) additionally tested an approach for the enforced focusing of diffractions in depth by including the standard deviations of all localizations with the same tag into the Fréchet matrix. While I also tested this jointly-developed idea in 2D, results suggested that the modified implementation presented in this thesis (Bauer et al., 2019a) is more promising. Consequently, the implementation and testing of diffraction wavefront tomography in 3D is part of future work.

Adjacent to the adaptation of wavefront tomography to the unique properties of diffractions, Znak et al. (2018) presented a novel implementation of wavefront tomography, which uses the so-called dynamic focusing to minimize the geometrical spreading of the back-propagated data points. In contrast to the matrix-based original implementation, they use an adjoint-state scheme for the minimization of the cost function. Whereas one aim of diffraction wavefront tomography was reducing the dependence on second-order attributes, this approach emphasizes the dependence on second-order attributes with the aim of reducing ambiguity. Future work includes an extension of this method in order to account for anisotropy.

A further possible direction of future work might be the systematic investigation and comparison of tomographic algorithms of different order. While traveltime tomography is most established in global studies, in more regional studies first-order slopes and second-order curvatures

are also taken into account. Since the results presented in this work suggest that for diffractions, slope tomography may yield velocity models of the same quality as second-order wavefront tomography, the question arises, if pure traveltime tomography might be able to provide similar results.

7.3 Passive-source seismology

Since diffractions are natural focusing functions, the connection from active-seismic diffractions to passive-source seismology can be directly established. The applicability of conventional wavefront tomography in passive seismic settings has been proven by Schwarz et al. (2016b) and Diekmann et al. (2019a). However, particularly in earthquake studies, the estimation of second-order attributes of body waves is highly challenging – because of, for instance, few available traces and noisy data – and therefore, mainly planar beamforming is used in these cases. Hence, the application of diffraction wavefront tomography might help to improve the results for both earthquake studies and passive seismic data. Since in the case of passive events the source excitation time is an additional unknown that has to be estimated, an optimization of the source excitation time, as suggested by Diekmann et al. (2019a), helps to stabilize the results.

7.4 Diffraction full-waveform inversion

In the recent years, inversion schemes, which invert for the measured waveforms instead of traveltime-related attributes, have become increasingly powerful and are used on both local (e.g. Virieux and Operto, 2009; Warner et al., 2013) and global scales (e.g. Fichtner et al., 2013; Sager et al., 2017). However, classical tomographic inversion schemes are still widely used in both academia and hydrocarbon industry, because computationally expensive waveform-based methods often require starting models that are sufficiently close to the true velocity distribution. In the context of diffractions, future work comprises the development of a diffraction full-waveform inversion (FWI). While conventional FWI in general can also invert for the diffracted wavefield, this requires relatively high frequencies, for which the inversion can become both unstable and expensive. In a diffraction FWI, however, the diffractors will be considered secondary sources and a one-way modeling will be used. Thus, it will not be necessary to run the FWI algorithm with particularly high frequencies. In this context, the joint velocity model building and scatterer localization provided by diffraction wavefront tomography, as presented in this thesis, will serve as an initial guess. Naturally, a diffraction FWI, in which active-seismic diffractions are treated as secondary sources, will be likewise applicable to passive-seismic and earthquake data.

Bibliography

Bakhtiari Rad, P., Schwarz, B., Gajewski, D., and Vanelle, C. (2018). Common-reflection-surface-based prestack diffraction separation and imaging. *Geophysics*, 83(1):S47–S55.

Bauer, A. (2014). From zero-offset to common-offset with diffractions. master's thesis, University of Hamburg.

Bauer, A., Schwarz, B., Diekmann, L., and Gajewski, D. (2019a). Wavefront tomography with enforced diffraction focusing. In *81st EAGE Conference and Exhibition 2019*.

Bauer, A., Schwarz, B., Diekmann, L., and Gajewski, D. (2019b). Wavefront tomography with enforced diffraction focusing. In *Second EAGE/PESGB Workshop on Velocities*.

Bauer, A., Schwarz, B., and Gajewski, D. (2015a). Prestack diffraction enhancement using a traveltime decomposition approach. In *SEG Technical Program Expanded Abstracts 2015*, pages 3820–3824. Society of Exploration Geophysicists.

Bauer, A., Schwarz, B., and Gajewski, D. (2015b). Zero-offset based prediction of common-offset diffraction traveltimes. In *77th EAGE Conference and Exhibition 2015 - Workshops*.

Bauer, A., Schwarz, B., and Gajewski, D. (2016a). Enhancement of prestack diffraction data and attributes using a traveltime decomposition approach. *Studia Geophysica et Geodaetica*, 60(3):471–486.

Bauer, A., Schwarz, B., and Gajewski, D. (2016b). Improving the resolution of wavefront tomography by utilizing diffractions. In *SEG Technical Program Expanded Abstracts 2016*, pages 5296–5301. Society of Exploration Geophysicists.

Bauer, A., Schwarz, B., and Gajewski, D. (2017a). Quantifying Diffracted and Passive Event Location Uncertainties with Local Wavefront Measurements. In *79th EAGE Conference and Exhibition 2017*.

Bauer, A., Schwarz, B., and Gajewski, D. (2017b). Utilizing diffractions in wavefront tomography. *Geophysics*, 82(2):R65–R73.

Bauer, A., Schwarz, B., and Gajewski, D. (2018a). Diffraction wavefront tomography – efficient automated velocity inversion for multi-fold and single-channel data. In *80th EAGE Conference and Exhibition 2018 - Workshops*.

Bauer, A., Schwarz, B., Lotze, M., Werner, T., and Gajewski, D. (2016c). Utilizing diffractions in wavefront-based tomography. In *78th EAGE Conference and Exhibition 2016*.

Bauer, A., Schwarz, B., Werner, T., and Gajewski, D. (2018b). An unsupervised strategy for the global tagging of individual diffractions. In *SEG Technical Program Expanded Abstracts 2018*, pages 4096–4100.

Bauer, A., Schwarz, B., Werner, T., and Gajewski, D. (2018c). Unsupervised global identification of diffractions based on local wavefront measurements. In *80th EAGE Conference and Exhibition 2018*.

Bauer, A., Schwarz, B., Werner, T., and Gajewski, D. (2019c). Unsupervised event identification and tagging for diffraction focusing. *Geophysical Journal International*, 217(3):2165–2176.

Baykulov, M., Dümmong, S., and Gajewski, D. (2011). From time to depth with CRS attributes. *Geophysics*, 76(4):S151–S155.

Baykulov, M. and Gajewski, D. (2009). Prestack seismic data enhancement with partial common-reflection-surface (CRS) stack. *Geophysics*, 74(3):V49–V58.

Baysal, E., Kosloff, D. D., and Sherwood, J. W. (1983). Reverse time migration. *Geophysics*, 48(11):1514–1524.

Bergler, S., Duveneck, E., Höcht, G., Zhang, Y., and Hubral, P. (2002). Common-reflection-surface stack for converted waves. *Studia geophysica et geodaetica*, 46:165–175.

Berkovitch, A., Belfer, I., Hassin, Y., and Landa, E. (2009). Diffraction imaging by multifocusing. *Geophysics*, 74(6):WCA75–WCA81.

Billette, F. and Lambaré, G. (1998). Velocity macro-model estimation from seismic reflection data by stereotomography. *Geophysical Journal International*, 135(2):671–690.

Bóna, A. (2011). Shot-gather time migration of planar reflectors without velocity model. *Geophysics*, 76(2):S93–S101.

Bortfeld, R. (1989). Geometrical ray theory: Rays and traveltimes in seismic systems (second-order approximations of the traveltimes). *Geophysics*, 54:342–349.

Claerbout, J. (1970). Coarse grid calculations of waves in inhomogeneous media with application to delineation of complicated seismic structure. *Geophysics*, 35(3):407–418.

Claerbout, J. F. (1985). *Imaging the earth's interior*, volume 1. Blackwell scientific publications Oxford.

Dafni, R. and Symes, W. W. (2017). Diffraction imaging by prestack reverse-time migration in the dip-angle domain. *Geophysical Prospecting*, 65(S1):295–316.

Dell, S. and Gajewski, D. (2011). Common-reflection-surface-based workflow for diffraction imaging. *Geophysics*, 76(5):S187–S195.

Diekmann, L., Schwarz, B., Bauer, A., and Gajewski, D. (2017). Approaching passive data with the established active seismic toolbox. In *79th EAGE Conference and Exhibition 2017 - Workshops*.

Diekmann, L., Schwarz, B., Bauer, A., and Gajewski, D. (2018a). Simultaneous model building and source localization: A 3D synthetic case study. In *SEG Technical Program Expanded Abstracts 2018*, pages 2937–2941.

Diekmann, L., Schwarz, B., Bauer, A., and Gajewski, D. (2018b). Source localisation and joint velocity model building. In *80th EAGE Conference and Exhibition 2018*.

Diekmann, L., Schwarz, B., Bauer, A., and Gajewski, D. (2019a). Source localisation and joint velocity model building using wavefront attributes. *Under review in Geophysical Journal International*.

Diekmann, L., Schwarz, B., Bauer, A., and Gajewski, D. (2019b). Wavefront tomography for passive seismic data. In *Second EAGE/PESGB Workshop on Velocities*.

Dümmong, S., Meier, K., Gajewski, D., and Hübscher, C. (2008). Comparison of prestack stereotomography and NIP wave tomography for velocity model building: Instances from the Messinian evaporites. *Geophysics*, 73(5):VE291–VE302.

Duveneck, E. (2004a). 3D tomographic velocity model estimation with kinematic wavefield attributes. *Geophysical Prospecting*, 52(6):535–545.

Duveneck, E. (2004b). Velocity model estimation with data-derived wavefront attributes. *Geophysics*, 69(1):265–274.

Eisenberg-Klein, G., Prüßmann, J., Gierse, G., and Trappe, H. (2008). Noise reduction in 2D and 3D seismic imaging by the CRS method. *The Leading Edge*, 27(2):258–265.

Farra, V. and Madariaga, R. (1987). Seismic waveform modeling in heterogeneous media by ray perturbation theory. *Journal of Geophysical Research: Solid Earth (1978–2012)*, 92(B3):2697–2712.

Fichtner, A., Trampert, J., Cupillard, P., Saygin, E., Taymaz, T., Capdeville, Y., and Villaseñor, A. (2013). Multiscale full waveform inversion. *Geophysical Journal International*, 194(1):534–556.

Fomel, S. (2002). Applications of plane-wave destruction filters. *Geophysics*, 67(6):1946–1960.

Fomel, S. and Kazinnik, R. (2013). Non-hyperbolic common reflection surface. *Geophysical Prospecting*, 61(1):21–27.

Fomel, S., Landa, E., and Taner, M. T. (2007). Poststack velocity analysis by separation and imaging of seismic diffractions. *Geophysics*, 72(6):U89–U94.

Foss, S.-K., Matias, J., Sollid, A., Loures, L., Pinotti, T., Brenne, E., Wergeland, Ø., Broch, T., Merten, D., and Ettrich, N. (2018). Examples of geology from seismic diffractions. In *SEG Technical Program Expanded Abstracts 2018*, pages 4141–4145. Society of Exploration Geophysicists.

Gelchinsky, B., Berkovitch, A., and Keydar, S. (1999). Multifocusing homeomorphic imaging: Part 1. Basic concepts and formulas. *Journal of Applied Geophysics*, 42(3):229–242.

Glöckner, M., Gajewski, D., Kläschen, D., Muff, S., and Berndt, C. (2018). Wavefront tomography with diffraction-only 3D P-cable data. In *SEG Technical Program Expanded Abstracts 2018*, pages 5133–5136. Society of Exploration Geophysicists.

Hubral, P. (1983). Computing true amplitude reflections in a laterally inhomogeneous earth. *Geophysics*, 48:1051–1062.

Hübscher, C. and Netzeband, G. (2007). Evolution of a young salt giant: The example of the Messinian evaporites in the Levantine Basin. In Wallner, M., Lux, K.-H., Minkley, W., and Hardy, J. H. R., editors, *The mechanical behaviour of salt*, pages 175–184. Taylor & Francis, London.

Jäger, R., Mann, J., Höcht, G., and Hubral, P. (2001). Common-reflection-surface stack: Image and attributes. *Geophysics*, 66:97–109.

Keller, J. B. (1962). Geometrical theory of diffraction. *Journal of the Optical Society of America*, 52(2):116–130.

Khaidukov, V., Landa, E., and Moser, T. J. (2004). Diffraction imaging by focusing-defocusing: An outlook on seismic superresolution. *Geophysics*, 69(6):1478–1490.

Klem-Musatov, K., Hron, F., and Lines, L. (1994). *Theory of seismic diffractions*. Society of Exploration Geophysicists.

Klokov, A. and Fomel, S. (2012). Separation and imaging of seismic diffractions using migrated dip-angle gathers. *Geophysics*, 77(6):S131–S143.

Kozlov, E., Barasky, N., Korolev, E., Antonenko, A., and Koshchuk, E. (2004). Imaging scattering objects masked by specular reflections. In *SEG Technical Program Expanded Abstracts 2004*, pages 1131–1134. Society of Exploration Geophysicists.

Krey, T. (1952). The significance of diffraction in the investigation of faults. *Geophysics*, 17(4):843–858.

Landa, E. and Keydar, S. (1998). Seismic monitoring of diffraction images for detection of local heterogeneities. *Geophysics*, 63(3):1093–1100.

Lavaud, B., Baina, R., and Landa, E. (2004). Automatic robust velocity estimation by post-stack stereotomography. In *SEG Technical Program Expanded Abstracts 2004*, pages 2351–2354. Society of Exploration Geophysicists.

Mann, J. (2002). *Extensions and applications of the common-reflection-surface stack method*. PhD thesis, University of Karlsruhe.

Mayne, W. H. (1962). Common reflection point horizontal data stacking techniques. *Geophysics*, 27(6):927–938.

Meier, K. (2007). Velocity model building: A comparison between prestack stereotomography and NIP-wave tomography. diploma thesis, University of Hamburg.

Moser, T. J. and Howard, C. B. (2008). Diffraction imaging in depth. *Geophysical Prospecting*, 56(5):627–641.

Müller, N.-A. (2009). Treatment of conflicting dips in the 3D common-reflection-surface stack. *Geophysical Prospecting*, 57(6):981–995.

Müller, T. (1999). *The common reflection surface stack method – seismic imaging without explicit knowledge of the velocity model*. PhD thesis, University of Karlsruhe.

Neidell, N. S. and Taner, M. T. (1971). Semblance and other coherency measures for multichannel data. *Geophysics*, 36(3):482–497.

Nelder, J. and Mead, R. (1965). A simplex method for function minimization. *American Mathematical Monthly*, 105:523–528.

Netzeband, G., Hübscher, C., and Gajewski, D. (2006). The structural evolution of the Messinian evaporites in the Levantine Basin. *Marine Geology*, 230(3):249–273.

Paige, C. C. and Saunders, M. A. (1982). LSQR: An algorithm for sparse linear equations and sparse least squares. *ACM Transactions on Mathematical Software (TOMS)*, 8(1):43–71.

Romanowicz, B. (2003). Global mantle tomography: progress status in the past 10 years. *Annual Review of Earth and Planetary Sciences*, 31(1):303–328.

Ross, Z. E., Yue, Y., Meier, M.-A., Hauksson, E., and Heaton, T. H. (2019). PhaseLink: A deep learning approach to seismic phase association. *Journal of Geophysical Research: Solid Earth*, 124(1):856–869.

Sager, K., Ermert, L., Boehm, C., and Fichtner, A. (2017). Towards full waveform ambient noise inversion. *Geophysical Journal International*, 212(1):566–590.

Santos, L. A., Mansur, W. J., and McMechan, G. A. (2012). Tomography of diffraction-based focusing operators. *Geophysics*, 77(5):R217–R225.

Schleicher, J., Tygel, M., and Hubral, P. (1993). Parabolic and hyperbolic paraxial two-point traveltimes in 3D media. *Geophysical Prospecting*, 41(4):495–513.

Schuster, G. T. (2002). Reverse-time migration = generalized diffraction stack migration. In *SEG Technical Program Expanded Abstracts 2002*, pages 1280–1283. Society of Exploration Geophysicists.

Schwarz, B. (2019). Coherent wavefield subtraction for diffraction separation. *Geophysics*, 84(3):1–47.

Schwarz, B., Bauer, A., and Gajewski, D. (2016a). Automatic joint location and velocity inversion for passive seismic data. In *78th EAGE Conference and Exhibition 2016*.

Schwarz, B., Bauer, A., and Gajewski, D. (2016b). Passive seismic source localization via common-reflection-surface attributes. *Studia Geophysica et Geodaetica*, 60(3):531–546.

Schwarz, B., Bauer, A., and Gajewski, D. (2017a). Automated single-channel data inversion using diffractions. In *79th EAGE Conference and Exhibition 2017*.

Schwarz, B., Bauer, A., and Gajewski, D. (2017b). A unified inversion scheme for diffractions and passive events. In *79th EAGE Conference and Exhibition 2017 - Workshops*.

Schwarz, B. and Gajewski, D. (2017a). Accessing the diffracted wavefield by coherent subtraction. *Geophysical Journal International*, 211(1):45–49.

Schwarz, B. and Gajewski, D. (2017b). A generalized view on normal moveout. *Geophysics*, 82(5):V335–V349.

Schwarz, B. and Gajewski, D. (2017c). The two faces of NMO. *The Leading Edge*, 36(6):512–517.

Schwarz, B., Vanelle, C., and Gajewski, D. (2014a). From zero-offset to common-offset with diffractions. In *76th EAGE Conference and Exhibition - Workshops*.

Schwarz, B., Vanelle, C., Gajewski, D., and Kashtan, B. (2014b). Curvatures and inhomogeneities: an improved common-reflection-surface approach. *Geophysics*, 79(5):S231–S240.

Schwarz, B., Vanelle, C., Wißmath, S., Bauer, A., and Gajewski, D. (2015). Efficient common-reflection-surface-based prestack slope determination for stereotomography. In *SEG Technical Program Expanded Abstracts 2015*, pages 5248–5253. Society of Exploration Geophysicists.

Soleimani, M., Piruz, I., Mann, J., and Hubral, P. (2009). Solving the Problem of Conflicting Dips in Common-Reflection-Surface (CRS) Stack. In *1st International Petroleum Conference & Exhibition*.

Spinner, M., Tomas, C., Marchetti, P., Gallo, C., and Arfeen, S. (2012). Common-offset CRS for advanced imaging in complex geological settings. In *SEG Technical Program Expanded Abstracts 2012*. Society of Exploration Geophysicists.

Taner, M. T. and Koehler, F. (1969). Velocity spectra – digital computer derivation and applications of velocity functions. *Geophysics*, 34:859–881.

Tarantola, A. (1984). Inversion of seismic reflection data in the acoustic approximation. *Geophysics*, 49(8):1259–1266.

Tarantola, A. (2005). *Inverse problem theory and methods for model parameter estimation*. SIAM.

Tavakoli F, B., Operto, S., Ribodetti, A., and Virieux, J. (2017). Slope tomography based on eikonal solvers and the adjoint-state method. *Geophysical Journal International*, 209(3):1629–1647.

Tromp, J., Tape, C., and Liu, Q. (2005). Seismic tomography, adjoint methods, time reversal and banana-doughnut kernels. *Geophysical Journal International*, 160(1):195–216.

Valenciano, A. A. and Biondi, B. (2002). Deconvolution imaging condition for reverse-time migration. *Stanford Exploration Project, Report*, 112:83–96.

Virieux, J. and Operto, S. (2009). An overview of full-waveform inversion in exploration geophysics. *Geophysics*, 74(6):WCC1–WCC26.

Walda, J. and Gajewski, D. (2015). Common-reflection-surface stack improvement by differential evolution and conflicting dip processing. In *SEG Technical Program Expanded Abstracts 2015*, pages 3842–3847. Society of Exploration Geophysicists.

Walda, J. and Gajewski, D. (2017). Determination of wavefront attributes by differential evolution in the presence of conflicting dips. *Geophysics*, 82(4):V229–V239.

Walda, J., Schwarz, B., and Gajewski, D. (2017). A competitive comparison of multiparameter stacking operators. *Geophysics*, 82(4):V275–V283.

Warner, M., Ratcliffe, A., Nangoo, T., Morgan, J., Umpleby, A., Shah, N., Vinje, V., Štekl, I., Guasch, L., Win, C., Conroy, G., and Bertrand, A. (2013). Anisotropic 3D full-waveform inversion. *Geophysics*, 78(2):R59–R80.

Werner, T. (2018). Application of 3D wavefront tomography to diffraction-only data. master's thesis, University of Hamburg.

Yilmaz, Ö. (2001). *Seismic data analysis*, volume 1. Society of Exploration Geophysicists, Tulsa.

Zhang, Y., Bergler, S., and Hubral, P. (2001). Common-reflection-surface (CRS) stack for common offset. *Geophysical Prospecting*, 49:709–718.

Znak, P., Kashtan, B., and Gajewski, D. (2018). Velocity model building by geometrical spreading focusing. In *SEG Technical Program Expanded Abstracts 2018*, pages 5188–5192. Society of Exploration Geophysicists.

List of peer-reviewed publications

Journal papers

- Bauer, A., Schwarz, B., and Gajewski, D. (2016a). Enhancement of prestack diffraction data and attributes using a traveltime decomposition approach. *Studia Geophysica et Geodaetica*, 60(3):471–486

- Schwarz, B., Bauer, A., and Gajewski, D. (2016b). Passive seismic source localization via common-reflection-surface attributes. *Studia Geophysica et Geodaetica*, 60(3):531–546

- Bauer, A., Schwarz, B., and Gajewski, D. (2017b). Utilizing diffractions in wavefront tomography. *Geophysics*, 82(2):R65–R73

- Bauer, A., Schwarz, B., Werner, T., and Gajewski, D. (2019c). Unsupervised event identification and tagging for diffraction focusing. *Geophysical Journal International*, 217(3):2165–2176

- Diekmann, L., Schwarz, B., Bauer, A., and Gajewski, D. (2019a). Source localisation and joint velocity model building using wavefront attributes. *Under review in Geophysical Journal International*

Expanded abstracts

- Bauer, A., Schwarz, B., and Gajewski, D. (2015b). Zero-offset based prediction of common-offset diffraction traveltimes. In *77th EAGE Conference and Exhibition 2015 - Workshops*

- Bauer, A., Schwarz, B., and Gajewski, D. (2015a). Prestack diffraction enhancement using a traveltime decomposition approach. In *SEG Technical Program Expanded Abstracts 2015*, pages 3820–3824. Society of Exploration Geophysicists

- Schwarz, B., Vanelle, C., Wißmath, S., Bauer, A., and Gajewski, D. (2015). Efficient common-reflection-surface-based prestack slope determination for stereotomography. In *SEG Technical Program Expanded Abstracts 2015*, pages 5248–5253. Society of Exploration Geophysicists

- Bauer, A., Schwarz, B., Lotze, M., Werner, T., and Gajewski, D. (2016c). Utilizing diffractions in wavefront-based tomography. In *78th EAGE Conference and Exhibition 2016*

- Schwarz, B., Bauer, A., and Gajewski, D. (2016a). Automatic joint location and velocity inversion for passive seismic data. In *78th EAGE Conference and Exhibition 2016*

- Bauer, A., Schwarz, B., and Gajewski, D. (2016b). Improving the resolution of wavefront tomography by utilizing diffractions. In *SEG Technical Program Expanded Abstracts 2016*, pages 5296–5301. Society of Exploration Geophysicists

- Bauer, A., Schwarz, B., and Gajewski, D. (2017a). Quantifying Diffracted and Passive Event Location Uncertainties with Local Wavefront Measurements. In *79th EAGE Conference and Exhibition 2017*

- Diekmann, L., Schwarz, B., Bauer, A., and Gajewski, D. (2017). Approaching passive data with the established active seismic toolbox. In *79th EAGE Conference and Exhibition 2017 - Workshops*

- Schwarz, B., Bauer, A., and Gajewski, D. (2017a). Automated single-channel data inversion using diffractions. In *79th EAGE Conference and Exhibition 2017*

- Schwarz, B., Bauer, A., and Gajewski, D. (2017b). A unified inversion scheme for diffractions and passive events. In *79th EAGE Conference and Exhibition 2017 - Workshops*

- Bauer, A., Schwarz, B., Werner, T., and Gajewski, D. (2018c). Unsupervised global identification of diffractions based on local wavefront measurements. In *80th EAGE Conference and Exhibition 2018*

- Bauer, A., Schwarz, B., and Gajewski, D. (2018a). Diffraction wavefront tomography – efficient automated velocity inversion for multi-fold and single-channel data. In *80th EAGE Conference and Exhibition 2018 - Workshops*

- Diekmann, L., Schwarz, B., Bauer, A., and Gajewski, D. (2018b). Source localisation and joint velocity model building. In *80th EAGE Conference and Exhibition 2018*

- Bauer, A., Schwarz, B., Werner, T., and Gajewski, D. (2018b). An unsupervised strategy for the global tagging of individual diffractions. In *SEG Technical Program Expanded Abstracts 2018*, pages 4096–4100

- Diekmann, L., Schwarz, B., Bauer, A., and Gajewski, D. (2018a). Simultaneous model building and source localization: A 3D synthetic case study. In *SEG Technical Program Expanded Abstracts 2018*, pages 2937–2941

- Bauer, A., Schwarz, B., Diekmann, L., and Gajewski, D. (2019b). Wavefront tomography with enforced diffraction focusing. In *Second EAGE/PESGB Workshop on Velocities*

- Diekmann, L., Schwarz, B., Bauer, A., and Gajewski, D. (2019b). Wavefront tomography for passive seismic data. In *Second EAGE/PESGB Workshop on Velocities*

- Bauer, A., Schwarz, B., Diekmann, L., and Gajewski, D. (2019a). Wavefront tomography with enforced diffraction focusing. In *81st EAGE Conference and Exhibition 2019*

Acknowledgments

First of all, I want to thank my wonderful wife Alejandra for her comprehension, her unconditional support and her infinite love. Eres mi alegría y mi felicidad – te amo con el alma!

Further, I would like to thank:

- Dirk Gajewski for the supervision of my PhD work and for his trust in my abilities. Thanks to you I had the chance to attend numerous conferences and to get to know a lot of people and places. I am very grateful for the chance of doing my PhD in your group and hope to continue being a part of it in the coming years.

- Benjamin Schwaaaaaahhhhrz, who has always been and still is my mentor in everything related to my work. Your vision, the so-called *golden flimmer*, and your ideas, which form the basis of this work, have motivated me a lot of times. I have enjoyed your company on various conferences, including our trip through the blooming landscapes of Eastern Texas and South Louisiäääääna with Philipp, and – sometimes hot-tempered or emotional ("JAAAAAAAAA!!!") – discussions on football (and a bit science, too). Apart from science, I highly appreciate not only your frienship, but also your talent in traditional Greek dance.

- Leon Diekmann, with whom I had the pleasure to work quite closely within the last two years. Your physical intuition and understanding has helped me at various stages of my work. In Paris, we enjoyed some after-conference happy-hours and I really enjoyed both our old-fashioned roadtrip to New Orleans and our roadtrip through California with Pavel, of which not only – but probably most importantly – the longest game in the history of the MLB World Series remains. At last, Laura and you have become very good friends to us. Oui oui, amigos muy buenos del Mojito grande!

- Ekkehart Tessmer whose efforts in producing the RTM results for my second paper I highly appreciate.

- Tobias Werner, who was the first student, whose bachelor's and master's theses I supervised. You implemented the event tagging in 3D and your first tests of the focusing constraints in 3D will be essential for the extension of diffraction wavefront tomography to 3D.

- Manuel Lotze, whose work during his bachelor's thesis also contributed to better understanding wavefront tomography.

- Pavel Znak for his pleasant and uncomplicated company on our roadtrip through California.

- Jan Walda for sharing an office with me for various years (and hopefully still some to come) and for his assistance in printing this thesis.

- Claudia Vanelle, to whom I will always be grateful for forwarding that contact in the Aliens Registration Office to me, which was absolutely vital for Alejandra and me.

- TEEC GmbH, in particular Gerald Eisenberg-Klein, Jürgen Prüssmann and Henning Trappe for the opportunity to visit the company and test my codes on their data and for their trust in my abilities in our joint projects.

- The the Federal Ministry for Economic Affairs and Energy of Germany for the funding of our project Difftomo (BMWi, 03SX427B), of which my PhD work is an essential part.

- The sponsors of the WIT consortium for the financial support of part of my PhD work.

- Matthias Hort, Felix Ament and Thomas Pohlmann, who agreed to be part of my examination board, as well as Céline Hadziioannou, who on short notice agreed to be part of my examination board for the defense.

Last, but not least, I am very grateful to my parents for their support of my studies. Finally, I want to thank all persons who directly or indirectly contributed to this work but are not part of this list.

Eidesstattliche Versicherung

Hiermit versichere ich an Eides statt, dass ich die vorliegende Dissertation mit dem Titel Utilizing the Unique Properties of Seismic Diffractions selbstständig verfasst und keine anderen als die angegebenen Hilfsmittel – insbesondere keine im Quellenverzeichnis nicht benannten Internetquellen – benutzt habe. Alle Stellen, die wörtlich oder sinngemäß aus Veröffentlichungen entnommen wurden, sind als solche kenntlich gemacht. Ich versichere weiterhin, dass ich die Dissertation oder Teile davon vorher weder im In- noch im Ausland in einem anderen Prüfungsverfahren eingereicht habe und die eingereichte schriftliche Fassung der auf dem elektronischen Speichermedium entspricht.

Hamburg, den 28. April 2019

Alexander Bauer